공학박사 학위논문

Enhancement of High Fidelity Hexagonal Geometry Core Analysis System for Diverse Applications

다양한 활용을 위한 고신뢰도 육방형 노심해석체계 개선

2023 년 2 월

서울대학교 대학원

에너지시스템공학부

김 성 찬

Enhancement of High Fidelity Hexagonal Geometry Core Analysis System for Diverse Applications

다양한 활용을 위한 고신뢰도 육방형
노심해석체계 개선

지도 교수 심 형 진

이 논문을 공학박사 학위논문으로 제출함
2023 년 1 월

서울대학교 대학원
에너지시스템공학부
김 성 찬

김성찬의 공학박사 학위논문을 인준함
2023 년 1 월

위 원 장 최 성 열 (인)

부위원장 심 형 진 (인)

위 원 주 한 규 (인)

위 원 조 진 영 (인)

위 원 이 현 철 (인)

Abstract

In this work, the hexagonal ray tracing module and coarse mesh finite difference (CMFD) acceleration, which are capable of explicitly modeling hexagonal geometry cores are developed in a direct whole core calculation code, nTRACER. The hexagonal ray tracing module employs the *elongated* model to explicitly model the unusual structures of a water-water energetic reactor (VVER) and sodium-cooled fast reactor (SFR) core. The assembly-wise modular rays are used in the hexagonal ray tracing calculation to reduce the tracking ray information to be stored. The coarse mesh finite difference (CMFD) formulation is expanded to the unstructured geometry to handle the irregular method of characteristics (MOC) cells in hexagonal assemblies. The CMFD calculation time and total computing time for the 2D VVER core problems are reduced by up to 39 % and 17 %, respectively, by using the super pin scheme.

The hexagonal ray tracing calculation in nTRACER is parallelized efficiently by employing the assembly-wise domain decomposition (ADD) scheme. Memory reduction and consequent reduction in computing time are possible by using the ADD scheme since the storage of the flat source region information is needed only for the assemblies being computed currently. The deterioration in the convergence of MOC calculations induced by using the ADD scheme is relaxed by updating the angular fluxes after CMFD calculations and by using the three-color scheme. The total computing time is reduced by up to 13 % and 23 % by using the three-color scheme and the angular flux storage scheme, respectively.

The hexagonal assembly-wise nodal solution is expanded to the unstructured geometry so that the high-fidelity analyses of SFR core deformations can be conducted in a practical time. The method to calculate the curvilinear and surface integrals of polynomials in arbitrary geometry is suggested. The triangle-based polynomial expansion nodal method and corner point balance calculation in a nodal code, RENUS are expanded to the unstructured geometry by using this method. The CMFD formulation in RENUS is expanded to the unstructured geometry similarly to nTRACER.

The solution accuracy of nTRACER is verified by comparing its calculation results against the McCARD results for the various hexagonal geometry core problems. The reactivity difference and the maximum and root-mean-square 3D pin power differences do not exceed 7 pcm, 6.41 %, and 0.44 %, respectively, for the

three 3D C5G7 H benchmark problems. The solution differences for the nine 2D KAERI VVER-1000 core problems do not exceed 106 pcm, 2.24 %, and 0.95 %, respectively, by using the P0 option. The two solutions for the 2D 'Full-core' VVER-440 and MET-1000 SFR core problems also match each other well. The solution differences are reduced by using the P2 option by up to 70 pcm in reactivity and 0.90 % in pin power distribution. It is demonstrated that nTRACER achieved satisfactory solution accuracy for hexagonal geometry core problems.

The ADD performance is examined by comparing the ray tracing time *with* and *without* the ADD scheme for the various VVER core problems. The ray tracing time and total computing time for the 2D full core problems are reduced by up to 48 % and 38 %, respectively. The two computing times for the 3D full core problems are reduced by up to 53 % and 45 %, respectively. It is verified that the hexagonal ray tracing calculation in nTRACER is parallelized efficiently by employing the ADD scheme.

The performance of the unstructured hexagonal nodal solution in RENUS is verified by comparing its calculation results against the McCARD results for the 2D schneller natriumgekühlter reaktor-300 core problems. Arbitrary core deformations, *contrived states* were applied to the core problems to expose the RENUS solution accuracy for unstructured geometry. The solution differences for the changes in reactivities and assembly power distribution induced by *contrived states* on the fuel region do not exceed 7 pcm and 0.46 %, respectively. In contrast, the reference reactivity and assembly power change by up to 240 pcm and 47.76 %, respectively. The RENUS solutions were further verified by decomposing the deformed core problem with uniform expansion into the deformed core problems with assembly-wise expansion. The verification results reveal that excellent agreements between the two solutions for deformed core problems do not owe to any error cancellation. Thus, it is concluded that RENUS attained significantly high accuracy in predicting the changes in nuclear characteristics induced by core deformations by using the unstructured nodal method.

Keyword : hexagonal geometry core, ray tracing calculation, coarse mesh finite difference formulation, assembly-wise domain decomposition, thermal core expansion, unstructured nodal solution
Student Number : 2016-21288

Table of Contents

List of Figures

List of Tables

Chapter 1. Introduction

In this work, the hexagonal ray tracing module and coarse mesh finite difference (CMFD) acceleration, which are capable of explicitly modeling hexagonal geometry cores including complicated structures, are developed in a direct whole core calculation (DWCC) code, nTRACER. The hexagonal assembly-wise nodal solution is expanded to the unstructured geometry so that the high-fidelity analyses of sodium-cooled fast reactor (SFR) core deformations can be conducted in a practical time.

Two-step core calculation (TSCC) code systems are to employ lower-order solution methods to analyze the core of a nuclear reactor using the group constants generated from the higher order solution for each typical assembly. The nuclear characteristics of reactor cores have been generally simulated by a TSCC code due to its advantage of low computing cost. With astonishing progress in computational processing units and storage devices in recent times, however, the need for the whole core solution with high resolution and transport-based accuracy has got increased justification. DWCC methods, which are to enhance solution fidelity by eliminating the advance procedure of generating homogenized assembly or pin cross-sections, have been extensively used in numerous codes [1]–[3] dealing with Cartesian geometry cores.

Water-water energetic reactors (VVERs), which are pressurized water reactors with hexagonal fuel assemblies, have spread in the East-European bloc and developing countries for several decades. Neutron moderation in the VVER core is complicated by unusual structures such as Vygorodka, the corner stiffener, and the water channels at the core basket. The complication undermines the assumptions of the diffusion equation and assembly or pin homogenization. Thus, it is expected that the DWCC method performing the sub-pin level transport calculation would outperform the assembly-wise or pin-wise nodal methods for VVER cores.

Currently, several codes have the hexagonal geometry handling feature in DWCC calculation. DeCART and STREAM are incorporated in TSCC code systems solving VVER core problems.[5]–[6] DeCART achieved the abundant analyses of high-temperature gas-cooled cores [7], and STREAM conducted verifications for 2D SFR core problems.[8] MPACT and NECP-X are also equipped with hexagonal ray tracing modules in recent years.[9]–[10] nTRACER has been coupled with T/H codes in the multi-physics analyses of VVER cores.[11]–[12]

Efficient application of parallel computation is necessary for the DWCC code, which performs large-scale calculations on millions of flat source regions (FSRs). The angle-wise parallelization, where threads trace the bunches of tracking rays in parallel across the whole problem domain, can be easily implemented while it has drawbacks in that the number of parallel processors is limited and a huge amount of memory is required. The assembly-wise domain decomposition (ADD) scheme was introduced in the DWCC codes for Cartesian geometry [13]–[14] to effectively exploit massively parallel computing platforms involving thousands of processors. In the plane-wise parallelization which is to assign a group of planes to different computing nodes, the ADD scheme using the OpenMP constructs can effectively reduce computing time by alleviating fetching overhead due to memory access bottleneck.

SFRs are estimated to have the highest feasibility of commercial operations among Generation-VI reactors due to their high efficiency in nuclear fuel usage.[15] SFRs also include hexagonal fuel assemblies. The complication is further increased by employing the double assembly duct and non-fuel assemblies with different rod sizes. The critical characteristic of SFR cores is the thermal core expansion induced by high power density and steep temperature gradient, which significantly impact reactivity and power distribution. The DWCC method using millions of FSRs is not adequate to deal with moving geometries. A low-scale computing resource is exploited in a nodal method employing fuel assembly size coarse meshes while its governing equations have been established only for regularly structured geometries so far.

Many codes, e.g., BOWPERT [16], RHOBOW [17], and BISTRO [18] have been carried out the analyses of SFR core deformations based on the perturbation theory. Those codes, which are to predict reactivity change induced by sufficiently small deviation from the reference state, have a weakness in analyzing a large-scale core deformation and consequent power distribution change. GeN-Foam [19] and PROTEUS-SN [20] explicitly model SFR core deformations by employing the finite difference method (FDM) and finite element method (FEM), respectively, on unstructured meshes. Those methods require a huge computing cost as mesh size is decreased to reduce discretization error.

The flux expression of a nodal solution is uniquely determined by reducing the number of unknown variables in physical constraints as the number of flux

expansion coefficients. The unknown variable can be specified by being substituted with the input determined from previous calculations or an equation of other unknown variables. Thus, the nodal method can be expanded to the unstructured geometry by deriving the variable expressions incorporating the curvilinear and surface integrals of functions used to approximate the flux distribution in an unstructured mesh.

1.1. Purpose and Scope of the Research

The unusual structures of VVER and SFR cores undermine the assumptions of the diffusion equation and assembly or pin homogenization adopted in the conventional TSCC code system. One of the purposes of this research is to develop the hexagonal ray tracing module and CMFD acceleration in nTRACER, which is capable of explicitly modeling hexagonal geometry cores. There needs to be more than the prediction of reactivity change based on the perturbation theory to grasp the entire characteristics of SFR thermal core expansions. A DWCC method, FDM, FEM, and Monte Carlo method require a large-scale computing resource to model core deformations. The other purpose of this research is to expand the hexagonal assembly-wise nodal solution to the unstructured geometry so that the high-fidelity analyses of SFR core deformations can be conducted in a practical time.

The hexagonal ray tracing module is developed in nTRACER by using the *elongated model* and assembly-wise modular ray scheme to model hexagonal geometry cores explicitly. The hexagonal ray tracing calculation using cells of different shapes is accelerated by the CMFD formulation expanded to the unstructured geometry. The computing time of nTRACER calculations for hexagonal geometry core problems is reduced by employing the super pin scheme in the CMFD formulation.

The hexagonal ray tracing calculation in nTRACER is parallelized efficiently by employing the ADD scheme. A significant drawback in the ADD scheme is that the lag in updating the incoming angular fluxes at the assembly surface would deteriorate the convergence of the method of characteristics calculation. The incoming partial current at the assembly surface is updated by using the incoming partial current change determined by the CMFD calculation. The three-color scheme and angular flux storage scheme (AFSS) are employed to enhance the ADD performance.

The method to calculate the curvilinear and surface integrals of polynomials in arbitrary geometry by using the look-up table is suggested. A nodal code, RENUS [21] solves 3D hexagonal geometry core problems by employing the triangle-based polynomial expansion nodal (T-PEN) method [22], corner point balance (CPB) solution, nodal expansion method (NEM), and approximation to the axial leakage source distribution. The polynomial expressions of the areal fluxes and flux moments, surface fluxes, and currents are established in arbitrary geometry. RENUS is capable of solving 2D deformed hexagonal geometry core problems by incorporating those expressions in the governing equations in the T-PEN method and CPB solution.

In this work, the application scope is limited to the steady-states of hexagonal geometry cores rather than transients or depletions. The nTRACER solution accuracy is verified by comparing its solutions against the reference solutions for the 3D hexagonal variation benchmark problems and 2D VVER and SFR core problems. The ADD performance is examined by comparing the ray tracing time *with* or *without* the ADD scheme for the 2D and 3D VVER core problems. The accurate analysis of SFR core deformations requires considering millions of interactions between core components in neutronics, thermal-hydraulics, thermal-mechanics, and radiologics, which exceeds the scope of this thesis. Thus, this work focuses on the hypothetical deformation states of the 2D SFR benchmark problems in verifying the unstructured nodal solution in RENUS.

1.2. Outline of the Thesis

Chapter 2 presents the comprehensive descriptions of code development of nTRACER for a hexagonal geometry core. The complicated geometries of VVER and SFR cores are illustrated. The cell and modular ray schemes are selected to model hexagonal geometry cores explicitly. The CMFD formulation in unstructured geometry and the super pin scheme used in the CMFD update are described.

Parallelization of hexagonal ray tracing calculations with the ADD scheme is described in Chapter 3. The principle of the ADD scheme which renders a reduction in computing time is presented. The equation to update the assembly incoming angular flux in the ADD scheme is derived. Performance examinations for the three-color scheme and AFSS are carried out by comparing the computing time between different schemes.

Chapter 4 presents the detailed descriptions of the RENUS nodal solutions for

unstructured geometry. The method to calculate the curvilinear and surface integrals of polynomials in arbitrary geometry is described. The governing equations for regular hexagonal geometry are introduced first, and subsequently, the expansion of these equations to the unstructured hexagonal geometry is described.

Chapter 5 deals with verifications of the nTRACER solutions for the various hexagonal geometry core problems and performance examinations of the hexagonal ray tracing calculations with the ADD scheme. The RENUS unstructured nodal solutions for the 2D irregularly deformed hexagonal geometry core problems are compared against the reference solutions produced by McCARD. Chapter 6 concludes the thesis.

Chapter 2. Development of the Hexagonal Ray Tracing Module and CMFD acceleration in nTRACER

One of the purposes of this research is to develop the hexagonal ray tracing module and coarse mesh finite difference (CMFD) acceleration in nTRACER, which is capable of explicitly modeling hexagonal geometry cores. Thus, the core configurations of Water-water energetic reactor (VVER) cores and sodium-cooled fast reactor (SFR) cores including the unusual structures to be modeled by nTRACER are presented first. In the subsequent subsection, the cell and modular ray schemes employed in the hexagonal ray tracing calculation in nTRACER are carefully selected by considering hexagonal geometries. The last subsection describes the expansion of CMFD formulation to the unstructured geometry required to solve method of characteristics (MOC) cells in hexagonal assemblies. Improvement in the performance of CMFD calculations by using the super pin scheme is verified for the 2D VVER core problems.

2.1. Descriptions of the Hexagonal Geometry Core Problems

Before developing the necessary geometry extension of nTRACER for the accurate modeling of VVERs, various hexagonal benchmark specifications need to be checked thoroughly. In this regard, the four benchmark problems to be solved by nTRACER are described with the approximations introduced in the nTRACER modeling.

The VVER-1000 reactor benchmark problems were proposed by korea atomic energy research institute (KAERI) to verify the code capability in the US/ROK I-NERI program.[23] This benchmark is referred to as 'KAERI benchmark' in the following. The benchmark set consists of 5 parts: a pin cell, an assembly *with* and *without* control rod insertion, a 2D whole core, and a 3D whole core. The fuel loading pattern shown in Figure 2.1 is originated from the first cycle of Kozloduy Unit 6 with the fuel assembly TVS and TVSM. The assembly and pin pitches are 23.6 cm and 1.275 cm, respectively. Each part is divided into sub-problems with different fuel enrichments, fuel and moderator temperatures, and boron concentrations.

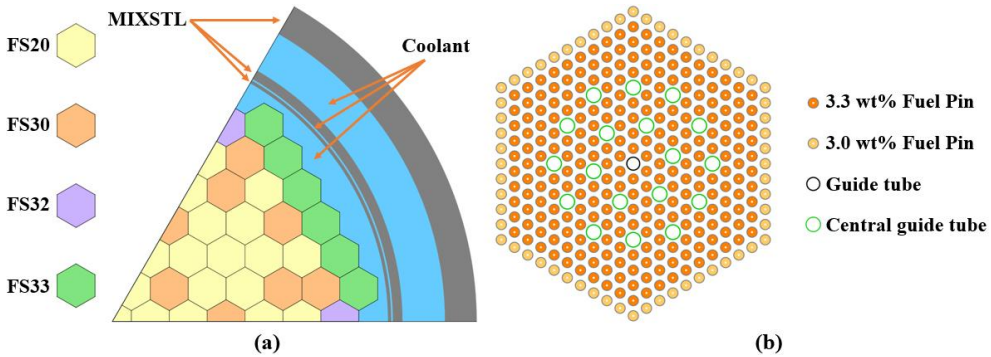

Figure 2.1. (a) Radial core configuration and (b) pin layout of FS 32 in the KAERI benchmark problem.

The axial configuration of the core is depicted in Figure 2.2.a. Since the 3cm thin plane of spacer grids would cause instability in the nTRACER calculation, the spacer grid is approximated as a single cylindrical tube within the active fuel region as shown in Figure 2.2.c. While the spacer grid volume is conserved, the outer radius is reduced from 0.5769 cm to 0.5535 cm.

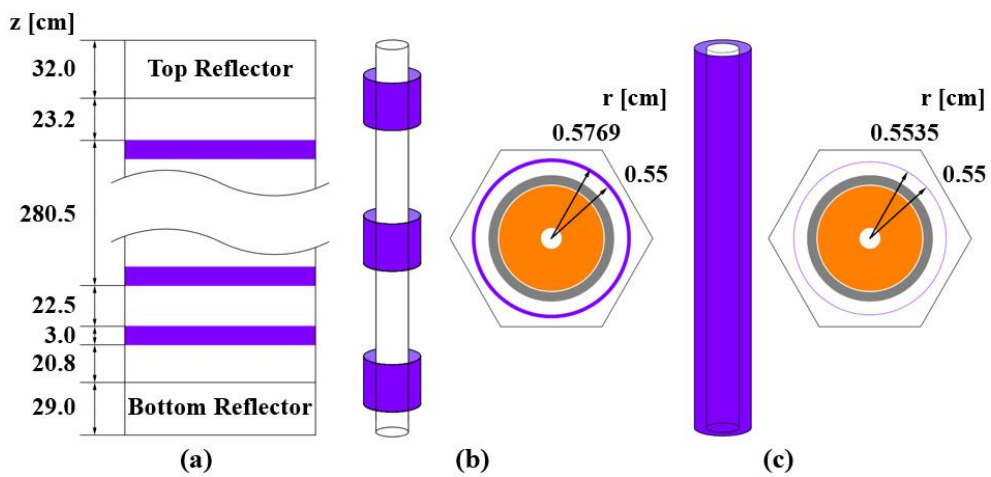

Figure 2.2. (a) Axial core configuration and (b) spacer grid in the KAERI benchmark problem (c) nTRACER modeling.

Based on the operational data of the second VVER-1000 Unit of the Ukrainian nuclear power plant Khmelnitsky, the X2 VVER-1000 benchmark problem was proposed for further validation and verification of VVER-1000 reactors with the TVSA fuel assembly.[24] Tasks for steady-state, transient, and burn-up calculations are provided in this benchmark problem. The experimental values and reference Monte Carlo solutions for reactivity and power distribution are also provided. The

radial core configuration and the pin layout of the fuel assembly types are depicted in Figure 2.3. Compared to the KAERI benchmark problem, the fuel assembly types are more complicated with the burnable Gd_2O_3 absorber. The core basket with the groove region and the water channels are added to the X2 benchmark problem. The inner three fuel pins with the burnable absorber in 39AWU change their position when reflected or rotated in the azimuthal direction. Due to this asymmetry, the solution for the one-sixth core problem with any azimuthal boundary condition cannot be identical to that for the full core problem.

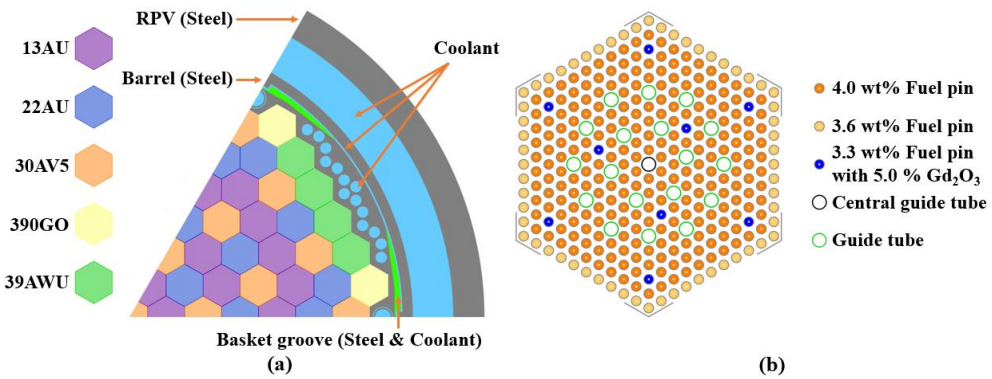

Figure 2.3. (a) Radial core configuration and (b) pin layout of FA 39 AWU in the X2 benchmark problem.

The X2 benchmark problem is explicitly modeled in nTRACER following the revised benchmark specifications [25] except for several approximations. The double rings in the coolant channel are approximated as a single ring with a radius of 5.59 cm while the coolant volume is conserved. The dent in the groove region is neglected. Since the central guide tube exceeds the hexagonal MOC cell in nTRACER, its radius is reduced from 0.65 cm to 0.633 cm. The temperature of all elements, coolant density, and boron concentration in the coolant are set to 281.0 °C, 0.7626 g/cc, and 1077 ppm, respectively.

The VVER-440 'Full-core' benchmark problem is a 2D calculation benchmark problem based on a VVER-440 reactor core set at the cold state with explicit modeling of the radial reflector.[26] This benchmark problem is referred to as VVER440FC in the following. The radial core configuration and the pin layout of the fuel assembly are depicted in Figure 2.4. The assembly and pin pitches are 14.7 cm and 1.23 cm, respectively. The fuel assembly is enclosed with the assembly duct, and the outer-most fuel assemblies are wrapped with 'Vygorodka', a kind of shroud, in the VVER-440 core. The temperature of all elements, coolant density, and content

of the absorbing material (H_3BO_3) in the coolant are set to 543.15 K, 0.7775 g/cc, and 3.0 g/kg, respectively.

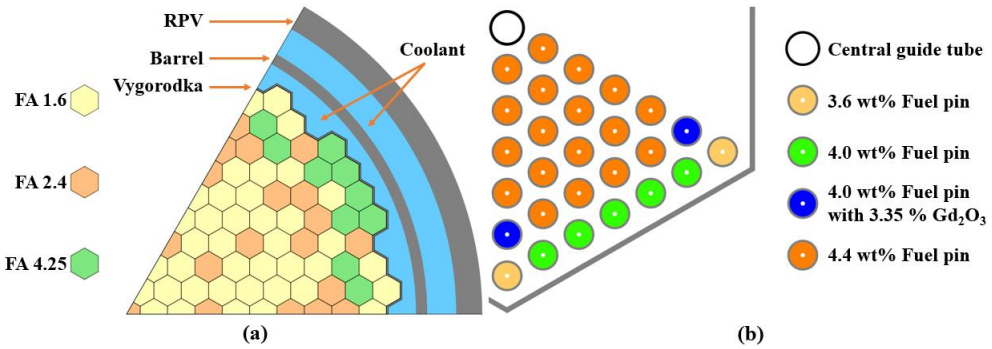

Figure 2.4. (a) Radial core configuration and (b) pin lay out of FA 4.25 in the VVER440FC benchmark problem.

The VVER440FC benchmark problem is limited to the planar core while the simple axial configuration shown in Figure 2.5 is represented in the 180° benchmark problem.[27] In the examination for VVER-440 3D cores, the planar core of the VVER440FC benchmark is extended axially with an active height of 250 cm. The two axial reflectors are filled with the material identical to that of the radial moderator.

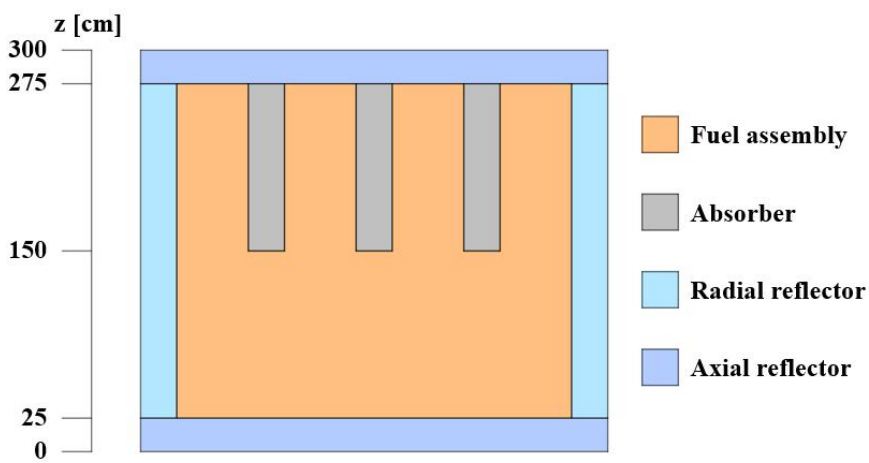

Figure 2.5. Axial core configuration in the 180° benchmark problem.

The advanced burner reactor (ABR) core was designed for the study of future fast reactor designs.[28] The MET-1000 benchmark includes the 1000 MWth medium-size core incorporating a ternary metallic fuel and mixed-oxide fuel. The

fuel loading pattern of an assembly pitch of 16.2471 cm is depicted in Figure 2.6. The distinctive geometries of this benchmark problem are the different pin radii ranging from 0.3857 cm to 2.3606 cm and the double-layered duct at the control assemblies as shown in Figure 2.7. The fuel and non-fuel are at uniform temperatures of 432.5 ℃ and 534 ℃, respectively. The complicated axial configuration of the core of a height of 480.2 cm is described in this benchmark problem. Nonetheless, only the 2D core problem established from the middle plane of the core is solved in this work due to a calculation instability in nTRACER induced by the severe axial gradient of flux and temperature in the core.

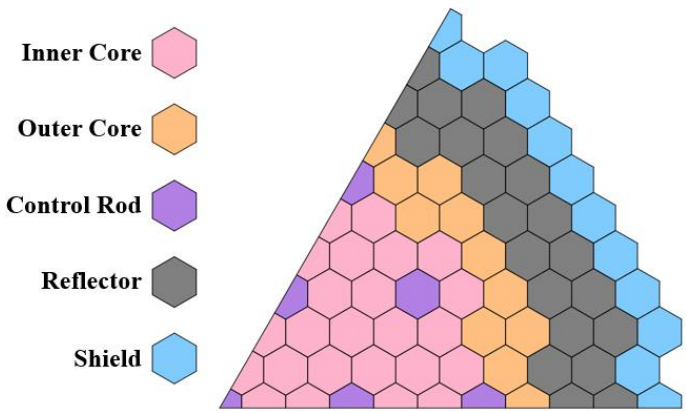

Figure 2.6. Radial core configuration in the MET-1000 benchmark problem.

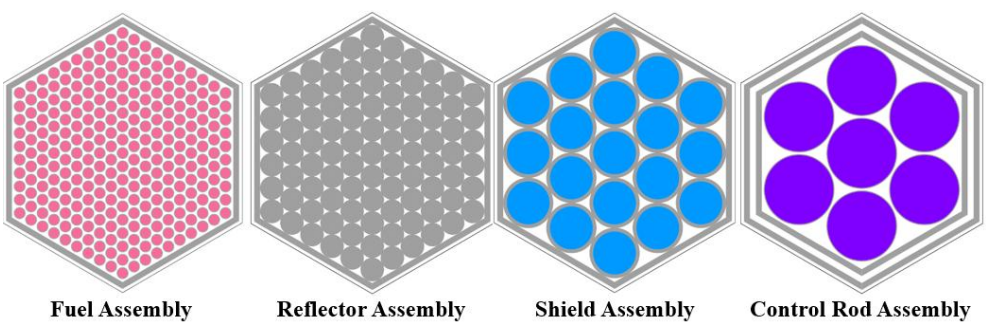

Figure 2.7. Radial assembly configurations in the MET-1000 benchmark problem.

2.2. Ray Tracing Calculation Using the Modular Ray in a Hexagonal Assembly

The features of handling hexagonal geometry in nTRACER had to be extended to model the VVER cores explicitly. This section briefly describes the basic general calculation scheme of nTRACER, and the specific extensions for VVER geometries

are then followed.

nTRACER solves 3D core problems by iterating the calculations with different resolutions and geometries. The sub-pin level planar MOC solution is used to determine the homogenized group constants in pin level to be used in the 3D CMFD formulation. During the outer iterations in the CMFD calculation, the axial MOC calculation is invoked. Given the flux, flux form function, and radial transverse leakage, the axial MOC calculation is performed to update the axial current between the axial nodes of each pin. The solvers of planar MOC and 3D CMFD for hexagonal geometries were newly developed to solve hexagonal geometry core problems while the axial MOC solver was modified with minor changes for summing the transverse leakage in hexagonal geometry.

The planar MOC cell can be easily constructed in rectangular geometry since both fuel rods and moderator gaps can be modeled similarly to a rectangular cell. However, the moderator gap in hexagonal geometry cannot be easily modeled as a hexagonal cell like a fuel rod. There can be two available models to fill up the hexagonal assembly with cells as shown in Figure 2.8. In the *chopped model*, all the fuel rods in a hexagonal assembly are modeled as a hexagonal cell, and the zigzag-shaped residual region is chopped at the hexagonal cell vertex. On the contrary, the fuel rods along the assembly periphery are modeled as an outward-elongated pentagon cell in the *elongated model*. As a consequence, the moderator gap is modeled as a trapezoidal cell. The rectangular gap cell is divided in half in case of solving one-sixth core problems. While DeCART, the direct whole core calculation (DWCC) code of KAERI, adopts the *chopped model*,[1] nTRACER adopts the *elongated model*. In the latter model, a computing resource for tracking cells in MOC and CMFD solutions can be increased with more cell types, and the accuracy of the planar MOC solution might be deteriorated by uneven fuel cell area. However, hexagonal-annulus structures along the assembly periphery such as Vygorodka of VVER-440,[26] the assembly duct of SFR,[28] and the corner stiffener of VVER-1000 [24] can be modeled explicitly by using the latter model whereas the former model cannot.

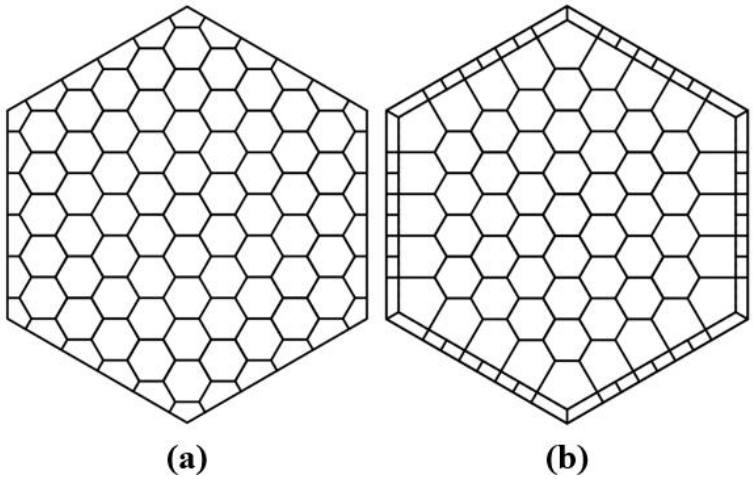

Figure 2.8. (a) *Chopped model* and (b) *Elongated model* for the hexagonal assembly.

In the ray tracing calculation, the outgoing angular flux at each source region is updated based on the solution of the Boltzmann transport equation following a ray across the problem plane. Rays are constructed in a hierarchical structure prior to the ray tracing calculation. A cyclic ray or rotational ray starts and ends at the core outer boundary, respectively. It is reflected on the core azimuthal boundary if exists. The cyclic ray can be decomposed into assembly rays, which start and end at the assembly surface, respectively. Ray tracing parameters such as the ray spacing, the number of azimuthal angles, and the number of polar angles are specified in the user input. The ray spacing, azimuthal angle, and weight of cyclic ray are adjusted so that all assembly rays on the problem plane belong to a set of basis rays, so-called modular rays in a unit assembly to save computing resource. The modular ray passes through the flat source regions (FSRs), of which the region index and segment length are stored for the ray tracing calculation. In DeCART, the modular ray is approximated by linking cell rays to reduce the segment information to be stored. However, the memory for modular rays is insignificant compared to others, e.g., the memory needed for the scalar flux storage at FSRs. Therefore, the modular rays are modeled explicitly in nTRACER to prevent losing solution accuracy.

At each imaginary assembly filled with MOC cells of a single type, the segments of modular rays are stored in the unit of a cell as shown in Figure 2.9.a. Sub-divisions among FSRs along the radial direction and azimuthal direction in MOC cells are omitted here, and the ray spacing is exaggerated for brevity. During the ray tracing calculation, the cyclic ray is swept in the unit of a cell by looking up the segment information from the corresponding cell ray in the modular ray as shown

in Figure 2.9.b.

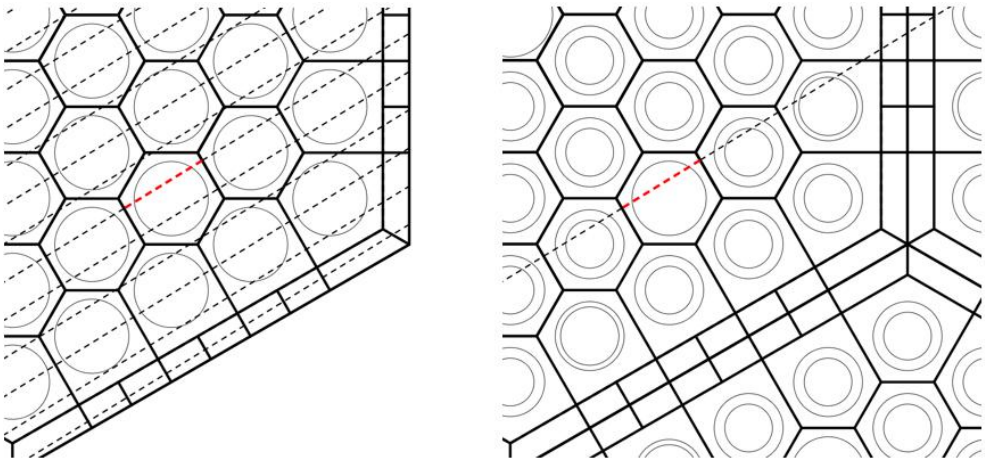

Figure 2.9. (a) Modular ray at the imaginary assembly (b) cyclic ray on the problem plane.

Vygorodka is a steel reflector which wraps the outer-most fuel assembly in the VVER-440 core as shown in Figure 2.10.a. The *elongated model* cannot model the protruded corner of Vygorodka explicitly. Thus, the moderator and steel materials are homogenized into a mixture as an area-weighted average at the gap cell colored red in Figure 2.10.b. Note that the dimensions of the fuel cells and moderator cells are different in this figure. The hexagonal version of nTRACER is capable of modeling the problem with cells of different dimensions, which is a significant characteristic of an SFR.

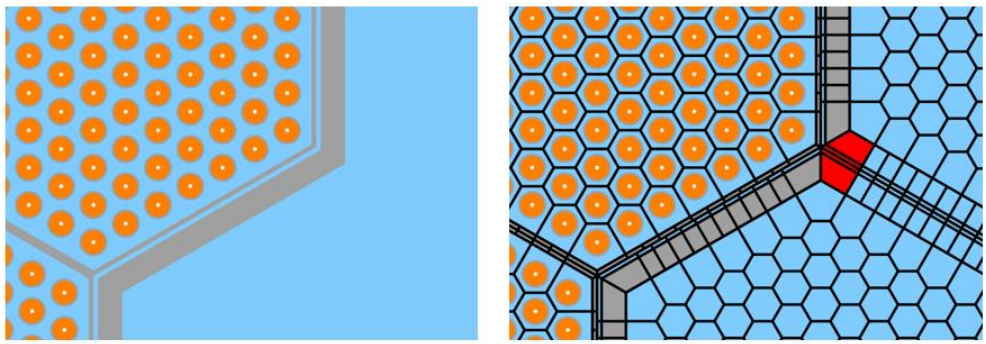

Figure 2.10. (a) Vygorodka in the VVER440FC benchmark problem (b) planar MOC cells in nTRACER.

As for modeling the outer structure, it is reasonable to fill a MOC cell with the structural material if the center of mass belongs to the structure. Otherwise, with the surrounding material. The groove region in the X2 benchmark problem, which is described by a homogeneous mixture of the coolant and steel, is approximated following this modeling as shown in Figure 2.11. The fuel assembly is simply represented as a single hexagon in Figure 2.11.a. Figure 2.11.b is a magnified view of the red square region in Figure 2.11.a while the gap cell is omitted.

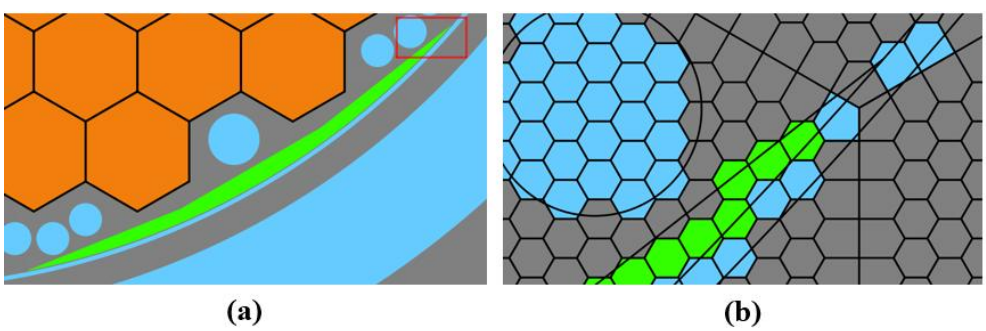

Figure 2.11. (a) Groove region in the X2 benchmark problem (b) nTRACER modelling.

2.3. CMFD Formulation for the Unstructured Geometry

Unlike rectangular geometry, cell shapes differ among CMFD meshes in hexagonal geometry. Following the definitions of the coupling coefficient and current correction coefficient,[29] the finite difference formulation at an unstructured CMFD mesh can be written as follows:

$$\sum_k^{N_s}\{(\tilde{D}_k - \hat{D}_k)s_k\phi_s - (\tilde{D}_k + \hat{D}_k)s_k\phi_k\} + \Sigma_{ts}\phi_s V_s = Q_s V_s, \quad (2.1)$$

where $\tilde{D}_k$ and $\hat{D}_k$ are the coupling coefficient and current correction coefficient with the k-th neighboring mesh, respectively, given as:

$$\tilde{D}_k = \frac{D_s D_k}{D_s l_{kn} + D_k l_{ks}}, \quad (2.2)$$

$$\hat{D}_k = \frac{-\hat{J}_k - \tilde{D}_k(\hat{\phi}_k - \hat{\phi}_s)}{\hat{\phi}_s + \hat{\phi}_k}, \quad (2.3)$$

and $\hat{J}_k$, $\hat{\phi}_k$, and $\hat{\phi}_s$ are the net current and two cell-averaged fluxes at the k-th surface of the mesh determined from the previous MOC solution; ϕ_k and D_k are the mesh-averaged flux and mesh-averaged diffusion coefficient in the k-th neighboring mesh; N_s, Σ_{ts}, ϕ_s, D_s, V_s, and Q_s are the number of surfaces, mesh-averaged total macroscopic cross-section, mesh-averaged flux, mesh-averaged diffusion coefficient, area, and mesh-averaged neutron source in the mesh, respectively; s_k is the length of the k-th surface of the mesh, and l_{ks} and l_{kn} are the shortest length from the k-th surface to the mesh center and the neighboring mesh center, respectively. The notation of the energy group is omitted here. The unstructured CMFD formulation is enabled by applying flexibility to the surface length, mesh width, and the number of neighboring meshes. In Figure 2.12, the construction of the CMFD formulation parameters for the super-cell split by the core boundary is represented.

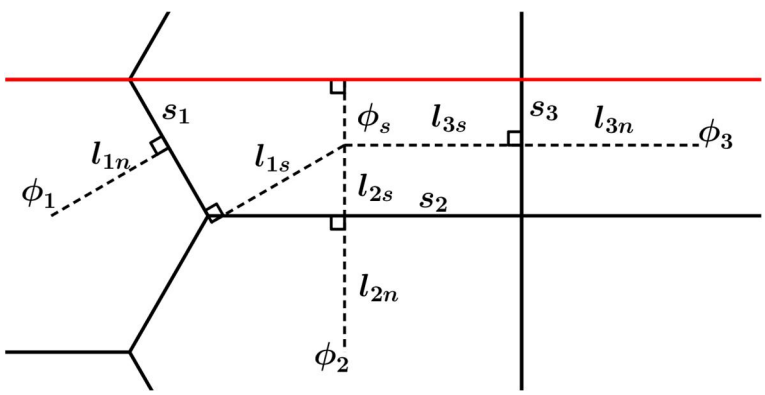

Figure 2.12. Construction of the CMFD formulation parameters for the boundary mesh in hexagonal geometry.

The gap cell thicknesses in the VVER440FC and KAERI benchmark problems are 0.25 cm and 0.02 cm, respectively, while the fuel pin pitches in the two problems are 1.23 cm and 1.275 cm, respectively. Neutron moderation in the gap cells, where

the pure moderator is filled, has less significance in the analyses of VVER cores due to its relatively small cell area. On the other hand, the number of CMFD meshes for the gap cells counts six times the number of fuel pins along the assembly surface in the *elongated* model as shown in Figure 2.13.a. Inefficiency would occur in CMFD calculations by incorporating CMFD meshes for the gap cells in that a significant computing resource is consumed additionally while solution accuracy is improved little. Thus, the super pin scheme, which is to homogenize the periphery fuel cell and gap cell into one cell in the CMFD calculation as shown in Figure 2.13.b., is examined in nTRACER. The homogenized macroscopic cross-section in super pins used in the CMFD calculation is obtained as the average value of reaction rate divided by flux. This value is calculated by using the area weight of the FSRs incorporated in the super pin. The flux change in the super pin determined by the CMFD calculation is used uniformly in the flux update for those FSRs.

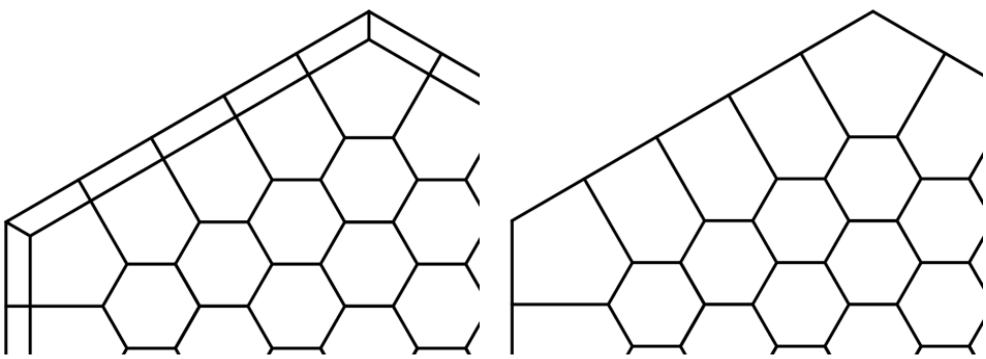

Figure 2.13. Construction of CMFD meshes with (a) MOC pins and (b) Super pins.

The performance of CMFD calculations with two mesh schemes and two scattering order options are compared for the 2D VVER core problems. The comparison results are summarized in Table 2.1 and Table 2.2, where 'MP' and 'SP' are the MOC pin scheme and super pin scheme, respectively; 'V10' and 'V4' are the KAERI and VVER440FC benchmark problems, respectively; and 'RT', 'CMFD' and 'Total' are the ray tracing time, CMFD calculation time, and total computing time, respectively. The total computing time is reduced due to the significant reduction in CMFD calculation time while the ray tracing time does not change. The reduction in CMFD calculation time does not change by the scattering order option nor geometric symmetry of the problem while it increases in the problems of smaller core size. The reduction in total computing time is decreased in the solutions using the P2 option since the ray tracing time accounts mainly for the total computing time.

The CMFD calculation time and total computing time are reduced by up to 39 % and 17 %, respectively, by using the super pin scheme. Thus, the super pin scheme is employed in nTRACER for the hexagonal geometry core problems in the following.

Table 2.1. Comparison results for the 2D VVER core problems with the P0 option between two CMFD pin schemes.

Case		MP computing time (s)			Reduction by SP (%)		
		RT	CMFD	Total	RT	CMFD	Total
1/6 Core	V10 V01	513	697	1,322	0	24	13
	V10 V05	418	538	1,063	0	27	9
	V10 V09	410	492	1,007	0	25	12
	V4	285	87	439	0	37	7
Full Core	V10 V01	2,770	3,776	7,078	-2	24	12
	V10 V05	2,242	2,875	5,644	3	30	17
	V10 V09	2,209	2,622	5,355	-1	27	13
	V4	1,402	467	2,206	1	39	9

Table 2.2. Comparison results for the 2D VVER core problems with the P2 option between two CMFD pin schemes.

Case		MP Computing time (s)			Reduction by SP (%)		
		RT	CMFD	Total	RT	CMFD	Total
1/6 Core	V10 V01	1,481	533	2,124	-1	22	5
	V10 V05	1,460	566	2,134	-1	24	6
	V10 V09	1,509	515	2,133	1	28	8
	V4	763	87	920	0	38	4
Full Core	V10 V01	9,517	3,052	13,131	1	28	7
	V10 V05	8,657	3,128	12,336	0	27	7
	V10 V09	8,808	2,756	12,115	0	28	6
	V4	4,410	461	5,219	-1	39	3

Chapter 3. Parallelization of the Hexagonal Ray Tracing Calculation with the ADD Scheme

With the original parallelization scheme of the nTRACER code, which is to divide the time-consuming entire ray tracing task into smaller tasks by grouping rays in the azimuthal direction, some large 3D core problems cannot be solved in a computing cluster with limited memory. This limitation is because the rays encompass the entire core region, and each thread tracing a group of the rays requires the ray segment information across the core. Memory for this information can be huge in hexagonal ray tracing involving much more complicated FSR structures than the rectangular cases. This excessive memory burden can be resolved by employing the assembly-wise domain decomposition (ADD), which is to let each thread trace only the rays belonging to an assembly. In the following, the overall parallelization scheme of the nTRACER ray tracing calculation with the hexagonal ADD scheme is described first. Then the specific methods to enable the ADD scheme including the angular flux update method at the assembly surface, three-color method, and angular flux storage scheme (AFSS) are detailed in the subsequent subsections.

3.1. Assembly-wise Decomposition of the Planar Ray Tracing Domain

The MOC ray tracing calculation outlined in the previous section requires considerable computing time associated with the tremendous number of ray segments. Incorporating the effect of anisotropic scattering, which is needed for enhancing solution accuracy, is the additional factor to increase computing time. With the P_2 scattering source, the memory for FSRs is increased six times to store the region-averaged angular fluxes. This memory can be tremendous because the number of FSRs is huge (about 1,800,000 in the 2D KAERI one-sixth core problem and six times it for the full core problem).

In the angle-wise parallelization for the ray tracing calculation, which was the original nTRACER parallel computing scheme, a group of cyclic rays are swept in parallel by different CPU threads. It is necessary to allocate the memory for the FSRs in the whole core to each thread since every FSR should be swept during the ray tracing. Thus, some large problems with limited memory cannot be solved with angle-wise parallelization. This limitation is worsened by the AFSS needed for anisotropic scattering treatment. In this regard, the ADD scheme to let each thread trace rays in one assembly is tried here so that the storage of FSR information is

needed only for the assemblies being computed currently, and thus memory reduction is possible. While the ADD is performed originally by using the distributed parallelism,[30]–[31] the shared memory parallelism using the OpenMP constructs is exploited here following the nTRACER parallelism. The algorithm of the nTRACER MOC sweeps with the ADD scheme is presented in Figure 3.1. The nTRACER ray tracing calculation for a 3D VVER core problem is performed plane-by-plane using MPI for the distributed memory parallelism. In the ADD calculation, the ray tracing domain at each plane is decomposed into assemblies using OpenMP for the shared memory parallelism. Each thread sweeps several assemblies since the number of assemblies is usually larger than the number of available threads. Load balancing is achieved by using the OpenMP *guided* scheduling.

```
Algorithm MOC sweep for nTRACER
do Energy group iterations
  do Energy groups
    do Planes ! MPI parallelization
      do Inner iterations
        Update P0 scattering source and higher-order scattering source moment
      do Assemblies ! OpenMP parallelization (ADD)
        Update anisotropic scattering source
        do Forward & Backward
          do Assembly rays
            do Cells
              do Segments
                do Polar angles
                  Calculate segment angular flux change
                  Update segment outgoing angular flux
                  Calculate FSR scalar flux
                end do
              Calculate cell current
              end do
            end do
          end do
        end do
      end do
      Update assembly angular flux
      end do
    end do
  end do
end do
```

Figure 3.1. Algorithm of the nTRACER MOC sweeps with the ADD scheme.

The ADD is implemented with dynamic memory allocation, which is to allocate the memory needed for ray tracing for an assembly only when a thread for that assembly performs ray tracing. This memory is deallocated once the ray tracing is done. Parallel computing is done by assigning one thread to one assembly such that the number of simultaneously calculated assemblies is the same as the number of

threads available on each node. The total memory allocated at a time during the ray tracing calculation is thus proportional to the number of available threads, which is usually much fewer than the number of assemblies in a plane. By this method, the memory requirement for simultaneous ray tracing with the ADD scheme can be significantly less than the angle-wise parallelization. However, the actual reduction cannot be that much because additional nontrivial memory to save the incoming angular flux shape at the assembly surfaces is required. Nonetheless, considerable memory saving is possible with the ADD scheme. Updating the assembly incoming angular flux is described in the following sub-section.

3.2. Assembly Incoming Angular Flux Update

A significant drawback in the ADD is that a ray cannot be traced continuously throughout the core since the ray within an assembly should start from the assembly surface. Thus, the incoming angular flux at the assembly surface cannot be taken as the outgoing angular flux of its neighboring assembly. The incoming angular flux at each assembly surface should be taken from the previous MOC iteration, and it requires storing the angular flux information at the assembly surfaces, which is another drawback to increase memory requirement. The lag in updating the incoming angular fluxes at the assembly surfaces would deteriorate the convergence of the MOC calculation. However, this deterioration can be relaxed by updating the incoming angular fluxes by using the CMFD calculation results. There are three variables of which the change by the CMFD calculation can be used for this update: the scalar flux, partial current, and P1 approximation of the angular flux. The partial currents, which can be determined by two node average fluxes and the interface surface flux obtained from the CMFD calculation, are used to update the incoming angular fluxes at the assembly surface similarly to the method implemented in MPACT.[31]–[32] Specifically, the stored incoming angular flux $\tilde{\varphi}_s$ of the previous MOC calculation at the surface of each assembly for each energy group is used to determine the new angular flux φ_s by using the scalar flux and net current determined at the surface between the i-th and the $i+1$-th CMFD mesh as:

$$\boldsymbol{\varphi_s} = \frac{\boldsymbol{J_s^{CMFD+}}}{\boldsymbol{J_s^{MOC+}}} \tilde{\boldsymbol{\varphi}}_{\boldsymbol{s}}, \tag{3.1}$$

$$\boldsymbol{J_s^{MOC+}} = \frac{\mathbf{1}}{\mathbf{4}} \boldsymbol{\phi_s^{MOC}} + \frac{\mathbf{1}}{\mathbf{2}} \boldsymbol{J_s^{MOC}}, \tag{3.2}$$

$$\boldsymbol{J_s^{CMFD+}} = \frac{\mathbf{1}}{\mathbf{4}} \boldsymbol{\phi_s^{CMFD}} + \frac{\mathbf{1}}{\mathbf{2}} \boldsymbol{J_s^{CMFD}}, \tag{3.3}$$

$$\boldsymbol{\phi_s^{CMFD}} = \tilde{\boldsymbol{\alpha}}_{\boldsymbol{i}} \boldsymbol{\phi_i^{CMFD}} + (\mathbf{1} - \tilde{\boldsymbol{\alpha}}_{\boldsymbol{i}}) \boldsymbol{\phi_{i+1}^{CMFD}} + \hat{\boldsymbol{\alpha}}_{\boldsymbol{i}} \left(\boldsymbol{\phi_i^{CMFD}} + \boldsymbol{\phi_{i+1}^{CMFD}} \right), \tag{3.4}$$

$$\hat{\boldsymbol{\alpha}}_{\boldsymbol{i}} = -\frac{\tilde{\alpha}_i \phi_i^{MOC} + (1-\tilde{\alpha}_i) \phi_{i+1}^{MOC} - \phi_s^{MOC}}{\phi_i^{MOC} + \phi_{i+1}^{MOC}}, \tag{3.5}$$

$$\tilde{\alpha}_i = \frac{D_i/h_i}{D_i/h_i + D_{i+1}/h_{i+1}}, \tag{3.6}$$

where ϕ_s^{MOC}, J_s^{MOC} and ϕ_i^{MOC} are the surface scalar flux, surface net current and cell-averaged scalar flux at the i-th mesh, respectively, determined from the previous MOC calculation; and D_i and h_i are the diffusion coefficient and size of the i-th mesh, respectively. The CMFD surface current, J_s^{CMFD}, is obtained by the ordinary CMFD net current relation involving the current correction coefficient $\hat{D}_i$. Note that the similar correction coefficient $\hat{\alpha}_i$ is introduced for the surface flux calculation from the mesh average flux. The plus sign appearing in Eqs. (3.2) and (3.3) changes to the minus sign if the incoming angular flux is in the opposite direction, namely from mesh *i+1* to *i*. In the hexagonal CMFD calculation with the *elongated model*, the CMFD meshes have different shapes. Therefore, the $\tilde{\alpha}_i$ calculation represented in Eq. (3.6) is extended to use two different mesh sizes.

3.3. Three-color Scheme

The STREAM DWCC code developed at UNIST uses the red-black scheme to achieve high efficiency in angular flux communication.[33] This scheme arranges the surfaces and directions in the assembly angular flux update with an index determined on a checkerboard. On the other hand, the color scheme used in nTRACER is to perform simultaneous ray tracing calculations for a group of assemblies belonging to the same color group. After all assemblies belonging to one color are swept, assemblies belonging to the next color are swept in sequence. Note that assemblies belonging to a color are swept in parallel by threads. This scheme provides an important advantage in that the outgoing angular fluxes of one colored assembly can be used in updating the incoming angular fluxes of the other colored assemblies.

Possible color schemes in hexagonal geometry are illustrated in Figure 3.2: none, two red/black schemes, and the three-color scheme. All assemblies are swept at once by using threads in a random order without any color scheme (‘w/o C.’). On the other hand, the update of angular fluxes in the assembly surface is invoked between sweeping assemblies belonging to different colors in case of using a color scheme. Red and black in the red/black scheme might be alternately assigned to assemblies (‘RB 1’) or arranged in a strip (‘RB 2’). Three groups of assemblies in the three-color scheme can be swept by following two iteration patterns (‘RGB1’ and ‘RGB2’) as described in Table 3.1.

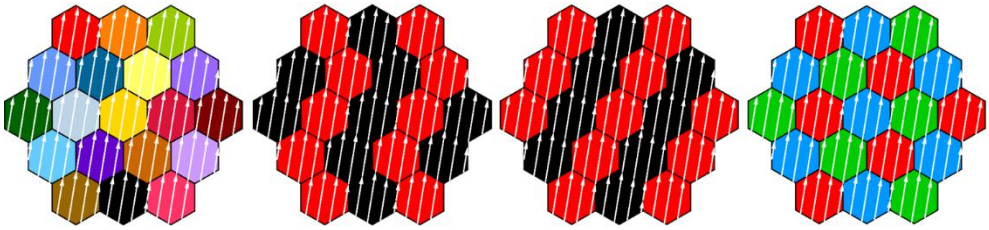

Figure 3.2. Color schemes in hexagonal geometry.

Table 3.1. Iteration patterns in the RGB scheme.

Iterations	1	2	3	4	…
RGB 1	(R, G, B)	(B, G, R)	(R, G, B)	(B, G, R)	…
RGB 2	(R, G, B)	(G, B, R)	(B, R, G)	(R, G, B)	…

The ADD performance with different color schemes is examined for the small VVER core problems, which employ the assemblies and problem cases of the KAERI benchmark and follow the loading pattern of the C5G7 H benchmark problem. The examination results are summarized in Table 3.2, and error reductions in the ADD calculations with different color schemes are illustrated in Figure 3.3 and Figure 3.4. The ray tracing time is increased in most cases since sweeping assemblies in a sequence of color deteriorates calculation parallelization. This drawback is aggravated for the one-sixth core problems due to unevenness in assembly area. However, a necessity to mitigate the instability in ADD calculations justifies a few increase in computing time. Thus, it is concluded to employ the three-color scheme in hexagonal ADD calculations for the full core since one MOC iteration is saved for the V01 full core problem only by using the three-color scheme. The first iteration pattern of the three-color scheme is employed in the following though the difference between the two patterns is negligible.[34]

Table 3.2. Ray tracing time (s) for the small core problem with color schemes.

Cases		w/o C.	RB1	RB2	RGB1	RGB2
1/6 Core	V01	845	1,283	1,270	1,890	1,897
	V05	605	1,063	1,057	1,560	1,563
	V09	610	1,050	1,050	1,550	1,567
Full Core	V01	2,363	2,570	2,560	2,210	2,220
	V05	1,683	2,120	2,123	1,883	1,857
	V09	1,670	2,113	2,100	1,827	1,830

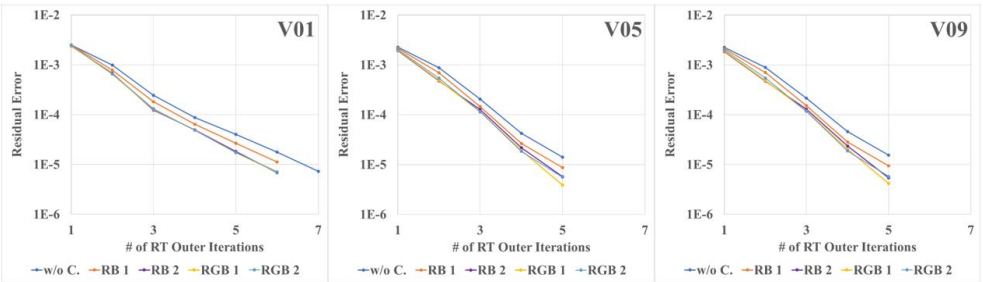

Figure 3.3. Error reduction with different color schemes for one-sixth core problems.

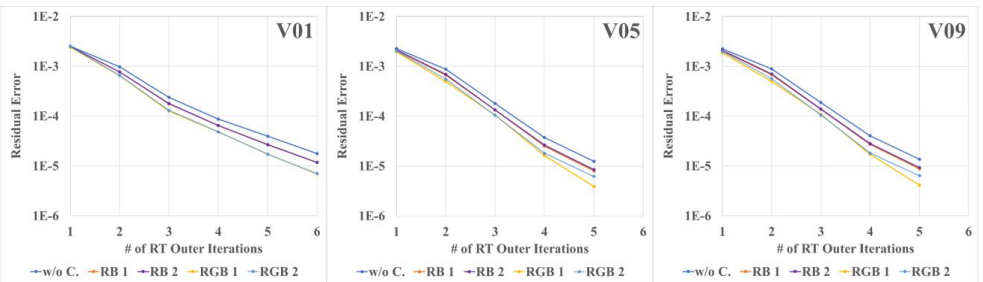

Figure 3.4. Error reduction with different color schemes for full core problems.

The impact of the three-color scheme on the ray tracing calculation with the hexagonal ADD scheme is examined for the 2D VVER core problems as shown in Figure 3.5, where 'RGB' is the three-color scheme. In the one-sixth symmetry case, the total ray tracing time is increased since OpenMP load balancing for the ray tracing calculation is deteriorated by adding three-color iterations to assembly iterations. On the other hand, the total ray tracing time for the 2D KAERI V06, V09 full core problem is reduced by 9~13 % by saving one ray tracing iteration. Thus, the three-color scheme is used only for the full core problems in the following.

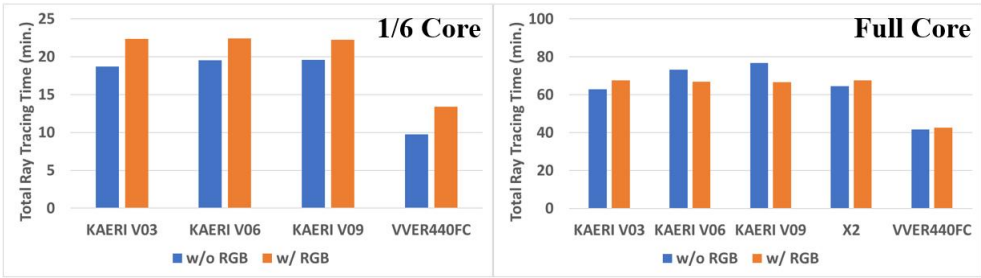

Figure 3.5. Total ray tracing time for the 2D VVER core problems *with* and *without* the three-color scheme.

3.4. Angular Flux Storage Scheme

The l-th order Legendre angular expanded m-th flux moment ϕ_l^m for the energy group g at the position $\vec{r}$ in the planar MOC calculation with anisotropic scattering is obtained as follows:

$$\boldsymbol{\phi}_{g,l}^{\boldsymbol{m}}(\vec{\boldsymbol{r}}) = \frac{\hat{\boldsymbol{\phi}}_{g,l}^{\boldsymbol{m}}(\vec{\boldsymbol{r}})}{\boldsymbol{\Sigma}_{\boldsymbol{tg}}(\vec{\boldsymbol{r}})\boldsymbol{A}(\vec{\boldsymbol{r}})} + \frac{\boldsymbol{Q}_{g,l}^{\boldsymbol{m}}(\vec{\boldsymbol{r}})}{\boldsymbol{\Sigma}_{\boldsymbol{tg}}(\vec{\boldsymbol{r}})}, \tag{3.7}$$

$$\hat{\boldsymbol{\phi}}_{g,l}^{\boldsymbol{m}}(\vec{\boldsymbol{r}}) = \sum_{\hat{\boldsymbol{\Omega}}} \boldsymbol{\omega}_{\hat{\boldsymbol{\Omega}}} \boldsymbol{\sin\theta}\, \boldsymbol{\Delta}_{\boldsymbol{\alpha}} \left(\boldsymbol{\varphi}_{\boldsymbol{g}}^{\boldsymbol{in}}(\vec{\boldsymbol{r}},\hat{\boldsymbol{\Omega}}) - \boldsymbol{\varphi}_{\boldsymbol{g}}^{\boldsymbol{out}}(\boldsymbol{s},\vec{\boldsymbol{r}},\hat{\boldsymbol{\Omega}})\right) \boldsymbol{Y}_{\boldsymbol{l}}^{\boldsymbol{m}*}(\hat{\boldsymbol{\Omega}}), \tag{3.8}$$

$$\boldsymbol{Q}_{g,l}^{\boldsymbol{m}}(\vec{\boldsymbol{r}}) = \boldsymbol{\delta}_{0l}\boldsymbol{Q}_{fg}(\vec{\boldsymbol{r}}) + \sum_{g'} \boldsymbol{\Sigma}_{s,g'\to g}^{\boldsymbol{l}}(\vec{\boldsymbol{r}})\boldsymbol{\phi}_{g',l}^{\boldsymbol{prv,m}}(\vec{\boldsymbol{r}}), \tag{3.9}$$

where Σ_t is the total cross-section; A is the source mesh area in ray tracing; ω is the weighting of solid angle $\hat{\Omega}$; θ is the polar angle; Δ is the ray spacing; α is the azimuthal angle; φ^{in} is the incoming angular flux; φ^{out} is the outgoing angular flux; s is the segment length; Q_f is the fission source; Σ_s^l is the l-th order Legendre angular expanded scattering cross-section; ϕ^{prv} is the angular flux moment obtained from the previous step.

In the flux moment storage scheme (FMSS), $\hat{\phi}_{g,l}^m$ is accumulated in the course of tracing each ray segment. This scheme is quite intuitive and especially effective in the P0 calculation. It requires, however, enormous multiplication operations in the P2 calculation. On the contrary, $\hat{\phi}_{g,l}^m$ is calculated as the weighted sum of $\hat{\varphi}_g$, the difference between two angular fluxes in the AFSS.[35]

$$\hat{\boldsymbol{\phi}}_{g,l}^{\boldsymbol{m}}(\vec{\boldsymbol{r}}) = \sum_{\hat{\boldsymbol{\Omega}}} \boldsymbol{\omega}_{\hat{\boldsymbol{\Omega}}} \boldsymbol{\sin\theta}\, \boldsymbol{\Delta}_{\boldsymbol{\alpha}} \hat{\boldsymbol{\varphi}}_{\boldsymbol{g}}(\boldsymbol{s},\vec{\boldsymbol{r}},\hat{\boldsymbol{\Omega}}) \boldsymbol{Y}_{\boldsymbol{l}}^{\boldsymbol{m}*}(\hat{\boldsymbol{\Omega}}), \tag{3.10}$$

$$\hat{\boldsymbol{\varphi}}_{\boldsymbol{g}}(\boldsymbol{s},\vec{\boldsymbol{r}},\hat{\boldsymbol{\Omega}}) = \boldsymbol{\varphi}_{\boldsymbol{g}}^{\boldsymbol{in}}(\vec{\boldsymbol{r}},\hat{\boldsymbol{\Omega}}) - \boldsymbol{\varphi}_{\boldsymbol{g}}^{\boldsymbol{out}}(\boldsymbol{s},\vec{\boldsymbol{r}},\hat{\boldsymbol{\Omega}}). \tag{3.11}$$

This scheme requires storing the average angular flux information during ray

tracing. The moment calculation is done at the end of the ray tracing calculation in this scheme. The benefit of computing time saving attainable by avoiding expensive moment calculations during the ray tracing calculation justifies the increased memory usage.

The impact of the AFSS on computing time for the two ray tracing calculations *with* and *without* the ADD scheme, which are examined for the 2D VVER core problems, is exactly the opposite as shown in Figure 3.6. The total ray tracing time is increased significantly in the calculation without the ADD scheme due to a huge fetching overhead induced by the enormous memory size of the angular flux change. On the other hand, the total ray tracing time is reduced by 10~26% in the calculation with the ADD scheme by saving multiplication operations in the P2 calculation. Thus, the AFSS is used only in the calculation with the ADD scheme in the following.

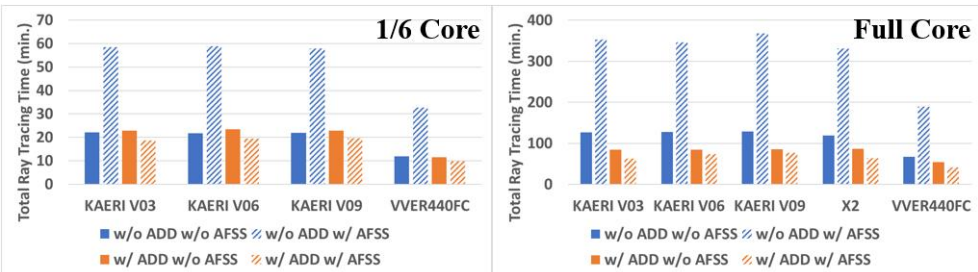

Figure 3.6. Total ray tracing time for the 2D VVER core problems *with* and *without* the AFSS.

The algorithm of the nTRACER MOC sweeps with the hexagonal ADD scheme, three-color scheme, and AFSS is represented in Figure 3.7. Compared to Figure 3.1, color iterations are added to assembly iterations, and the scalar flux is calculated once all assembly rays are swept.

```
Algorithm MOC sweep for nTRACER
do Energy group iterations
  do Energy groups
    do Planes ! MPI parallelization
      do Inner iterations
        Update P0 scattering source and higher-order scattering source moment
        do Colors ! 3 color scheme
          do Assemblies ! OpenMP parallelization (ADD)
            Update anisotropic scattering source
            do Forward & Backward
              do Assembly rays
                do Cells
                  do Segments
                    do Polar angles
                      Calculate segment angular flux change
                      Update segment outgoing angular flux
                    end do
                  Calculate cell current
                  end do
                end do
              end do
            end do
            Calculate scalar flux ! AFSS
          end do
        Update assembly angular flux
        end do
      end do
    end do
  end do
end do
```

Figure 3.7. Algorithm of the nTRACER MOC sweeps with the ADD scheme, three-color scheme, and AFSS.

Chapter 4. Development of the Unstructured Nodal Method in RENUS

So far, the capability of handling geometric deformation of a core has been attained only in the finite difference method, finite element method, and Monte Carlo solutions, which require dividing the problem domain into substantial meshes to obtain sufficient accuracy. Meanwhile, the nodal solution based on polynomial expansions, which exploits a smaller computing resource, can also be expanded to the unstructured geometry by calculating the integrals of the polynomial expressions within the given domain.

A nodal code, RENUS analyzes the neutronic characteristics of a 3D hexagonal geometry core by employing the planar solutions and axial solution as shown in Figure 4.1. For each plane, the triangle-based polynomial expansion nodal (T-PEN) method and corner point balance (CPB) solution are alternately invoked to solve the decoupled planar diffusion equations. The point fluxes used in the T-PEN calculations are updated from the CPB solutions while the surface currents and assembly fluxes used in the CPB calculations are updated from the T-PEN solutions again. The axial coupling between planes is resolved by the 1D nodal expansion method (NEM) solution. The axial leakages used in the T-PEN calculations are updated from the NEM solutions while the transverse leakages and assembly fluxes used in the NEM calculations are updated from the T-PEN solutions again. The axial leakage source distribution approximated as the third polynomial expression for each assembly is inputted to the T-PEN calculations. The nodal calculations are accelerated by updating the assembly fluxes by using the 3D CMFD formulation. The 3D CMFD formulation uses the surface currents determined by the nodal solutions again.

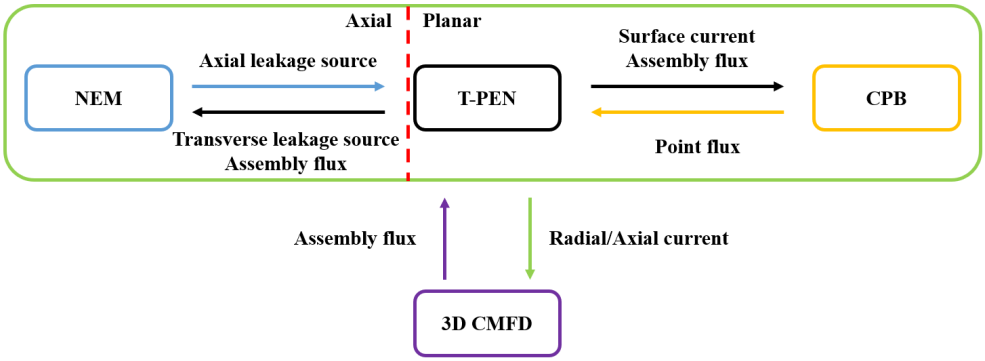

Figure 4.1. Code flow of RENUS.

This section introduces the method to calculate the curvilinear and surface integrals of polynomials in arbitrary geometry. In the subsequent subsections, the T-PEN method and CPB solution in regularly structured geometry are introduced, and the expansion of those calculations to the unstructured geometry by using the method described in Subsection 4.1. is described.

4.1. Polynomial Integral Calculations in Arbitrary Geometry

The nodal method is to approximate the flux distribution in a fuel assembly size coarse mesh, into which the cross-sections are homogenized, as an expression of continuous functions such as polynomial, exponential and trigonometrical functions. The physical constraints, e.g., the diffusion equation, flux and current continuity, and leakage balance are employed in each mesh to determine the unknown coefficients in the flux expression. The system of the physical constraints can be established by incorporating the physical variables including the mesh-averaged flux and current, of which the expressions are determined from the flux expression. The number of unknowns in the system can be reduced by substituting the unknown variables with the inputs determined from previous calculations or equations of other unknown variables. The flux expression can be uniquely determined by solving the system as the number of unknowns becomes equal to the number of flux expansion coefficients. Thus, the nodal method can be expanded to the irregularly deformed geometry by expressing edge-averaged and area-averaged variables as an equation of other variables in an unstructured mesh. It needs to calculate the curvilinear and surface integrals of basic functions in arbitrary geometry since those integrals are incorporated in variable expressions.

In the two arbitrary segments stretching from (x_1, y_1) to (x_2, y_2) which are

parallel to the y-axis or *not*, respectively, shown in Figure 4.2, the surface flux $\bar{\phi}_l$ and current $\bar{J}_l$ are defined as follows:

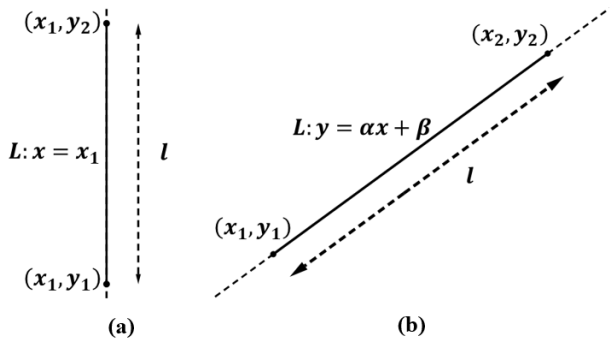

Figure 4.2. Arbitrary segments (a) *parallel* to the y-axis or (b) *not*.

$$\bar{\boldsymbol{\phi}}_{\boldsymbol{l}} = \frac{\mathbf{1}}{\boldsymbol{y_2 - y_1}} \int_{y_1}^{y_2} \boldsymbol{\phi}(\boldsymbol{x}, \boldsymbol{y})|_{x=x_1} \boldsymbol{dx} \text{ while } \boldsymbol{x_1 = x_2}, \tag{4.1}$$

$$\bar{\boldsymbol{\phi}}_{\boldsymbol{l}} = \frac{\mathbf{1}}{\boldsymbol{x_2 - x_1}} \int_{x_1}^{x_2} \boldsymbol{\phi}(\boldsymbol{x}, \boldsymbol{y})|_{y=\alpha x+\beta} \boldsymbol{dx} \text{ while } \boldsymbol{x_1 \neq x_2}, \tag{4.2}$$

$$\bar{\boldsymbol{J}}_{\boldsymbol{l}} = -\boldsymbol{D} \frac{\mathbf{sgn}(\boldsymbol{x_1})}{\boldsymbol{l}} \int_{y_1}^{y_2} \frac{\boldsymbol{\partial}}{\boldsymbol{\partial x}} \boldsymbol{\phi}(\boldsymbol{x}, \boldsymbol{y})\Big|_{x=x_1} \boldsymbol{dy} \text{ while } \boldsymbol{x_1 = x_2}, \tag{4.3}$$

$$\bar{\boldsymbol{J}}_{\boldsymbol{l}} = -\boldsymbol{D} \frac{\mathbf{sgn}(\boldsymbol{\beta})}{\boldsymbol{l}} \begin{pmatrix} -\boldsymbol{\alpha} \int_{x_1}^{x_2} \frac{\boldsymbol{\partial}}{\boldsymbol{\partial x}} \boldsymbol{\phi}(\boldsymbol{x}, \boldsymbol{y})\Big|_{y=\alpha x+\beta} \boldsymbol{dx} \\ + \int_{x_1}^{x_2} \frac{\boldsymbol{\partial}}{\boldsymbol{\partial y}} \boldsymbol{\phi}(\boldsymbol{x}, \boldsymbol{y})\Big|_{y=\alpha x+\beta} \boldsymbol{dx} \end{pmatrix} \text{ while } \boldsymbol{x_1 \neq x_2}, \tag{4.4}$$

where sgn is a sign function; D is the homogeneous diffusion coefficient; l is the segment length; and $\phi(x, y)$ is the flux expression.

The surface flux of $\phi(x, y)$ polynomials used in the T-PEN method and CPB solution can be obtained by using Table 4.1, in which u, p, v and q are defined as follows:

Table 4.1. Polynomial curvilinear integrals in arbitrary segment.

	$\bar{\phi}_l$	$\times$
$\mathbf{1}$	$\mathbf{1}$	$\mathbf{1}$
x	$x_1 + x_2$	
y	$y_1 + y_2$	
u	$u_1 + u_2$	$\frac{1}{2}$
p	$p_1 + p_2$	
v	$v_1 + v_2$	
q	$q_1 + q_2$	
x^2	$x_1^2 + x_1x_2 + x_2^2$	
y^2	$y_1^2 + y_1y_2 + y_2^2$	
u^2	$u_1^2 + u_1u_2 + u_2^2$	$\frac{1}{3}$
p^2	$p_1^2 + p_1p_2 + p_2^2$	
v^2	$v_1^2 + v_1v_2 + v_2^2$	
q^2	$q_1^2 + q_1q_2 + q_2^2$	
x^3	$(x_1 + x_2)(x_1^2 + x_2^2)$	
y^3	$(y_1 + y_2)(y_1^2 + y_2^2)$	
u^3	$(u_1 + u_2)(u_1^2 + u_2^2)$	$\frac{1}{4}$
p^3	$(p_1 + p_2)(p_1^2 + p_2^2)$	
v^3	$(v_1 + v_2)(v_1^2 + v_2^2)$	
q^3	$(q_1 + q_2)(q_1^2 + q_2^2)$	
x^4	$x_1^4 + x_1^3x_2 + x_1^2x_2^2 + x_1x_2^3 + x_2^4$	
y^4	$y_1^4 + y_1^3y_2 + y_1^2y_2^2 + y_1y_2^3 + y_2^4$	
u^4	$u_1^4 + u_1^3u_2 + u_1^2u_2^2 + u_1u_2^3 + u_2^4$	$\frac{1}{5}$
p^4	$p_1^4 + p_1^3p_2 + p_1^2p_2^2 + p_1p_2^3 + p_2^4$	
v^4	$v_1^4 + v_1^3v_2 + v_1^2v_2^2 + v_1v_2^3 + v_2^4$	
q^4	$q_1^4 + q_1^3q_2 + q_1^2q_2^2 + q_1q_2^3 + q_2^4$	

$$\boldsymbol{u} = -\frac{1}{2}\left(\boldsymbol{x} + \sqrt{3}\boldsymbol{y}\right), \tag{4.5}$$

$$\boldsymbol{p} = -\frac{1}{2}\left(\boldsymbol{x} - \sqrt{3}\boldsymbol{y}\right), \tag{4.6}$$

$$\boldsymbol{v} = -\frac{1}{2}\left(\boldsymbol{y} - \sqrt{3}\boldsymbol{x}\right), \tag{4.7}$$

$$\boldsymbol{q} = -\frac{1}{2}\left(\boldsymbol{y} + \sqrt{3}\boldsymbol{x}\right). \tag{4.8}$$

Note that the equations in the table are valid whether the segment is *parallel* to the y-axis or *not*. For example, the surface flux in arbitrary segment with the flux shape of x^3 is obtained as follows:

$$\bar{\boldsymbol{\phi}}_{\boldsymbol{l}} = \frac{1}{y_2 - y_1}\int_{y_1}^{y_2} \boldsymbol{x^3}\,\boldsymbol{dx} = \frac{1}{4}(\boldsymbol{x_1} + \boldsymbol{x_1})\left(\boldsymbol{x_1^2} + \boldsymbol{x_1^2}\right) \text{ while } \boldsymbol{x_1 = x_2}, \tag{4.9}$$

$$\bar{\boldsymbol{\phi}}_{\boldsymbol{l}} = \frac{1}{x_2 - x_1}\int_{x_1}^{x_2} \boldsymbol{x^3}\,\boldsymbol{dx} = \frac{1}{4}(\boldsymbol{x_1} + \boldsymbol{x_2})\left(\boldsymbol{x_1^2} + \boldsymbol{x_2^2}\right) \text{ while } \boldsymbol{x_1 \neq x_2}. \tag{4.10}$$

The curvilinear integral terms in Eq. (4.3) and Eq. (4.4) can be obtained by multiplying their coefficients to the surface flux of $\frac{\partial}{\partial x}\phi(x,y)$ and $\frac{\partial}{\partial y}\phi(x,y)$ polynomials, respectively, which can be determined by using Table 4.1.

The areal flux $\bar{\phi}_V$, flux moments $\tilde{\phi}_x$ and $\tilde{\phi}_y$, flux Laplacian operator $\nabla^2\bar{\phi}_V$, and flux Laplacian operator moments $\nabla^2\tilde{\phi}_x$ and $\nabla^2\tilde{\phi}_y$ in an arbitrary closed polygon with an area of A are defined as follows:

$$\bar{\boldsymbol{\phi}}_{\boldsymbol{V}} = \frac{1}{A}\int \boldsymbol{\phi}(\boldsymbol{x},\boldsymbol{y})\boldsymbol{dS}, \tag{4.11}$$

$$\tilde{\boldsymbol{\phi}}_{\boldsymbol{x}} = \frac{1}{A}\int \boldsymbol{x}\boldsymbol{\phi}(\boldsymbol{x},\boldsymbol{y})\boldsymbol{dS}, \tag{4.12}$$

$$\tilde{\boldsymbol{\phi}}_{\boldsymbol{y}} = \frac{1}{A}\int \boldsymbol{y}\boldsymbol{\phi}(\boldsymbol{x},\boldsymbol{y})\boldsymbol{dS}, \tag{4.13}$$

$$\boldsymbol{\nabla^2}\bar{\boldsymbol{\phi}}_{\boldsymbol{V}} = \frac{1}{A}\int \left(\frac{\partial^2}{\partial x^2}+\frac{\partial^2}{\partial y^2}\right)\boldsymbol{\phi}(\boldsymbol{x},\boldsymbol{y})\boldsymbol{dS}, \tag{4.14}$$

$$\boldsymbol{\nabla^2}\tilde{\boldsymbol{\phi}}_{\boldsymbol{x}} = \frac{1}{A}\int \boldsymbol{x}\left(\frac{\partial^2}{\partial x^2}+\frac{\partial^2}{\partial y^2}\right)\boldsymbol{\phi}(\boldsymbol{x},\boldsymbol{y})\boldsymbol{dS}, \tag{4.15}$$

$$\boldsymbol{\nabla^2}\tilde{\boldsymbol{\phi}}_{\boldsymbol{y}} = \frac{1}{A}\int \boldsymbol{y}\left(\frac{\partial^2}{\partial x^2}+\frac{\partial^2}{\partial y^2}\right)\boldsymbol{\phi}(\boldsymbol{x},\boldsymbol{y})\boldsymbol{dS}, \tag{4.16}$$

The arbitrary closed polygon shown in Figure 4.3 can be split into parallelograms or triangles divided by lines parallel to the y-axis. The areal variables of Eqs. (4.11)–(4.16) in this polygon can be obtained by averaging the areal variables in parallelograms or triangles with volume weight.

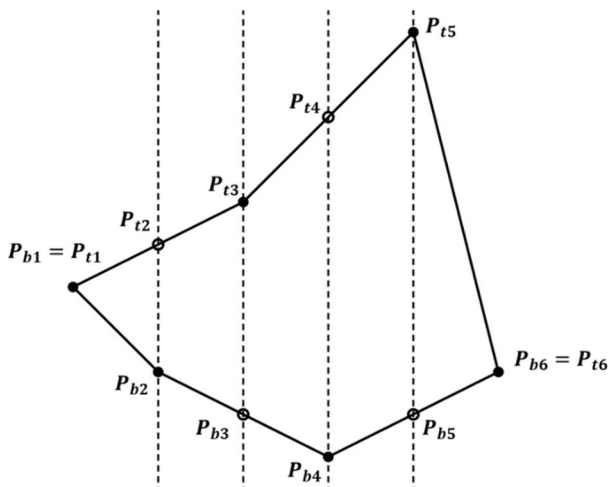

Figure 4.3. Arbitrary polygon divided by lines parallel to the y-axis.

The areal flux in one parallelogram shown in Figure 4.4 can be obtained as follows:

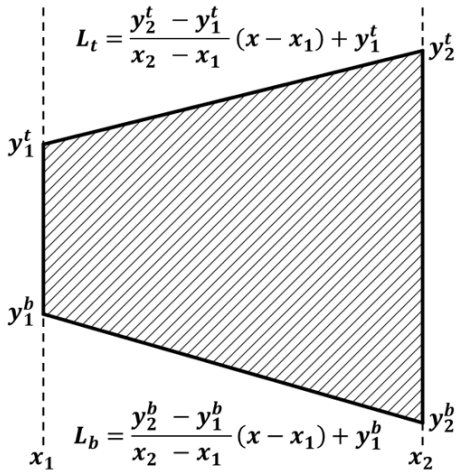

Figure 4.4. Parallelogram parallel to the y-axis.

$$\bar{\boldsymbol{\phi}}_V = \frac{1}{A}\int \boldsymbol{\phi}(x,y)\boldsymbol{dS} = \frac{1}{A}\int_{x_1}^{x_2}\int_{L_b}^{L_t} \boldsymbol{\phi}(x,y)\,\boldsymbol{dydx}, \tag{4.17}$$

$$\boldsymbol{A} = \frac{1}{2}(x_2 - x_1)\big(y_1^t - y_1^b\big)\big(y_2^t - y_2^b\big), \tag{4.18}$$

$$\int_{L_b}^{L_t} \boldsymbol{\phi}(x,y)\,\boldsymbol{dy} = \boldsymbol{F_y}\big(x, \boldsymbol{L_t}(x)\big) - \boldsymbol{F_y}\big(x, \boldsymbol{L_b}(x)\big), \tag{4.19}$$

$$\frac{\boldsymbol{\partial}}{\boldsymbol{\partial y}}\boldsymbol{F_y}(x,y) = \boldsymbol{\phi}(x,y), \tag{4.20}$$

$$\int_{x_1}^{x_2}\Big(\boldsymbol{F_y}\big(x, \boldsymbol{L_t}(x)\big) - \boldsymbol{F_y}\big(x, \boldsymbol{L_b}(x)\big)\Big)\boldsymbol{dx} = \big(\boldsymbol{G_{xt}}(x_2) - \boldsymbol{G_{xt}}(x_1)\big) - \big(\boldsymbol{G_{xb}}(x_2) - \boldsymbol{G_{xb}}(x_1)\big), \tag{4.21}$$

$$\frac{\boldsymbol{\partial}}{\boldsymbol{\partial x}}\boldsymbol{G_{xt}}(x) = \boldsymbol{F_y}\big(x, \boldsymbol{L_t}(x)\big), \tag{4.22}$$

$$\frac{\boldsymbol{\partial}}{\boldsymbol{\partial x}}\boldsymbol{G_{xb}}(x) = \boldsymbol{F_y}\big(x, \boldsymbol{L_b}(x)\big), \tag{4.23}$$

$$\bar{\boldsymbol{\phi}}_V = \frac{1}{A}\Big(\big(\boldsymbol{G_{xt}}(x_2) - \boldsymbol{G_{xt}}(x_1)\big) - \big(\boldsymbol{G_{xb}}(x_2) - \boldsymbol{G_{xb}}(x_1)\big)\Big). \tag{4.24}$$

The surface integral function $G_{xl}(x)$ in the arbitrary line $L: y = ax + b$ for x, y polynomials used in the T-PEN method and CPB solution can be obtained by using Table 4.2. $G_{xl}(x)$ for u, p, v and q polynomials can be obtained as a linear combination of $G_{xl}(x)$ for x, y polynomials.

Table 4.2. Polynomial surface integral functions in arbitrary line.

$\phi(x,y)$	$G_{xl}(x)$
1	$\frac{1}{2}ax^2+bx$
x	$\frac{1}{3}ax^3+\frac{1}{2}bx^2$
x^2	$\frac{1}{4}ax^4+\frac{1}{3}bx^3$
x^3	$\frac{1}{5}ax^5+\frac{1}{4}bx^4$
x^4	$\frac{1}{6}ax^6+\frac{1}{5}bx^5$
y	$\frac{1}{6}a^2x^3+\frac{1}{2}abx^2+\frac{1}{2}b^2x$
y^2	$\frac{1}{12}a^3x^4+\frac{1}{3}a^2bx^3+\frac{1}{2}ab^2x^2+\frac{1}{3}b^3x$
y^3	$\frac{1}{20}a^4x^5+\frac{1}{4}a^3bx^4+\frac{1}{2}a^2b^2x^3+\frac{1}{2}ab^3x^2+\frac{1}{4}b^4x$
y^4	$\frac{1}{30}a^5x^6+\frac{1}{5}a^4bx^5+\frac{1}{2}a^3b^2x^4+\frac{2}{3}a^2b^3x^3+\frac{1}{2}ab^4x^2+\frac{1}{5}b^5x$
xy	$\frac{1}{8}a^2x^4+\frac{1}{3}abx^3+\frac{1}{4}b^2x^2$
x^2y	$\frac{1}{10}a^2x^5+\frac{1}{4}abx^4+\frac{1}{6}b^2x^3$
xy^2	$\frac{1}{15}a^3x^5+\frac{1}{4}a^2bx^4+\frac{1}{3}ab^2x^3+\frac{1}{6}b^3x^2$
x^3y	$\frac{1}{12}a^2x^6+\frac{1}{5}abx^5+\frac{1}{8}b^2x^4$
x^2y^2	$\frac{1}{18}a^3x^6+\frac{1}{5}a^2bx^5+\frac{1}{4}ab^2x^4+\frac{1}{9}b^3x^3$
xy^3	$\frac{1}{24}a^4x^6+\frac{1}{5}a^3bx^5+\frac{3}{8}a^2b^2x^4+\frac{1}{3}ab^3x^3+\frac{1}{8}b^4x^2$

Note that the equations in the table are also valid in a triangle by inputting same y_1^t and y_1^b or same y_2^t and y_2^b. The areal flux moments, flux Laplacian operator and flux Laplacian operator moments of $\phi(x,y)$ polynomials can be obtained by repeating the areal flux calculation for $x\phi(x,y), y\phi(x,y), \left(\frac{\partial^2}{\partial x^2}+\frac{\partial^2}{\partial y^2}\right)\phi(x,y), x\left(\frac{\partial^2}{\partial x^2}+\frac{\partial^2}{\partial y^2}\right)\phi(x,y)$ and $y\left(\frac{\partial^2}{\partial x^2}+\frac{\partial^2}{\partial y^2}\right)\phi(x,y)$ polynomials, respectively, which can be determined by using Table 4.2.

4.2. Expansion of the T-PEN Method to the Unstructured Geometry

The T-PEN method [22] is to approximate the flux distribution in a triangle node of hexagonal assembly as a linear combination of nine polynomials as follows:

$$\phi(x,y)=c_0+a_xx+a_yy+b_xx^2+b_uu^2+b_pp^2+c_xx^3+c_uu^3+ \quad (4.25)$$

$$c_p p^3,$$

where the notation of the energy group is omitted here.

The physical variables used in the T-PEN method can be categorized into the *representative* group and the *derived* group. Each variable in the *representative* group including one areal flux $\bar{\phi}_V$, two areal flux moments $\tilde{\phi}_x$ and $\tilde{\phi}_y$, three surface fluxes $\bar{\phi}_x, \bar{\phi}_u, \bar{\phi}_p$, and three corner point fluxes ϕ_x, ϕ_u, ϕ_p can be expressed as a linear combination of nine flux expansion coefficients, and vice versa. Seven variables in the *derived* group including one areal leakage $\bar{D}_V^2$, two areal leakage moments $\tilde{D}_x^2$ and $\tilde{D}_y^2$, three surface currents $\bar{J}_x, \bar{J}_u, \bar{J}_p$, and one central leakage L_c are incorporated in the physical constraints employed to establish the response matrix. The T-PEN variables in the regular triangle node shown in Figure 4.5 are defined as follows:

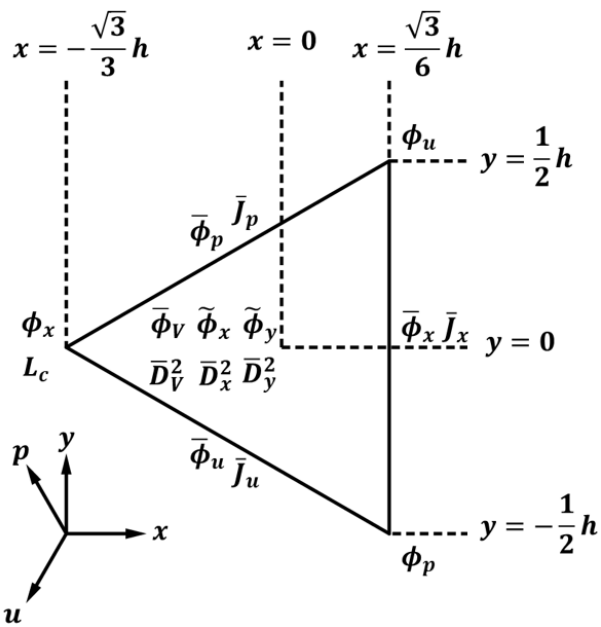

Figure 4.5. Construction of the T-PEN variables in the regular triangle node.

$$\bar{\phi}_V = \frac{1}{A}\int_S \phi(x,y)dS, \tag{4.26}$$

$$\tilde{\phi}_x = \frac{2}{\sqrt{3}hA}\int_S x\phi(x,y)dS, \tag{4.27}$$

$$\tilde{\phi}_y = \frac{2}{hA}\int_S y\phi(x,y)dS, \tag{4.28}$$

$$\bar{\phi}_x = \frac{1}{h}\int_{-\frac{1}{2}h}^{\frac{1}{2}h} \phi(x,y)|_{x=\frac{\sqrt{3}}{6}h} dy, \tag{4.29}$$

$$\bar{\boldsymbol{\phi}}_{\boldsymbol{u}} = \frac{1}{h}\int_{-\frac{\sqrt{3}}{3}h}^{\frac{\sqrt{3}}{6}h} \boldsymbol{\phi}(\boldsymbol{x},\boldsymbol{y})\big|_{\boldsymbol{y}=-\frac{1}{\sqrt{3}}\boldsymbol{x}-\frac{1}{3}\boldsymbol{h}}\,\boldsymbol{dx}, \tag{4.30}$$

$$\bar{\boldsymbol{\phi}}_{\boldsymbol{p}} = \frac{1}{h}\int_{-\frac{\sqrt{3}}{3}h}^{\frac{\sqrt{3}}{6}h} \boldsymbol{\phi}(\boldsymbol{x},\boldsymbol{y})\big|_{\boldsymbol{y}=-\frac{1}{\sqrt{3}}\boldsymbol{x}+\frac{1}{3}\boldsymbol{h}}\,\boldsymbol{dx}, \tag{4.31}$$

$$\boldsymbol{\phi}_{\boldsymbol{x}} = \boldsymbol{\phi}\left(-\frac{1}{\sqrt{3}}\boldsymbol{h},\boldsymbol{0}\right), \tag{4.32}$$

$$\boldsymbol{\phi}_{\boldsymbol{u}} = \boldsymbol{\phi}\left(\frac{\sqrt{3}}{6}\boldsymbol{h},\frac{1}{2}\boldsymbol{h}\right), \tag{4.33}$$

$$\boldsymbol{\phi}_{\boldsymbol{p}} = \boldsymbol{\phi}\left(\frac{\sqrt{3}}{6}\boldsymbol{h},-\frac{1}{2}\boldsymbol{h}\right), \tag{4.34}$$

$$\bar{\boldsymbol{D}}_{\boldsymbol{V}}^{\boldsymbol{2}} = -\frac{\boldsymbol{D}}{\boldsymbol{A}}\int_{\boldsymbol{S}}\left(\frac{\partial^2}{\partial \boldsymbol{x}^2}+\frac{\partial^2}{\partial \boldsymbol{y}^2}\right)\boldsymbol{\phi}(\boldsymbol{x},\boldsymbol{y})\boldsymbol{dS}, \tag{4.35}$$

$$\widetilde{\boldsymbol{D}}_{\boldsymbol{x}}^{\boldsymbol{2}} = -\frac{\boldsymbol{2D}}{\sqrt{\boldsymbol{3}}\boldsymbol{hA}}\int_{\boldsymbol{S}}\boldsymbol{x}\left(\frac{\partial^2}{\partial \boldsymbol{x}^2}+\frac{\partial^2}{\partial \boldsymbol{y}^2}\right)\boldsymbol{\phi}(\boldsymbol{x},\boldsymbol{y})\boldsymbol{dS}, \tag{4.36}$$

$$\widetilde{\boldsymbol{D}}_{\boldsymbol{y}}^{\boldsymbol{2}} = -\frac{\boldsymbol{2D}}{\boldsymbol{hA}}\int_{\boldsymbol{S}}\boldsymbol{y}\left(\frac{\partial^2}{\partial \boldsymbol{x}^2}+\frac{\partial^2}{\partial \boldsymbol{y}^2}\right)\boldsymbol{\phi}(\boldsymbol{x},\boldsymbol{y})\boldsymbol{dS}, \tag{4.37}$$

$$\bar{\boldsymbol{J}}_{\boldsymbol{x}} = -\frac{\boldsymbol{D}}{\boldsymbol{h}}\int_{-\frac{1}{2}h}^{\frac{1}{2}h}\left(\vec{\boldsymbol{e}}_{\boldsymbol{x}}\cdot\vec{\boldsymbol{\nabla}}\boldsymbol{\phi}(\boldsymbol{x},\boldsymbol{y})\right)\Big|_{\boldsymbol{x}=\frac{\sqrt{3}}{6}\boldsymbol{h}}\,\boldsymbol{dy}, \tag{4.38}$$

$$\bar{\boldsymbol{J}}_{\boldsymbol{u}} = -\frac{\boldsymbol{D}}{\boldsymbol{h}}\int_{-\frac{\sqrt{3}}{3}h}^{\frac{\sqrt{3}}{6}h}\left(\vec{\boldsymbol{e}}_{\boldsymbol{u}}\cdot\vec{\boldsymbol{\nabla}}\boldsymbol{\phi}(\boldsymbol{x},\boldsymbol{y})\right)\Big|_{\boldsymbol{y}=-\frac{1}{\sqrt{3}}\boldsymbol{x}-\frac{1}{3}\boldsymbol{h}}\,\boldsymbol{dx}, \tag{4.39}$$

$$\bar{\boldsymbol{J}}_{\boldsymbol{p}} = -\frac{\boldsymbol{D}}{\boldsymbol{h}}\int_{-\frac{\sqrt{3}}{3}h}^{\frac{\sqrt{3}}{6}h}\left(\vec{\boldsymbol{e}}_{\boldsymbol{p}}\cdot\vec{\boldsymbol{\nabla}}\boldsymbol{\phi}(\boldsymbol{x},\boldsymbol{y})\right)\Big|_{\boldsymbol{y}=-\frac{1}{\sqrt{3}}\boldsymbol{x}+\frac{1}{3}\boldsymbol{h}}\,\boldsymbol{dx}, \tag{4.40}$$

$$\boldsymbol{L}_{\boldsymbol{c}} = -\boldsymbol{D}\left(\vec{\boldsymbol{e}}_{\boldsymbol{x}}\cdot\vec{\boldsymbol{\nabla}}\boldsymbol{\phi}(\boldsymbol{x},\boldsymbol{y})\right)\Big|_{\left(-\frac{1}{\sqrt{3}}\boldsymbol{h},\boldsymbol{0}\right)}, \tag{4.41}$$

where h is the side length; A is the triangle area; D is the homogeneous diffusion coefficient in the triangle node. The notation of the energy group is omitted here.

The *derived* group variables can be expressed as a linear combination of the *representative* group variables by using the following procedures: First, express all T-PEN variables as a linear combination of the nine flux expansion coefficients by substituting Eq. (4.25) into Eqs. (4.26)–(4.41). Then, reverse the expressions of the *representative* group variables to express the nine flux expansion coefficients as a linear combination of the nine *representative* group variables. Finally, multiply the expressions of the *derived* group variables by the expressions of the flux expansion coefficients to express seven *derived* group variables as a linear combination of the nine *representative* group variables. The final expressions in a regular triangle are obtained as follows:

$$\bar{\boldsymbol{D}}^{\boldsymbol{2}} = \frac{\boldsymbol{D}}{\boldsymbol{h}^{\boldsymbol{2}}}\left(\boldsymbol{80}\bar{\boldsymbol{\phi}} - \boldsymbol{32}\left(\bar{\boldsymbol{\phi}}_{\boldsymbol{x}}+\bar{\boldsymbol{\phi}}_{\boldsymbol{u}}+\bar{\boldsymbol{\phi}}_{\boldsymbol{p}}\right)+\frac{\boldsymbol{16}}{\boldsymbol{3}}\left(\boldsymbol{\phi}_{\boldsymbol{x}}+\boldsymbol{\phi}_{\boldsymbol{u}}+\boldsymbol{\phi}_{\boldsymbol{p}}\right)\right), \tag{4.42}$$

$$\widetilde{D}_x^2 = \frac{D}{h^2}\left(80\widetilde{\phi}_x - \frac{16}{3}\bar{\phi}_x + \frac{8}{3}(\bar{\phi}_u + \bar{\phi}_p) + \frac{8}{9}(2\phi_x - \phi_u - \phi_p)\right), \quad (4.43)$$

$$\widetilde{D}_y^2 = \frac{D}{h^2}\left(80\widetilde{\phi}_y + 8(\bar{\phi}_u - \bar{\phi}_p) - \frac{8}{3}(\phi_u - \phi_p)\right), \quad (4.44)$$

$$\bar{J}_x = -\frac{D}{\sqrt{3}h}(20\bar{\phi} + 120\widetilde{\phi}_x - 24\bar{\phi}_x + 2\phi_x + \phi_u + \phi_p), \quad (4.45)$$

$$\bar{J}_u = -\frac{D}{\sqrt{3}h}(20\bar{\phi} - (60\widetilde{\phi}_x + 60\widetilde{\phi}_y) - 24\bar{\phi}_u + \phi_x + 2\phi_u + \phi_p), \quad (4.46)$$

$$\bar{J}_p = -\frac{D}{\sqrt{3}h}(20\bar{\phi} - (60\widetilde{\phi}_x - \widetilde{\phi}_y) - 24\bar{\phi}_p + \phi_x + \phi_u + 2\phi_p), \quad (4.47)$$

$$L_c = -\frac{\sqrt{3}D}{h}(60\widetilde{\phi}_x - 4\bar{\phi}_x + 4\phi_x). \quad (4.48)$$

For the hexagonal assembly including six triangle nodes shown in Figure 4.6, the T-PEN method employs 31 physical constrains for each energy group. These constraints include three diffusion equations in each triangle node including two weighted residual methods of x and y, two current continuity equations at each inner and outer surfaces, and one leakage balance equation at the center to construct the linear system as follows:

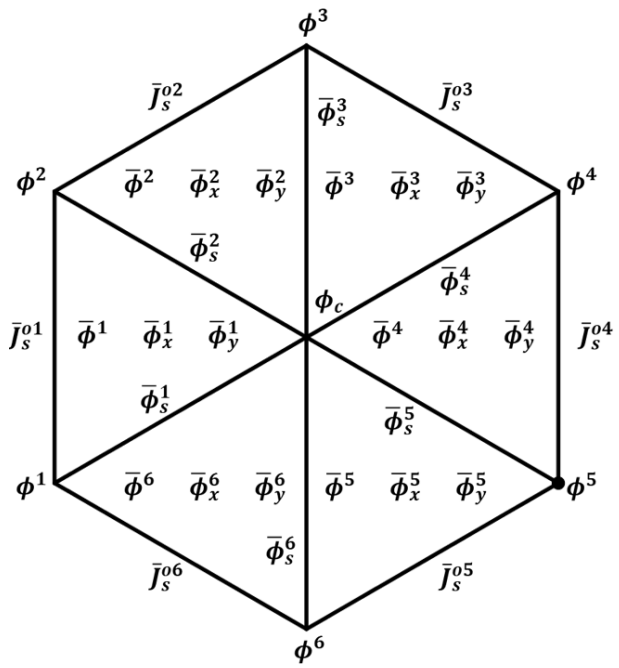

Figure 4.6. Construction of the T-PEN variables in the regular hexagonal assembly.

$$\bar{D}^{2i} + \Sigma_{rg}\bar{\phi}_g^i = \frac{\chi_g}{k_{eff}}\sum_{g'} \nu\Sigma_{fg'g}\bar{\phi}_{g'}^i + \sum_{g'} \Sigma_{sg'g}\bar{\phi}_{g'}^i + \bar{S}_g^{zi}, \quad (4.49)$$

$$\widetilde{D}_x^{2i} + \Sigma_{rg}\widetilde{\phi}_{gx}^i = \frac{\chi_g}{k_{eff}}\sum_{g'} \nu\Sigma_{fg'g}\widetilde{\phi}_{g'x}^i + \sum_{g'} \Sigma_{sg'g}\widetilde{\phi}_{g'x}^i + \tilde{S}_{gx}^{zi}, \quad (4.50)$$

$$\widetilde{D}_y^{2i} + \Sigma_{rg}\widetilde{\phi}_{gy}^i = \frac{\chi_g}{k_{eff}}\sum_{g'} \nu\Sigma_{fg'g}\widetilde{\phi}_{gy}^i + \sum_{g'} \Sigma_{sg'g}\widetilde{\phi}_{gy}^i + \tilde{S}_{gy}^{zi}, \quad (4.51)$$

$$\bar{J}_x^i = \bar{J}_x^{oi} - \bar{J}_x^{ii}, \tag{4.52}$$

$$\bar{J}_u^i = -\bar{J}_p^{i+1}, \tag{4.53}$$

$$\sum_{i=1}^{6} L_c^i = 0, \tag{4.54}$$

where Σ_r, Σ_f and Σ_s are the assembly macroscopic cross-sections of the removal, fission, and scattering reaction, respectively; χ is the fission spectrum; ν is the average number of neutrons generated by fission; k_{eff} is the multiplication factor; $\bar{S}^z, \tilde{S}_x^z$, and $\tilde{S}_y^z$ are the axial leakage source and two axial leakage source moments, respectively; and $\bar{J}_x^o$ and $\bar{J}_x^i$ are the outgoing and incoming partial currents, respectively.

The T-PEN response matrix can be constructed by substituting Eqs. (4.42)–(4.48) into Eqs. (4.49)–(4.54) as follows:

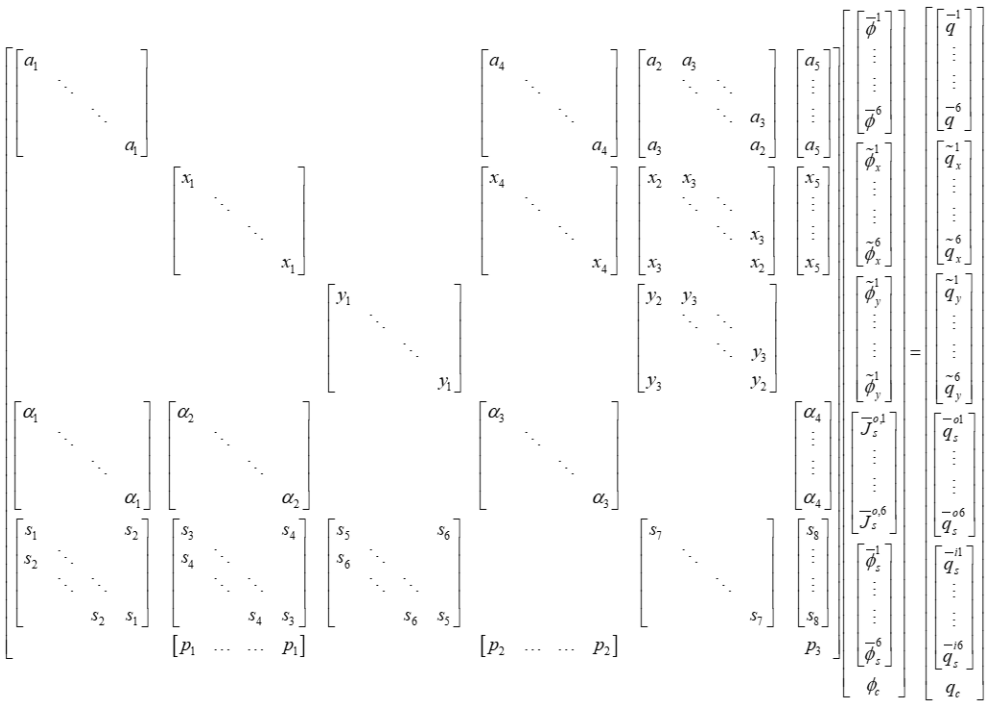

Figure 4.7. T-PEN Response matrix for a regular hexagonal assembly.

In this work, the definitions of the T-PEN variables described in Eqs. (4.26)–(4.41), except for the areal variables, are expanded to the unstructured triangle node shown in Figure 4.8 as follows:

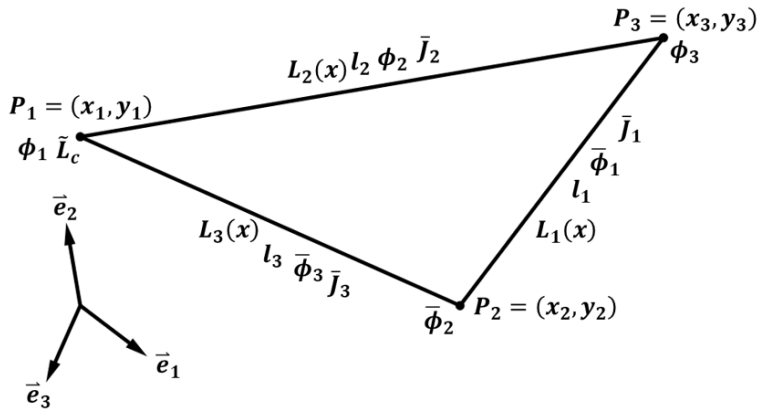

Figure 4.8. Construction of the T-PEN variables in the irregularly deformed triangle node.

$$\bar{\boldsymbol{\phi}}_{\mathbf{1}} = \frac{\mathbf{1}}{\boldsymbol{l}_{\mathbf{1}}} \int_{x_2}^{x_3} \boldsymbol{\phi}(\boldsymbol{x}, \boldsymbol{y})|_{L_1(x)}\, \boldsymbol{dx}, \tag{4.55}$$

$$\bar{\boldsymbol{\phi}}_{\mathbf{2}} = \frac{\mathbf{1}}{\boldsymbol{l}_{\mathbf{2}}} \int_{x_1}^{x_3} \boldsymbol{\phi}(\boldsymbol{x}, \boldsymbol{y})|_{L_3(x)}\, \boldsymbol{dx}, \tag{4.56}$$

$$\bar{\boldsymbol{\phi}}_{\mathbf{3}} = \frac{\mathbf{1}}{\boldsymbol{l}_{\mathbf{3}}} \int_{x_1}^{x_2} \boldsymbol{\phi}(\boldsymbol{x}, \boldsymbol{y})|_{L_3(x)}\, \boldsymbol{dx}, \tag{4.57}$$

$$\bar{\boldsymbol{J}}_{\mathbf{1}} = -\boldsymbol{D} \frac{\mathbf{1}}{\boldsymbol{l}_{\mathbf{1}}} \int_{x_2}^{x_3} \left(\vec{\boldsymbol{e}}_{\mathbf{1}} \cdot \vec{\boldsymbol{\nabla}} \boldsymbol{\phi}(\boldsymbol{x}, \boldsymbol{y}) \right) \Big|_{L_1(x)} \boldsymbol{dx}, \tag{4.58}$$

$$\bar{\boldsymbol{J}}_{\mathbf{2}} = -\boldsymbol{D} \frac{\mathbf{1}}{\boldsymbol{l}_{\mathbf{2}}} \int_{x_1}^{x_3} \left(\vec{\boldsymbol{e}}_{\mathbf{2}} \cdot \vec{\boldsymbol{\nabla}} \boldsymbol{\phi}(\boldsymbol{x}, \boldsymbol{y}) \right) \Big|_{L_2(x)} \boldsymbol{dx}, \tag{4.59}$$

$$\bar{\boldsymbol{J}}_{\mathbf{3}} = -\boldsymbol{D} \frac{\mathbf{1}}{\boldsymbol{l}_{\mathbf{3}}} \int_{x_1}^{x_2} \left(\vec{\boldsymbol{e}}_{\mathbf{3}} \cdot \vec{\boldsymbol{\nabla}} \boldsymbol{\phi}(\boldsymbol{x}, \boldsymbol{y}) \right) \Big|_{L_3(x)} \boldsymbol{dx}, \tag{4.60}$$

$$\boldsymbol{\phi}_{\mathbf{1}} = \boldsymbol{\phi}\left(\vec{\boldsymbol{P}}_{\mathbf{1}}\right), \tag{4.61}$$

$$\boldsymbol{\phi}_{\mathbf{2}} = \boldsymbol{\phi}\left(\vec{\boldsymbol{P}}_{\mathbf{2}}\right), \tag{4.62}$$

$$\boldsymbol{\phi}_{\mathbf{3}} = \boldsymbol{\phi}\left(\vec{\boldsymbol{P}}_{\mathbf{3}}\right), \tag{4.63}$$

$$\tilde{\boldsymbol{L}}_{\boldsymbol{c}} = -\frac{\boldsymbol{l}_{\mathbf{1}}}{\boldsymbol{h}} \left(\vec{\boldsymbol{e}}_{\mathbf{1}} \cdot \vec{\boldsymbol{\nabla}} \boldsymbol{\phi}(\boldsymbol{x}, \boldsymbol{y}) \right) \Big|_{\left(\vec{P}_1\right)}. \tag{4.64}$$

The linear combination expressions of the nine flux expansion coefficients for the corner fluxes and central leakage described in Eqs. (4.61)–(4.64) can be easily obtained by simple substitution. The expressions of the surface fluxes and currents in Eqs. (4.55)–(4.60) can be obtained by using the look-up table presented in Table 4.1. The expressions of the areal flux, flux moments, leakage, and leakage moments can be obtained by dividing the deformed assembly into parallelograms and calculating the surface integral functions for each parallelogram by using the look-up table presented in Table 4.2. Consequently, the *derived* group variables in the deformed triangle node can be expressed as linear combinations of the *representative* group variables by repeating the procedures described for the regular triangle node. The T-PEN response matrix for the deformed assembly can be constructed by

substituting the *derived* group variables with those expressions. Note that the curvilinear and surface integrals of nine polynomials are different for six triangle nodes of the deformed assembly as node shapes differ from each other. The diagonality of the response matrix can be decreased since all *representative* group variables are incorporated in the expressions of the *derived* group variables while the response matrix in regularly structured geometry is quite sparse. This decrease can deteriorate the performance of the T-PEN calculations for deformed hexagonal geometry problems.

In contrast with Eq. (4.41), the central leakage is multiplied by the length-weight in Eq. (4.64). This difference is because the leakage at one edge of an infinitesimal hexagon is a product of the leakage normal to the edge and the edge length as shown in Figure 4.9. The leakage balance at the center of the irregularly deformed hexagonal assembly is described as follows:

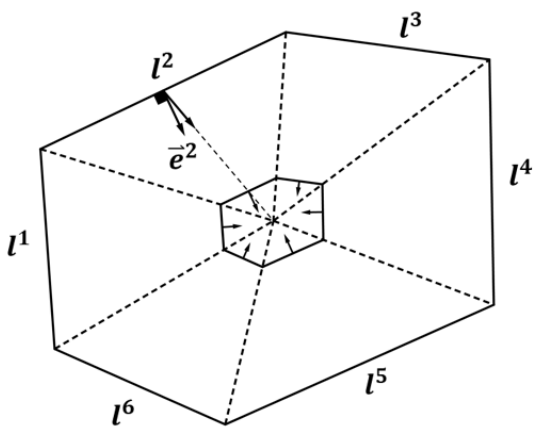

Figure 4.9. Leakage balance at the center of the irregularly deformed hexagonal assembly.

$$\sum_{i=1}^{6} \tilde{\boldsymbol{L}}_c^i = \mathbf{0}. \tag{4.65}$$

4.3. Expansion of the CPB solution to the Unstructured Geometry

The CPB solution is to approximate the flux distribution in a hexagonal assembly as a linear combination of fifteen polynomials as shown in Figure 4.10 as follows:

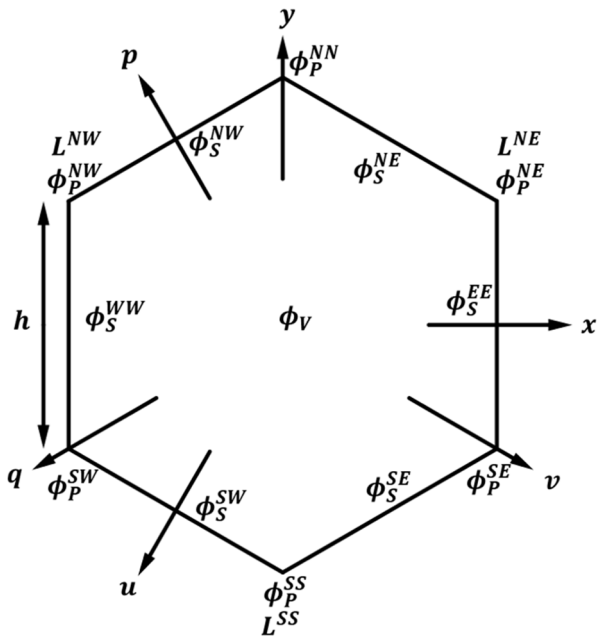

Figure 4.10. Construction of the CPB variables in the regular hexagonal assembly.

$$\begin{gathered}\boldsymbol{\phi(x,y) = C_0} \\ \boldsymbol{+A_x(x^3+x) + B_x(x^4+x^2) + A_y(y^3-y) + B_y(y^4-y^2)} \\ \boldsymbol{+A_u(u^3+u) + B_u(u^4+u^2) + A_v(v^3-v) + B_v(v^4-v^2)} \\ \boldsymbol{+A_p(p^3+p) + B_p(p^4+p^2) + A_q(q^3-q) + A_q(q^4-q^2),}\end{gathered} \tag{4.66}$$

where the notation of the energy group is omitted here.

The CPB variables represented in Figure 4.10 are defined similarly to the T-PEN method. The corner flux, surface flux, and areal flux belong to the *representative* group, and the corner leakage belongs to the *derived* group in the CPB solution. The expressions of three corner leakages as a linear combination of the fifteen flux expansion coefficients can be obtained as follows:

$$\begin{gathered}\boldsymbol{L^{SS} = -(3h^3-h)A_y + (4h^4-2h^2)B_y + \left(\frac{9\sqrt{3}}{8}h^3 + \frac{\sqrt{3}}{2}h\right)A_u +} \\ \boldsymbol{\left(\frac{9}{4}h^4 + \frac{3}{2}h^2\right)B_u + \left(\frac{3}{8}h^3 - \frac{1}{2}h\right)A_v + \left(\frac{1}{4}h^4 - \frac{1}{2}h^2\right)B_v -} \\ \boldsymbol{\left(\frac{9\sqrt{3}}{8}h^3 + \frac{\sqrt{3}}{2}h\right)A_p + \left(\frac{9}{4}h^4 + \frac{3}{2}h^2\right)B_p + \left(\frac{3}{8}h^3 - \frac{1}{2}h\right)A_q +} \\ \boldsymbol{\left(\frac{1}{4}h^4 - \frac{1}{2}h^2\right)B_q,}\end{gathered} \tag{4.67}$$

$$L^{NW} = -\left(\frac{9\sqrt{3}}{8}h^3 + \frac{\sqrt{3}}{2}h\right)A_x + \left(\frac{9}{4}h^4 + \frac{3}{2}h^2\right)B_x + \left(\frac{3}{8}h^3 - \frac{1}{2}h\right)A_y + \left(\frac{1}{4}h^4 - \frac{1}{2}h^2\right)B_y - (3h^3 - h)A_v + (4h^4 - 2h^2)B_v + \left(\frac{9\sqrt{3}}{8}h^3 + \frac{\sqrt{3}}{2}h\right)A_p + \left(\frac{9}{4}h^4 + \frac{3}{2}h^2\right)B_p + \left(\frac{3}{8}h^3 - \frac{1}{2}h\right)A_q + \left(\frac{1}{4}h^4 - \frac{1}{2}h^2\right)B_q, \quad (4.68)$$

$$L^{NE} = \left(\frac{9\sqrt{3}}{8}h^3 + \frac{\sqrt{3}}{2}h\right)A_x + \left(\frac{9}{4}h^4 + \frac{3}{2}h^2\right)B_x + \left(\frac{3}{8}h^3 - \frac{1}{2}h\right)A_y + \left(\frac{1}{4}h^4 - \frac{1}{2}h^2\right)B_y - \left(\frac{9\sqrt{3}}{8}h^3 + \frac{\sqrt{3}}{2}h\right)A_u + \left(\frac{9}{4}h^4 + \frac{3}{2}h^2\right)B_u + \left(\frac{3}{8}h^3 - \frac{1}{2}h\right)A_v + \left(\frac{1}{4}h^4 - \frac{1}{2}h^2\right)B_v - (3h^3 - 4h)A_q + (h^4 - 2h^2)B_q. \quad (4.69)$$

Three corner leakages can be expressed as linear combinations of the fifteen flux variables by repeating the converting procedures described in the previous subsection. Note that the coefficients in the expressions change with the assembly pitch while it does not in the T-PEN method. The corner leakages are substituted with these expressions in the leakage balance equation at the intersection of three assemblies shown in Figure 4.11. As a result, the intersection flux can be expressed as a linear combination of thirty flux variables as follows:

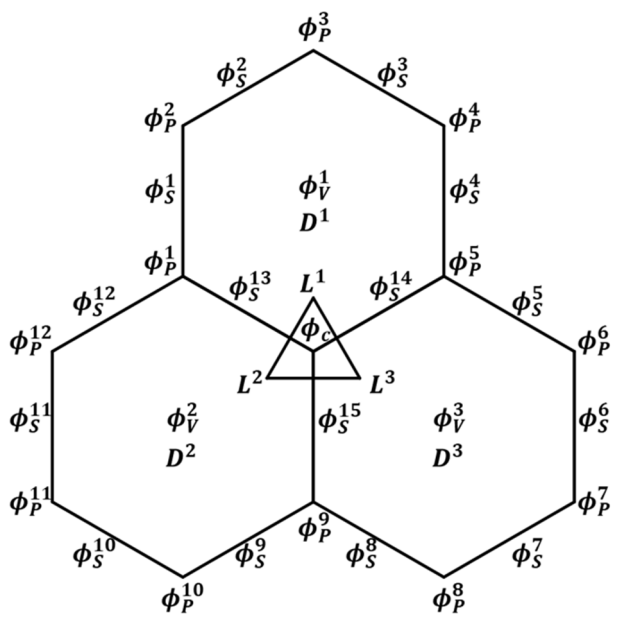

Figure 4.11. Construction of the CPB parameters in the regular hexagonal assemblies.

$$\sum_{i=3}^{3} L^i = 0, \quad (4.70)$$

$$(D^1 + D^2 + D^3)\phi_c + \omega_1\{D^1(\phi_P^1 + \phi_P^5) + D^2(\phi_P^1 + \phi_P^9) + \quad (4.71)$$

$$D^3\left(\phi_P^1+\phi_P^9\right)\}+\omega_2\{D^1\left(\phi_P^2+\phi_P^4\right)+D^2\left(\phi_P^6+\phi_P^8\right)+D^3\left(\phi_P^{10}+\phi_P^{12}\right)\}+\omega_3\left(D^1\phi_P^3+D^2\phi_P^7+D^3\phi_P^{11}\right)=\omega_4\{D^1\left(\phi_S^{13}+\phi_S^{14}\right)+D^2\left(\phi_S^{14}+\phi_S^{15}\right)+D^3\left(\phi_S^{13}+\phi_S^{15}\right)\}+\omega_5\{D^1\left(\phi_S^1+\phi_S^4\right)+D^2\left(\phi_S^5+\phi_S^8\right)+D^3\left(\phi_S^9+\phi_S^{12}\right)\}+\omega_6\{D^1\left(\phi_S^2+\phi_S^3\right)+D^2\left(\phi_S^6+\phi_S^7\right)+D^3\left(\phi_S^{10}+\phi_S^{11}\right)\}+\omega_7\left(D^1\phi_V^1+D^2\phi_V^2+D^3\phi_V^3\right),$$

where ω is the weighting factor changing with the assembly pitch. The weighting factors in the case of an assembly pitch of 4 (cm) are presented as follows:

$$\omega_1=\frac{72}{181}, \tag{4.72}$$

$$\omega_2=\frac{4}{181}, \tag{4.73}$$

$$\omega_3=-\frac{81}{905}, \tag{4.74}$$

$$\omega_4=\frac{7776}{9955}, \tag{4.75}$$

$$\omega_5=\frac{2928}{9955}, \tag{4.76}$$

$$\omega_6=-\frac{240}{1991}, \tag{4.77}$$

$$\omega_7=-\frac{144}{905}. \tag{4.78}$$

The linear system of the point fluxes in the core can be constructed by applying Eq. (4.71), where the surface fluxes and assembly fluxes determined from the T-PEN calculation are moved to the right-hand side, to all corner points. This linear system can be solved easily by using the plain Gauss-Seidal iteration scheme since it is strongly diagonally dominant.

In this work, the definitions of the CPB variables with the flux shape of Eq. (4.66) are expanded to the unstructured geometry similarly to the T-PEN method. The physical variables in the irregularly deformed hexagonal assembly shown in Figure 4.12 are expressed as linear combinations of the fifteen flux expansion coefficients by using Table 4.1 and Table 4.2. Three corner leakages in the leakage balance equation at the center are substituted with linear combinations of the fifteen flux variables by using the same converting procedures described in the previous subsection. The point fluxes in a deformed hexagonal geometry core are determined by solving the linear system employing the leakage balance equations at corner points including deviated ones. Note that the leakage balance equation at a deviated point employs the weighted sum of length between two neighboring corner points as shown in Figure 4.13.

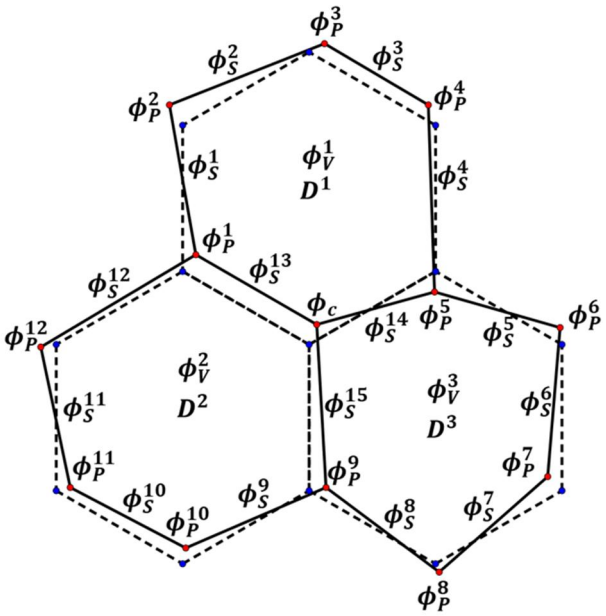

Figure 4.12. Construction of the CPB variables in the irregularly deformed hexagonal assemblies.

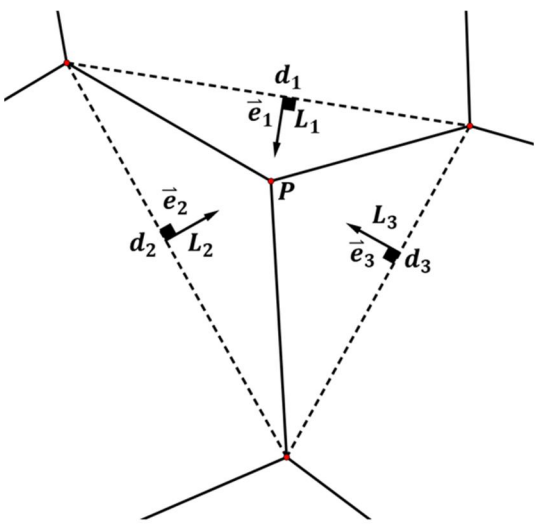

Figure 4.13. Leakage balance at the deviated point.

Chapter 5. Validation of the Solution Methods

The newly developed methods and schemes in nTRACER and RENUS described in the previous sections need to be verified to determine whether this research's purposes are achieved. The solution accuracy of nTRACER is verified first by comparing its calculation results for the various hexagonal geometry core problems against the McCARD results. In the subsequent subsection, the ADD performance is examined by comparing the ray tracing time *with* and *without* the ADD scheme for the various VVER core problems. The performance of the unstructured hexagonal nodal solution in RENUS is verified in the last subsection by comparing its calculation results for the arbitrarily deformed 2D SFR benchmark problems against the McCARD results.

The nTRACER calculation options proved to ensure sufficient solution accuracy by conducting sensitivity tests are used in this section. The ray parameters of 0.05 cm ray spacing, 12 azimuthal angles in [0, π], 4 polar angles in [0, π/2] are employed. The fuel of the fuel rod is divided into four regions in the radial direction. In contrast, the fuel with the gadolinium absorber is divided into seven regions. The outer iteration on ray tracing is terminated when the pseudo fission source error and residual error are reduced below 5x10-5.

In all nTRACER calculations in this section, pin power errors are examined in the absolute value, and the number of energy groups for VVER and SFR core problems are 47 and 33, respectively.

5.1. nTRACER Calculations for the Hexagonal Geometry Core Problems

For accuracy assessment, the nTRACER solutions for the hexagonal variant light water reactor (LWR) core problems, and 2D VVER and SFR core problems are compared with the McCARD [39] Monte Carlo reference solutions. The effect of P2 anisotropic scattering treatment on solution accuracy is also examined.

5.1.1. C5G7 H Benchmark Problem

The C5G7 H benchmark problems are the hexagonal variants of the C5G7 benchmark problems established for rectangular geometry LWR cores without spatial homogenization.[1] The core consist of nine materials including one UOX,

three MOX fuels, one fission chamber, one guide tube, one moderator, and one control rod. The seven-group macroscopic cross-section set for these materials is provided in this benchmark. The fuel loading pattern in the radial direction and axial configuration with three types of control rod insertion are illustrated in Figure 5.1. Fuel assemblies of a pitch of 11.9 cm shown in Figure 5.2 consist of fuel pins of a radius of 0.54 cm. One 2D core problem, where all control rods are withdrawn, and three 3D core problems with different control rod insertions in UA assemblies indicated in Table 5.1 are included in this benchmark.

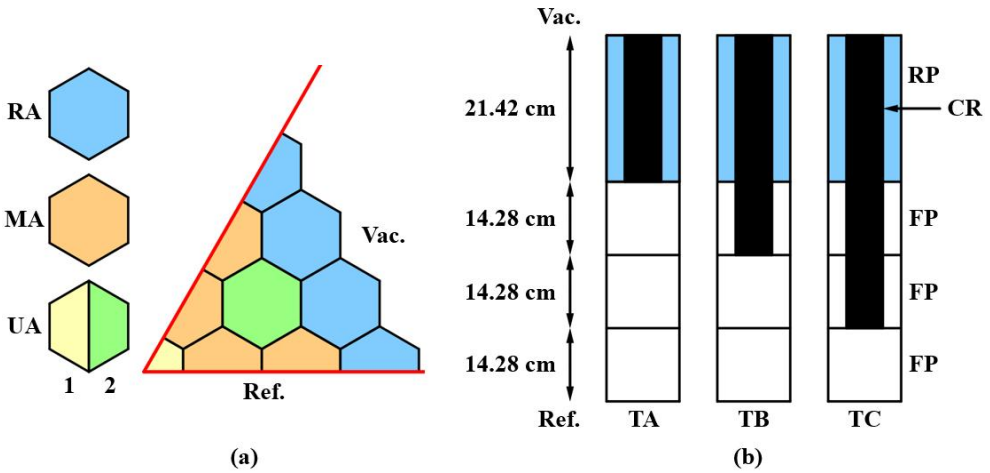

Figure 5.1. (a) Radial and (b) axial core configurations in the C5G7 H benchmark problem.

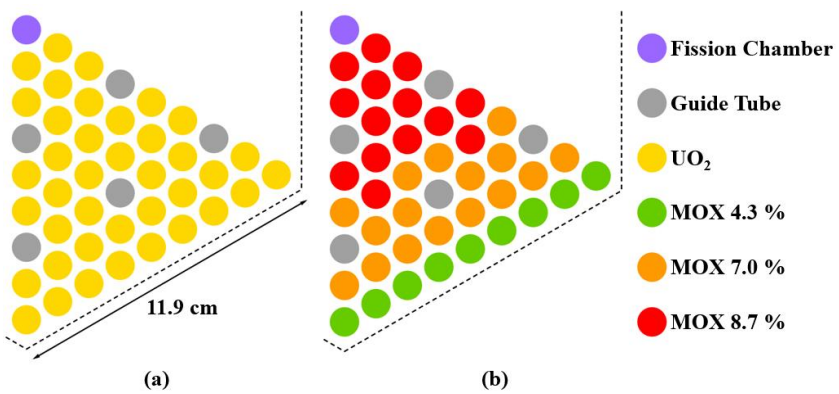

Figure 5.2. (a) UA and (b) MA in the C5G7 H benchmark problem.

Table 5.1. Control rod insertion in the C5G7 H benchmark problems.

Problems	UA-1	UA-2	MA
Unrodded	TA	TA	TA
Rodded A	TB	TA	TA
Rodded B	TC	TB	TA

The McCARD solution for these benchmark problems was determined as an average of three calculation results for the same problem with different random number seeds. Each McCARD calculation was conducted by using 100 inactive cycles, 500 active cycles, and 20 million particles per cycle. The standard deviation of pin power distribution does not exceed 0.19 %.

The solution accuracy of nTRACER for the 2D C5G7 H problem is sufficiently high in that the reactivity difference is 12 pcm and the maximum and root-mean-square (RMS) pin power differences are 1.02 % and 0.24 %, respectively, as presented in Table 5.2 and Figure 5.3.

Table 5.2. Comparison of two solutions for the 2D C5G7 H core problem.

McCARD		nTRACER		
k-eff	σ (pcm)	Δρ (pcm)	Max. ΔP (%)	RMS ΔP (%)
1.16241	2	12	1.02	0.24

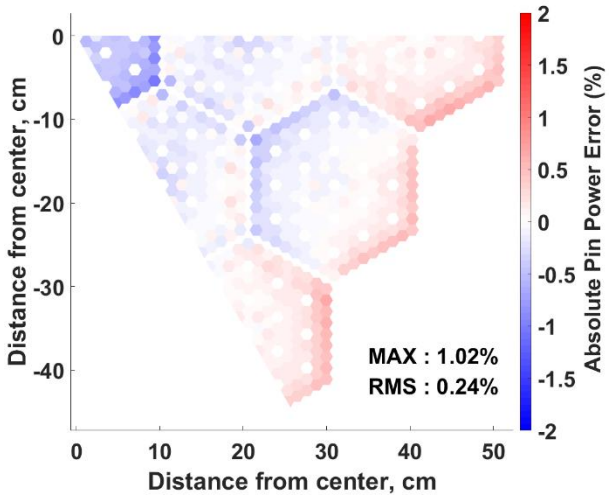

Figure 5.3. Pin power difference distribution for the 2D C5G7 H core problem.

The solution differences for the three 3D C5G7 H problems are summarized in Table 5.3, and the pin power difference for the Rodded A case in the radial and axial

directions are depicted in Figure 5.4 and Figure 5.5, respectively. The maximum difference in reactivity and 3D pin power distribution are 7 pcm and 6.41 %, respectively. The 3D pin power difference is somewhat high. However, the radial and axial pin power differences do not exceed a tolerance range. Thus, it is concluded that nTRACER reproduces the reference solutions for all C5G7 H benchmark problems with high accuracy.

Table 5.3. Comparison of two solutions for the 3D C5G7 H core problems.

			Unrodded	Rodded A	Rodded B
McCARD	k-eff		1.12273	1.11891	1.10264
	σ (pcm)			1	
nTRACER	Δρ (pcm)		**7**	3	-2
	3D ΔP (%)	Max.	**6.41**	5.98	5.36
		RMS	0.43	**0.44**	0.44
	Rad. ΔP (%)	Max.	0.93	**0.98**	0.89
		RMS	0.24	**0.26**	0.24
	Ax. ΔP (%)	Max.	**0.86**	0.76	0.84
		RMS	**0.23**	0.17	0.23

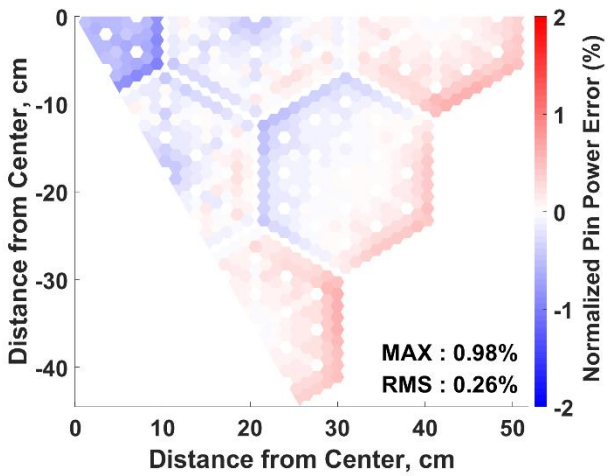

Figure 5.4. Radial pin power difference distribution for the C5G7 H Rodded A problem.

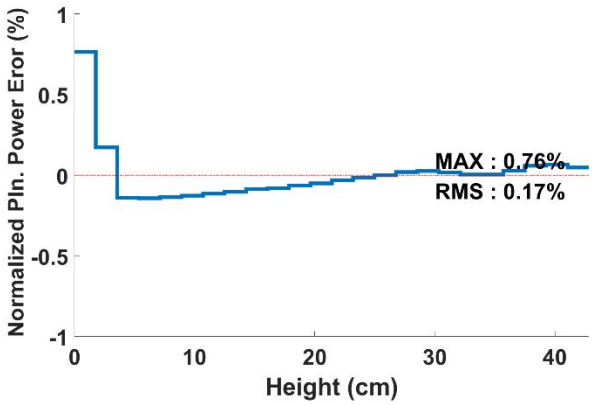

Figure 5.5. Axial plane power difference distribution for the C5G7 H Rodded A problem.

5.1.2. KAERI Benchmark Problem (VVER-1000)

The core configuration of the KAERI benchmark problem is illustrated in Subsection 2.1. All cases of the 2D KAERI benchmark problem described in Table 5.4 are solved by nTRACER and McCARD. The same McCARD options in the previous verification are also used for this problem.

Table 5.4. Benchmark cases of the 2D KAERI benchmark problem.

Case	Temperature (K)		Boron concentration (ppm)
	Fuel	Cladding, Coolant	
V01	300	300	0
V02	600	600	0
V03	900	600	0
V04	300	300	1,000
V05	600	600	1,000
V06	900	600	1,000
V07	300	300	2,000
V08	600	600	2,000
V09	900	600	2,000

nTRACER solved the 2D KAERI core problem by using the P0 option. The solution differences calculated by comparing the nTRACER calculation results against the McCARD results are presented in Table 5.5. The solution differences are somewhat high for the V01, V04, and V07 cases, where all materials are at 300 K. This is because the SNURPL 47G library used in the nTRACER calculations were generated targeting operation states with high temperature. On the other hand, the high solution accuracy of nTRACER is demonstrated for other cases as shown in

Figure 5.6 while it does not change significantly by fuel temperature nor boron concentration.

Table 5.5. Comparison of the two solutions for the 2D KAERI core problem with the P0 option.

P0	McCARD		nTRACER		
	k-eff	σ (pcm)	Δρ (pcm)	Max. ΔP (%)	RMS ΔP (%)
V01	1.28365		-34	**2.24**	**0.95**
V02	1.22097		-8	0.72	0.19
V03	1.21116		-38	0.68	0.20
V04	1.08154		-72	1.52	0.61
V05	1.08246	1	-23	0.58	0.22
V06	1.07377		-55	0.62	0.22
V07	0.94263		**-106**	1.54	0.53
V08	0.97712		-32	0.63	0.23
V09	0.96935		-68	0.70	0.27

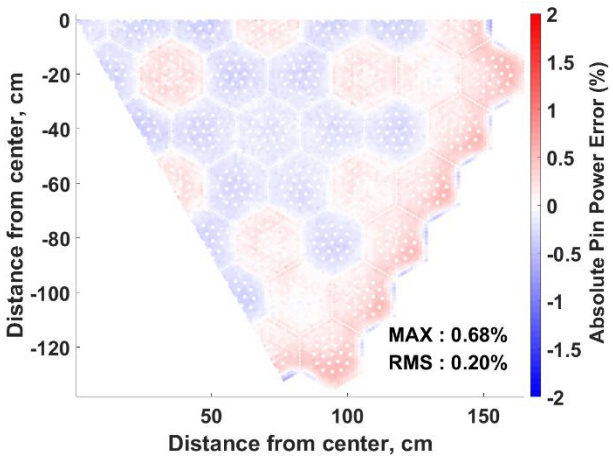

Figure 5.6. Radial pin power difference distribution for the KAERI V03 problem with the P0 option.

The effect of P2 anisotropic scattering treatment on solution accuracy is examined by comparing the solution differences between the P0 and P2 options. Table 5.6 and Figure 5.7 represent the solution difference with the P2 option. The reduction in solution difference is presented with a positive sign in Table 5.7. The reactivity difference is significantly reduced in most cases by using the P2 option. On the other hand, the pin power difference is increased for all cases at room temperature. It is also increased as boron concentration increases. It is demonstrated that the SNURPL 47G library needs to employ improved P2 anisotropic scattering treatment for problems at room temperature with high boron concentration.

Nonetheless, the increase in solution accuracy of nTRACER by using the P2 option for the core problems in operation state with low boron concentration is verified in this benchmark.

Table 5.6. Comparison of the two solutions for the 2D KAERI core problem with the P2 option.

P2	McCARD		nTRACER		
	k-eff	σ (pcm)	Δρ (pcm)	Max. ΔP (%)	RMS ΔP (%)
V01	1.28365		5	**2.33**	**0.89**
V02	1.22097		22	0.47	0.14
V03	1.21116		-7	0.50	0.18
V04	1.08154		23	1.85	0.80
V05	1.08246	1	31	0.58	0.20
V06	1.07377		-1	0.54	0.10
V07	0.94263		36	1.82	0.67
V08	0.97712		**46**	0.82	0.35
V09	0.96935		11	0.99	0.41

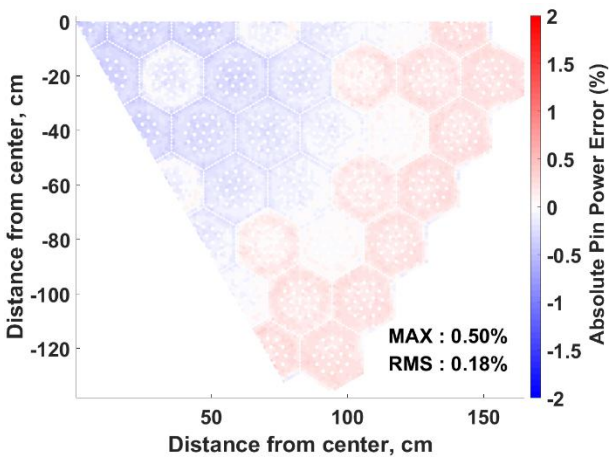

Figure 5.7. Radial pin power difference distribution for the KAERI V03 problem with the P2 option.

Table 5.7. Reduction in solution differences for the 2D KAERI core problem by using the P2 option.

P0-P2	Abs. Δρ (pcm)	Max. ΔP (%)	RMS ΔP (%)
V01	29	-0.09	0.06
V02	-14	0.25	0.05
V03	31	0.18	0.02
V04	49	-0.33	-0.19
V05	-8	0	0.02
V06	54	0.08	0.12
V07	70	-0.28	-0.14
V08	-14	-0.19	-0.12
V09	57	-0.29	-0.14

5.1.3. VVER440 'Full-core' Benchmark Problem

nTRACER solved the VVER440FC benchmark problem by using both P0 and P2 options. The same McCARD options in the previous verification are also used for this problem. The solution differences are presented in Table 5.8, Figure 5.8, and Figure 5.9. The solution accuracy of nTRACER is increased significantly by using the P2 option. These verification results correspond to the previous subsection since the benchmark problem is in operation state with low boron concentration. It is concluded that nTRACER reproduces the reference solutions for VVER core problems with high accuracy, which is improved by using the P2 option for problems in operation state with low boron concentration.

Table 5.8. Comparison of the two solutions for the VVER440FC core problem.

	McCARD		nTRACER		
	k-eff	σ (pcm)	Δρ (pcm)	Max. ΔP (%)	RMS ΔP (%)
P0	1.08834	1	-116	1.42	0.81
P2			-52	0.52	0.32

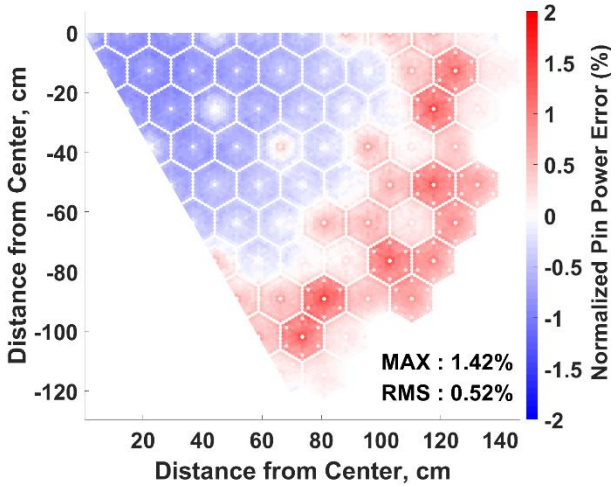

Figure 5.8. Radial pin power difference distribution for the VVER440FC problem with the P0 option.

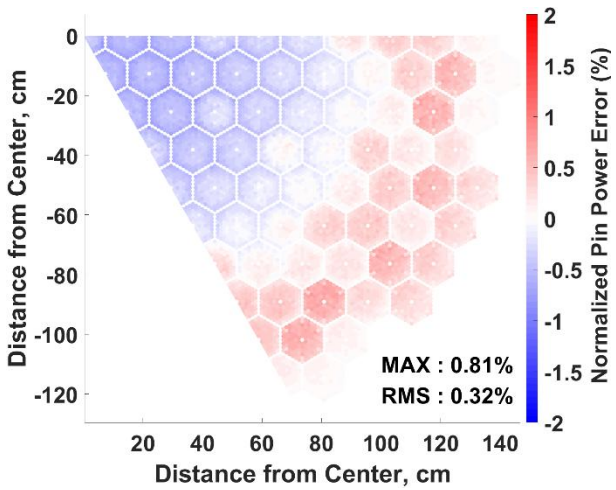

Figure 5.9. Radial pin power difference distribution for the VVER440FC problem with the P2 option.

5.1.4. MET-1000 Benchmark Problem

nTRACER solved the 2D MET-1000 benchmark problem by using the P2 option. The McCARD calculation result for this problem was obtained by using 500 inactive cycles, 2,000 active cycles, and 200 thousand particles per cycle. The solution difference is presented in Table 5.9 and Figure 5.10. The reactivity difference and the maximum and RMS pin power differences are 150 pcm, 2.17 %, and 0.76, respectively, which are in a tolerance range.[40] Thus, it is concluded that nTRACER attained satisfactory accuracy for solving SFR core problems.

Table 5.9. Comparison of the two solutions for the 2D MET-1000 core problem.

McCARD		nTRACER		
k-eff	σ (pcm)	Δρ (pcm)	Max. ΔP (%)	RMS ΔP (%)
1.22141	2	150	2.17	0.76

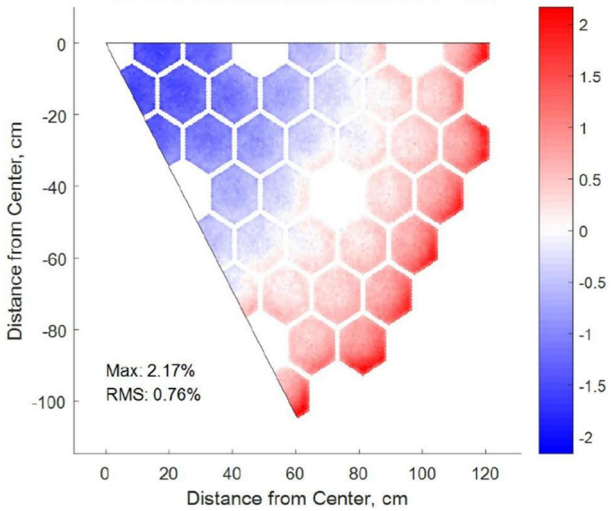

Figure 5.10. Radial pin power difference distribution for the 2D MET-1000 problem.

5.2. Performance Examination of the nTRACER Hexagonal Ray Tracing Calculation with the ADD scheme

The parallel execution performance of the new hexagonal version of nTRACER is examined by comparing the two solutions obtained *with* and *without* the ADD scheme. Considering practical operating conditions, only V03, V06, and V09 in the KAERI benchmark problem are solved. In these cases, the fuel and coolant temperatures are 900 K and 600 K, respectively, and the boron concentration ranges from 0 ppm to 2,000 ppm. The calculation options including the ray parameters and mesh structures in the previous section are also used in this section. For the 3D core problems, the active fuel region is equally divided into eighteen planes in the KAERI problem and into twelve planes in the VVER440FC problem, respectively. The axial reflectors in the 3D VVER440FC problem are also divided in half. As a consequence, eight computing nodes are exploited to solve sixteen and twenty-four planes of the VVER440FC and KAERI problems, respectively. The nTRACER calculations were performed on a ten-nodes computing platform, of which each node is equipped with two 26-core CPUs of Intel Xeon Gold 6230 R with 2.10 GHz clocks and 540 GB

RAM. The nodes are connected by 100 Gbps InfiniBand, which transfers calculation results between each node.

5.2.1. 2D VVER Core Problems

In the ADD scheme, the incoming angular flux at the assembly surface is updated by using the partial current information determined by the CMFD calculation by following Eq. (3.1). If the surface of a CMFD mesh adjoins more than two CMFD meshes, the length-weighted sum of CMFD fluxes should be employed in the partial incoming current update. This approximation might deteriorate neutron balance in CMFD meshes, consequently, and calculation convergence. In this regard, the nTRACER modeling of Vygorodka in the VVER440FC benchmark problem is modified from one shown in Figure 2.10.b to the other shown in Figure 5.11.a such that CMFD mesh boundaries are aligned, but Vygorodka is modeled with a jagged edge. Here the dimensions of the fuel and moderator cells are the same unlike in Figure 2.10.b. The cells representing Vygorodka are filled with a homogeneous mixture of steel and moderator materials, which conserves the total mass of Vygorodka. The error associated with this approximation of Vygorodka was assessed by the nTRACER runs with the angle-wise parallel computing option. The difference in power distribution between the two models is given in Figure 5.11.b., which reveals the maximum error of about 1 % at the core periphery. The reactivity error and RMS pin power difference are negligible. Thus, it is expected that the approximated Vygorodka modeling to enable the ADD would have a negligible impact on solution accuracy.

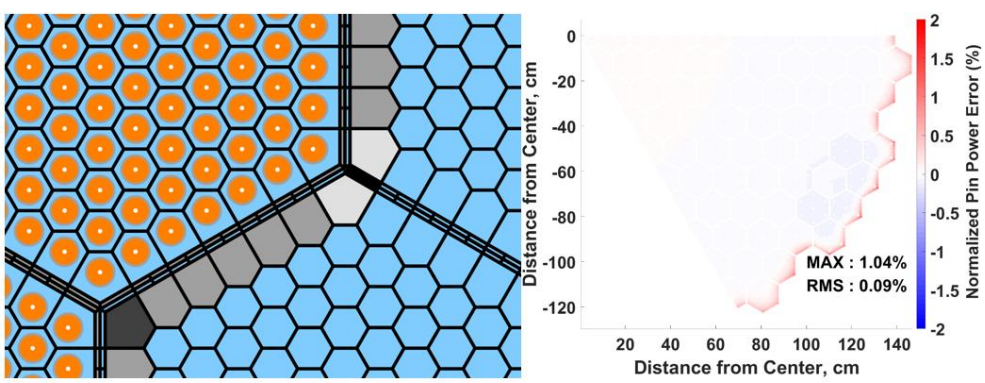

Figure 5.11. (a) nTRACER modeling for Vygorodka with the ADD scheme (b) Pin power difference for the 2D VVER440FC core problem.

For the 2D KAERI V09 core calculations *with* and *without* the ADD scheme,

the OpenMP parallel speedup in the ray tracing calculation is examined as shown in Figure 5.12. As the number of threads increases, the actual parallel speedup falls behind the ideal one. This gap is induced by load imbalance and thread communication. The ray tracing calculation for the full core with the ADD scheme has good load balancing since all assemblies have tracking rays of the same size. Thus, this case has a high parallel speedup of about 21 using twenty-six threads. The parallel speedups in other cases are less than 16 since imbalance exists in the assembly area or tracking ray length. Twenty-six threads of each processor are used for the planar MOC calculations in the following.

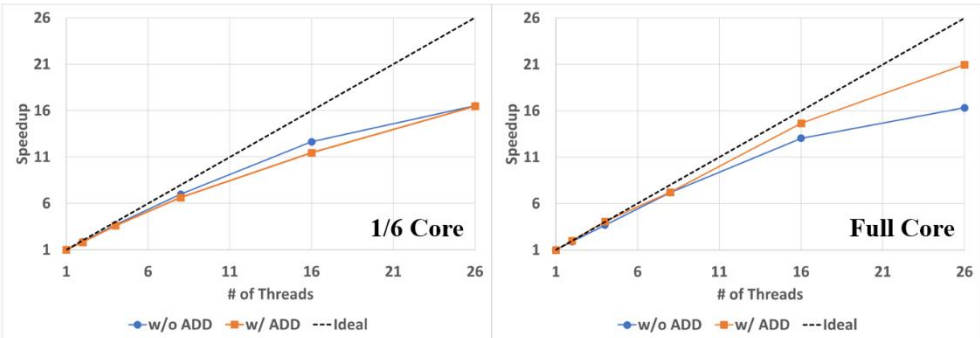

Figure 5.12. OpenMP parallel speedup of the ray tracing calculation for the 2D KAERI V09 core problems.

For each of the 2D core problems, the two solutions *with* and *without* the ADD scheme were compared as summarized in Table 5.10. The solution differences must be small because both solutions were obtained after satisfying the same convergence criterion. The convergence behaviors shown in Figure 5.13 indicate that convergence is slower with the ADD scheme. This drawback is because the incoming angular fluxes had to be approximated even with the CMFD partial current update scheme of Eq. (3.1). Nonetheless, the number of ray tracing iterations needed for satisfying the convergence criterion increases only by one for the one-sixth symmetry cases while it does not essentially increase for the full core cases. The comparison results for calculation performance are presented in Table 5.11 including the computing times, where '# of RT' and 'Total RT' are the number of ray tracing iterations and total ray tracing time, respectively.

Table 5.10. Calculation error with the ADD scheme for the 2D VVER core problems.

Problem		Δρ (pcm)	ΔP (%)	
			Max.	RMS
1/6 Core	KAERI V03	0	**0.34**	0.10
	KAERI V06	0	0.32	0.10
	KAERI V09	0	0.25	0.08
	VVER440FC	0	0.32	**0.11**
Full Core	KAERI V03	0	**0.31**	**0.11**
	KAERI V06	0	0.30	0.10
	KAERI V09	-1	0.17	0.07
	X2	0	0.31	0.10
	VVER440FC	0	0.05	0.01

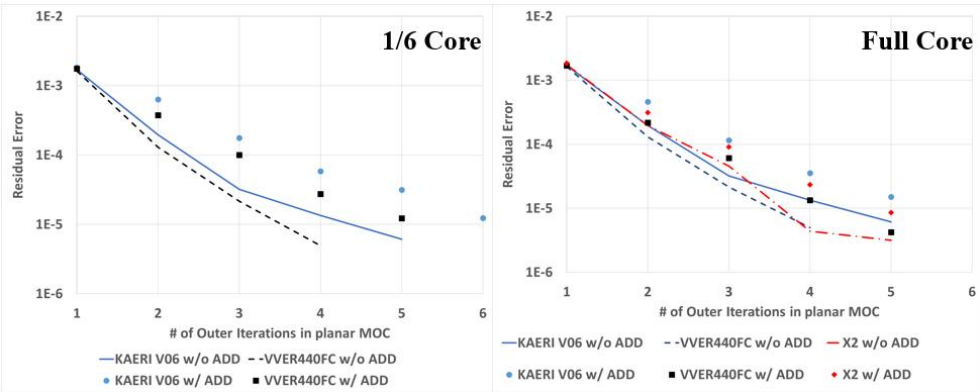

Figure 5.13. Residual error reduction for the 2D VVER core problems.

Table 5.11. Calculation performance with the ADD scheme assessed for the 2D VVER core problems.

Problems		w/o ADD		w/ ADD	
		# of RT	Total RT	# of RT	Total RT
1/6 Core	KAERI V03	5	22m	6	19m
	KAERI V06	5	22m	6	20m
	KAERI V09	5	22m	6	20m
	VVER440FC	4	12m	5	10m
Full Core	KAERI V03	5	2h 7m	5	1h 8m
	KAERI V06	5	2h 8m	5	1h 7m
	KAERI V09	5	2h 9m	5	1h 7m
	X2	5	1h 59m	5	1h 8m
	VVER440FC	4	67m	5	43m

Computing time decreases significantly for the 2D full core problems as summarized in Table 5.12. The total computing time is reduced by 26~38%, and

higher reductions of 43~49% are possible for each ray tracing calculation. This significant reduction is possible because memory access traffic is significantly reduced by reducing the memory size needed for each thread. In the original angle-wise parallelization without the ADD scheme, all threads have to access the geometry information of the entire core. Thus, there could be a serious fetching overhead due to a memory access bottleneck, which deteriorates calculation performance. This fetching overhead is significantly reduced by using the ADD scheme, which requires fetching local geometry information by each thread. For the 2D KAERI full core problem, the memory needed for the angle-wise parallelization (without the ADD scheme) and the ADD scheme turned out to be 100 GB and 82 GB, respectively. 18 GB reduction in memory was possible by using the ADD scheme even though additional memory was required to store the incoming angular fluxes at each assembly surface. For the one-sixth core problem, the single ray tracing time reduction is deteriorated due to an imbalance in sweeping assemblies and an increase in ray tracing iterations.

Table 5.12. Computing time reduction (%) with the ADD scheme for the 2D VVER core problems.

Problems		Single RT	Total RT	Total
1/6 Core	KAERI V03	29	15	3
	KAERI V06	25	10	0
	KAERI V09	26	11	1
	VVER440FC	**34**	**18**	**6**
Full Core	KAERI V03	47	47	35
	KAERI V06	48	**48**	36
	KAERI V09	48	48	**38**
	X2	43	43	33
	VVER440FC	**49**	36	26

5.2.2. 3D VVER Core Problems

The 3D core calculation is decomposed first axially by assigning a certain number of planes to each computing node. Eight computing nodes in the ten-nodes computing platform were exploited in the calculations for the 3D VVER440FC and KAERI core problems with sixteen and twenty-four planes, respectively. For the 3D VVER440FC core calculations *with* and *without* the ADD scheme, the MPI parallel speedup in the ray tracing calculation is examined as shown in Figure 5.14. The memory size required for the 3D VVER440FC full core calculation exceeds memory limitation when less than four computing nodes are exploited. nTRACER has good MPI parallel performance, which is better in the calculations with the ADD scheme.

In the following, two processors of each computing node are used for the 3D VVER440FC core problems while only one is used for the 3D KAERI core problems due to a memory size restriction. Thus, each processor solves one planar MOC problem of the 3D VVER440FC core while it solves four planar MOC problems of the 3D KAERI cores.

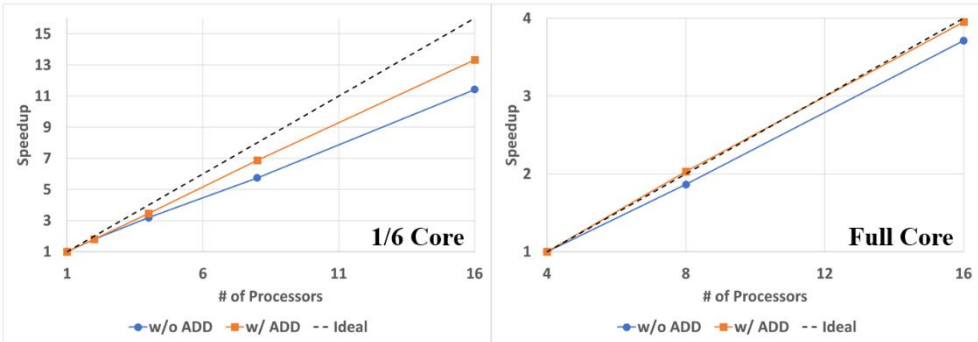

Figure 5.14. MPI parallel speedup of the ray tracing calculation for the 3D KAERI V09 core problems.

The solution accuracy summarized in Table 5.13-Table 5.14 and the convergence behavior shown in Figure 5.15 reveal the same tendency as the 2D problems.

Table 5.13. Calculation error with the ADD scheme for the 3D VVER one-sixth core problems.

Problem	Δρ (pcm)	ΔP (%) 3D		2D		1D	
		Max.	RMS	Max.	RMS	Max.	RMS
KAERI V03	0	0.60	0.18	0.26	0.09	**0.26**	**0.14**
KAERI V06	0	**0.78**	**0.23**	**0.54**	**0.21**	0.07	0.04
KAERI V09	-1	0.25	0.05	0.12	0.04	0.06	0.03
VVER440FC	-1	0.35	0.09	0.21	0.08	0.05	0.03

Table 5.14. Calculation error with the ADD scheme for the 3D VVER full core problems.

Problem	Δρ (pcm)	ΔP (%) 3D		2D		1D	
		Max.	RMS	Max.	RMS	Max.	RMS
KAERI V03	0	**0.47**	**0.16**	**0.14**	**0.06**	**0.25**	**0.14**
KAERI V06	0	0.14	0.05	0.07	0.03	0.06	0.03
KAERI V09	0	0.17	0.05	0.07	0.03	0.06	0.04
VVER440FC	-1	0.30	0.06	0.12	0.03	0.07	0.05

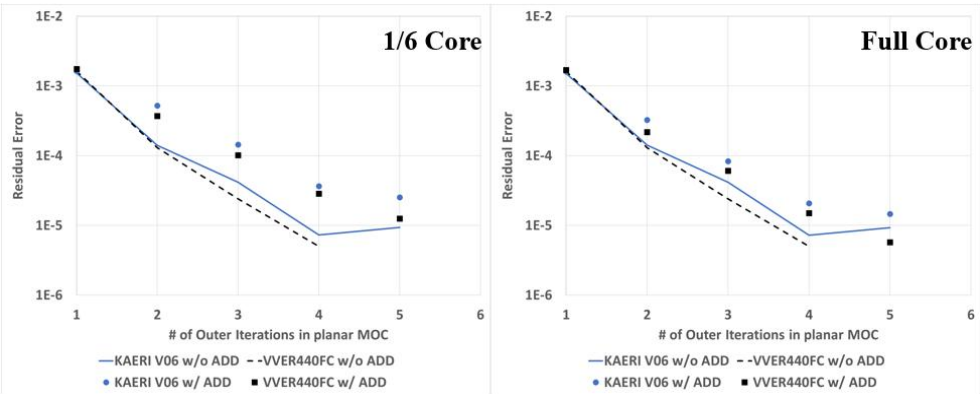

Figure 5.15. Residual error reduction for the 3D VVER core problems.

The calculation performance and reduction in computing time with the ADD scheme assessed for the 3D core problems are summarized in Table 5.15-Table 5.17, where the computing time for the axial MOC calculation is included under 'Total Ax.' Compared to the 2D full core problems, the reduction in radial ray tracing time is better in that the 27~53% reduction is possible in the single ray tracing time. This improvement is because the fetching overhead in the angle-wise parallelization is further increased by allocating four planes to each computing node in the 3D core problems. For the same reason, the 4~45% reduction in total computing time is possible for the 3D core problems. The axial MOC solver in nTRACER incorporates the effect of anisotropic scattering in the axial reflectors filled with the pure moderator to stabilize 3D core calculations. Some instability was noted in the axial MOC solution for the VVER440FC problem with the ADD scheme. This instability leads to performing more axial MOC calculations and increasing the axial MOC calculation time. This drawback offsets the gain for the computing time reduction in the radial MOC calculation, which is the main target of the ADD scheme. Nonetheless, the total computing time is reduced by up to 45%, which demonstrates the advantage of the ADD scheme in the computing time reduction.

Note that the capability of solving a 3D VVER full core is a crucial feature of a DWCC code because it is necessary for solving the asymmetric core, e.g., the X2 benchmark problem or for analyzing the depletion in the core with an asymmetric burn-up distribution. The ADD scheme can be exploited to reduce computing time for those 3D VVER full core calculations.

Table 5.15. Calculation performance assessed for the 3D VVER one-sixth core problems.

Problems	w/o ADD			w/ ADD		
	# of RT	Total RT	Total Ax	# of RT	Total RT	Total Ax.
KAERI V03	4	1h 36m	5m	5	1h 10m	5m
KAERI V06	5	2h 9m	5m	5	1h 12m	5m
KAERI V09	5	2h	5m	6	1h 20m	5m
VVER440FC	4	15m	17m	5	13m	17m

Table 5.16. Calculation performance assessed for the 3D VVER full core problems

Problems	w/o ADD			w/ ADD		
	# of RT	Total RT	Total Ax	# of RT	Total RT	Total Ax.
KAERI V03	4	10h 39m	39m	5	6h 18m	40m
KAERI V06	5	13h 19m	40m	5	6h 20m	40m
KAERI V09	5	13h 31m	40m	5	6h 19m	40m
VVER440FC	4	1h 32m	1h 47m	5	1h 8m	1h 55m

Table 5.17. Computing time reduction (%) with the ADD scheme for the 3D VVER core problems.

Problems		Single RT	Total RT	Total
1/6 Core	KAERI V03	41	27	19
	KAERI V06	**44**	**44**	**36**
	KAERI V09	44	33	26
	VVER440FC	32	15	4
Full Core	KAERI V03	**53**	41	31
	KAERI V06	52	52	44
	KAERI V09	53	**53**	**45**
	VVER440FC	41	27	5

5.3. RENUS Calculations for the Arbitrarily Deformed Core Problems

Considering the physical backgrounds of an SFR core deformation, it is necessary to employ *contrived states* to verify the unstructured nodal solution in RENUS. The definition of the *contrived state* is suggested first. In the subsequent subsection, the benchmark for a sodium-cooled fast breeder reactor is introduced, and the RENUS solutions are verified for the benchmark core problems with regularly structured geometry against the reference solution provided by McCARD. The RENUS verification results for the arbitrarily deformed 2D core problems with uniform and assembly-wise expansion are then followed.

5.3.1. Definition of the *Contrived State*

The physical backgrounds of an SFR core deformation can be grasped from the limited free bow illustrated in Figure 5.16.[41] As the thermal gradient develops during reactor operation, the assembly ducts begin to bow outward. After the outermost top load pad touches the restraint ring, the assembly ducts begin to bow inward. Note that the assembly inner components retain shape while the assembly duct moves laterally. This core deformation is a problem with millions of degrees of freedom due to thousands of mechanical interactions between the assembly ducts, supporting structure, restraint system, etc., induced by neutron irradiation, thermal expansion, and sodium coolant pressure. Dealing with the entire quality of the information provided to SFR core deformations must exceed the scope of this research.

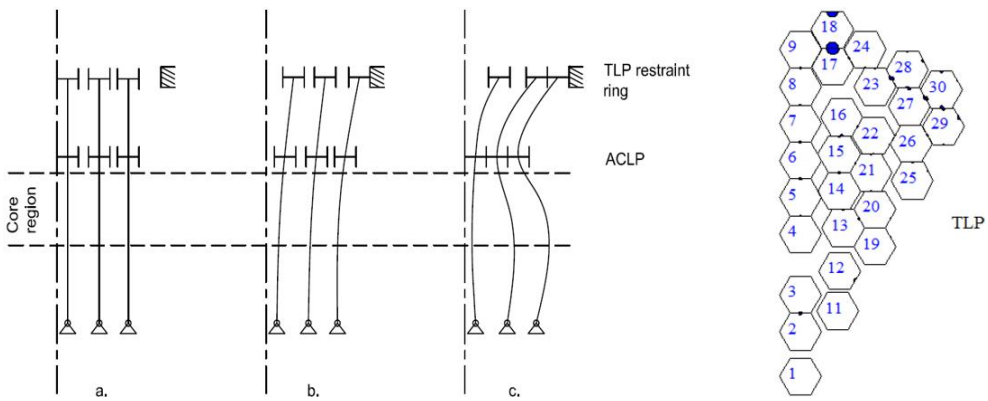

Figure 5.16. Axial and radial configurations of the limited free bow in an SFR core.

The *contrived state*, a hypothetical deformation state not claimed to be true deformation state in the reactor, is introduced to expose the weaknesses and strengths of calculation methods under different conditions.[42] Considering the lateral displacements of assemblies shown in Figure 5.16, *contrived states* are defined in this work as assembly deformations depicted in Figure 5.17. Each corner point colored grey deviates to the outward position colored red along the dashed line passing through the core center. The maximum x and y displacements of the assembly duct in the experimental breeder reactor-2 are 0.42 cm and 0.35 cm, respectively, in Reference [43]. The root-sum-squared displacement reaches about 9 % of the assembly pitch of the core. Thus, the displacement of assembly corner points with *contrived states* is determined as 9 % of the assembly pitch in this work.

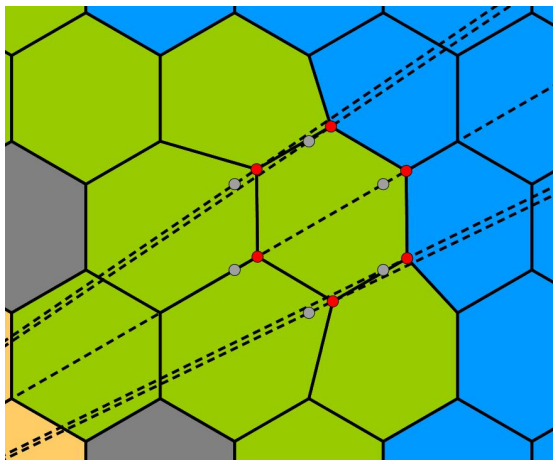

Figure 5.17. Radial core configuration with *contrived states* on one assembly.

5.3.2. SNR-300 Benchmark Problem with regularly structured geometry

The schneller natriumgekühlter reaktor-300 (SNR-300) is a sodium-cooled fast breeder reactor with 730 MW thermal power. The benchmark for this reactor provides the descriptions of the 3D core geometry and 4G macroscopic cross-section set.[44] The radial and axial core configurations are depicted in Figure 5.18 and Figure 5.19, respectively. Two 2D core problems including the upper core (UC) and lower core (LC) problems are incorporated in this benchmark. The outer control rod assembly is filled with the absorber and follower in the UC and LC problem, respectively, following the axial control rod insertion illustrated in Figure 5.19.

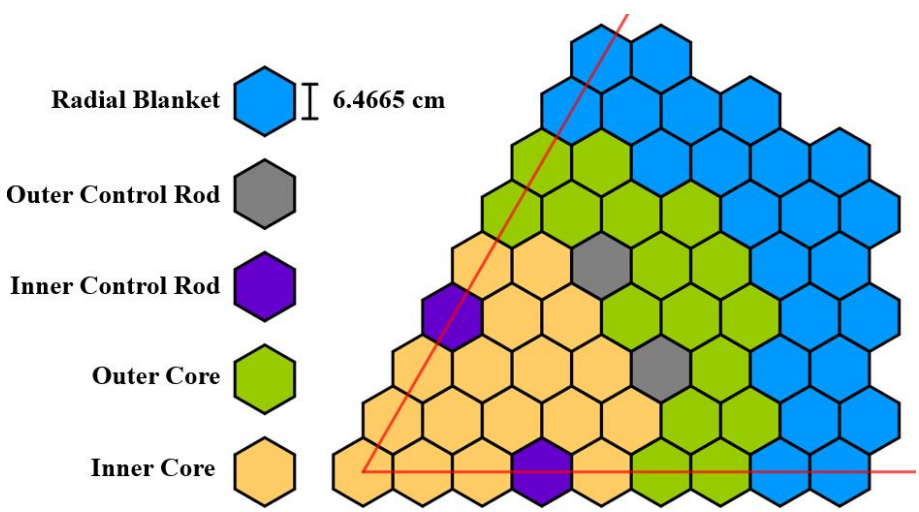

Figure 5.18. Radial core configuration of the SNR-300 benchmark problem.

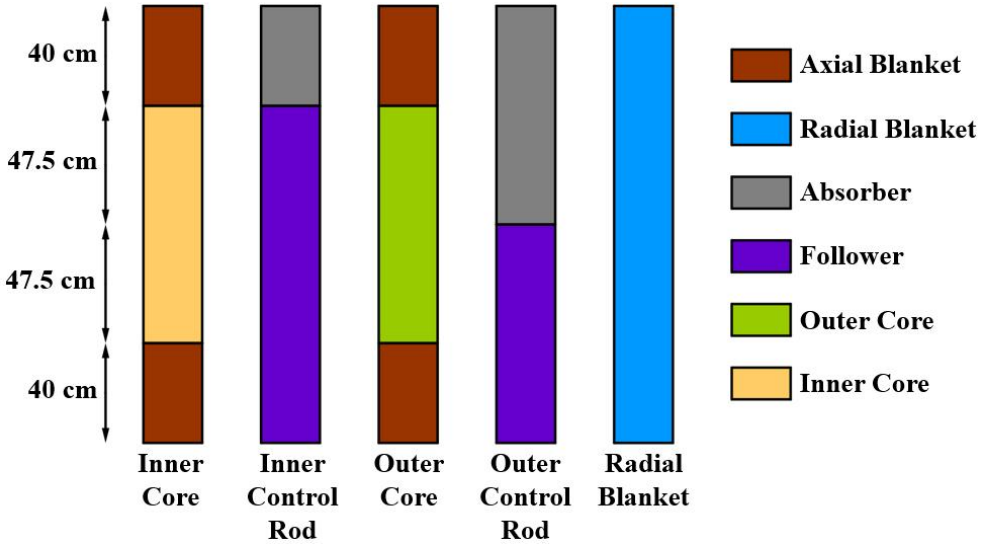

Figure 5.19. Axial core configuration of the SNR-300 benchmark problem.

The comparison results of the RENUS nodal solutions for the two 2D SNR-300 core problems with regularly structured geometry against the reference solutions produced by McCARD are summarized in Table 5.18. Each McCARD solution was determined as an average of three calculation results for the same problem with different random number seeds. Each McCARD calculation was conducted by using 100 inactive cycles, 300 active cycles, and 10 million particles per cycle. The standard deviation of assembly power distribution does not exceed 0.15 %. The solution differences in the UC problem with 508 pcm in reactivity and the maximum 3.38 % in assembly power distribution are larger than those in the LC problem due to the higher flux gradient in the core induced by the absorber in the outer control assembly. The McCARD assembly power and assembly power difference distributions are depicted in Figure 5.20 and Figure 5.21, respectively.

Table 5.18. Comparison of the RENUS solution for two 2D SNR-300 core problems with regularly structured geometry against the reference solution.

Case	Δρ (pcm)	Max. ΔP (%)	RMS ΔP (%)
UC	-508	3.38	1.71
LC	-270	2.40	1.34

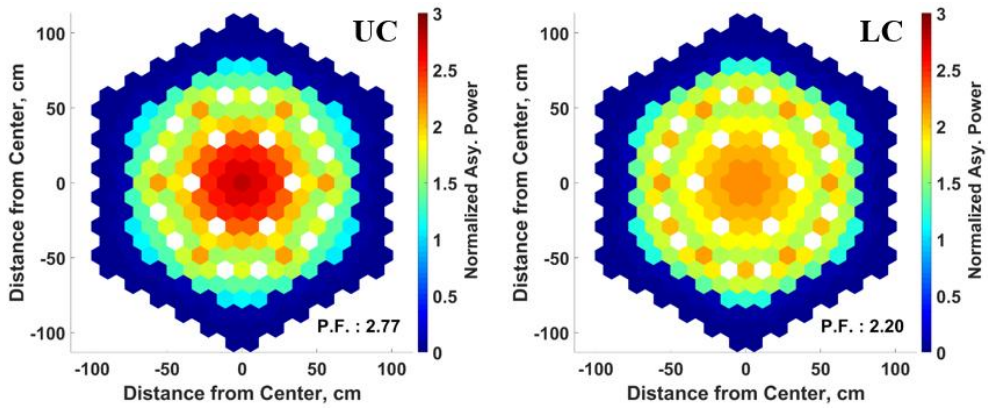

Figure 5.20. McCARD assembly power distribution for the two 2D SNR-300 core problems.

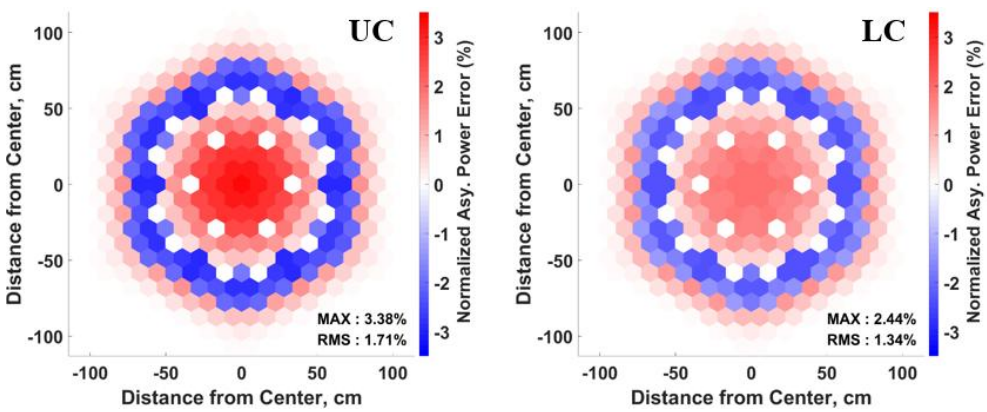

Figure 5.21. Assembly power difference distribution for the two 2D SNR-300 core problems.

In this work, the level of assembly power distribution is adjusted by dividing the power per volume for each assembly by the power per volume for the core. Concretely, the assembly power P_{xy}^{i} is adjusted as follows:

$$\bar{\boldsymbol{P}} = \sum_{i}^{N_{xy}} \sum_{g}^{G} \boldsymbol{\phi}_{g}^{i} \boldsymbol{k\Sigma}_{fg}^{i} \boldsymbol{V}^{i} / \sum_{i}^{N_{xy}} \boldsymbol{V}^{i}, \tag{5.1}$$

$$\boldsymbol{P}_{xy}^{i} = \sum_{g}^{G} \boldsymbol{\phi}_{g}^{i} \boldsymbol{k\Sigma}_{fg}^{i} / \bar{\boldsymbol{P}}, \tag{5.2}$$

where N_{xy} and G are the number of fuel assemblies and energy groups, respectively; ϕ_{g}^{i} and $k\Sigma_{fg}^{i}$ are the flux and kappa-fission macroscopic cross-section for the i-th assembly and g-th energy group, respectively; V^{i} is the i-th assembly volume.

5.3.3. 2D deformed SNR-300 core problems with uniform expansion

The masses of the fuel and structural materials are conserved after core deformations while the sodium coolant can backfill into the deformed domain. The factor R_{XS} is introduced in this work to deal with diverse cross-section changes as follows:

$$\boldsymbol{\Sigma' = \Sigma \times \frac{1}{1+R_{XS}\frac{V'-V}{V}}}, \tag{5.3}$$

where Σ and Σ' are the macroscopic cross-sections before and after assembly deformation, respectively; V and V' are the assembly volumes before and after assembly deformation, respectively. Note that the cross-section remains the same when R_{XS} is 0 %. It changes in inverse proportion to volume change when R_{XS} is 100 %. In this verification, the core problems with *contrived states* are solved with three different R_{XS} of 0 %, 50 %, and 100 %.

The arbitrarily deformed 2D SNR-300 core problems with uniform expansion are established in this work by applying *contrived states* on assemblies in the fuel region as depicted in Figure 5.22. The fuel assemblies are uniformly expanded in these problems except for the radial blanket of which the assembly power is negligible. For the two 2D SNR-300 core problems with three R_{XS}, six deformed 2D core problems were solved.

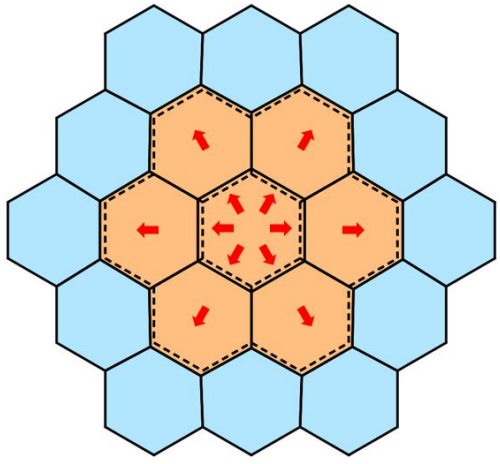

Figure 5.22. *Contrived states* on the fuel region.

The comparison results of k-eff values between RENUS and McCARD for the

deformed core problems are summarized in Table 5.19 and Table 5.20, respectively. The McCARD options for regularly structured geometry were also used here. Huge reactivity differences between the two solutions shown for regularly structured geometry remain almost the same after applying core deformation regardless of R_{XS}. The reactivity changes of the two solutions for the deformed core problem compared to the problem with regularly structured geometry match each other within 7 pcm. In contrast, the reference reactivity changes from -240 pcm to 192 pcm. It is demonstrated that RENUS reproduces reactivity changes in the reference solution induced by core deformations with high accuracy.

Table 5.19. Comparison of the k-eff values for the deformed 2D SNR-300 core problems with uniform expansion.

k-eff		Regular	Deformed (Rxs) 0 %	50 %	100 %
UC	McCARD	1.13258	1.13496	1.13226	1.12960
	RENUS	1.12610	1.12854	1.12574	1.12307
	Δρ (pcm)	-508	-501	-512	-515
LC	McCARD	1.23297	1.23399	1.23221	1.23046
	RENUS	1.22888	1.22987	1.22807	1.22632
	Δρ (pcm)	-270	-271	-274	-274

Table 5.20. Comparison of the reactivity changes for the deformed 2D SNR-300 core problems with uniform expansion.

Δρ (pcm) vs. Regular		Deformed (Rxs) 0 %	50 %	100 %
UC	McCARD	185	-25	-233
	RENUS	192	-28	-240
	del	7	-3	-7
LC	McCARD	67	-50	-165
	RENUS	66	-54	-170
	del	-2	-4	-4

The comparison results of assembly power and assembly power change distributions between the two solutions for the deformed core problems are summarized in Table 5.21 and Table 5.22. The assembly power differences between the two solutions for the LC problem after core deformation remain almost the same. Those for the UC problem are even decreased. The changes in assembly power distribution of the two solutions for the deformed core problem compared to the problem with regularly structured geometry match each other within 0.46 %. In contrast, the reference assembly power changes by up to 47.76 %. The McCARD assembly power, McCARD assembly power changes, and assembly power change

del distributions for the deformed LC problem with 0 % R_{XS} and the deformed UC problem with 100 % R_{XS} are presented in Figure 5.23-Figure 5.25, respectively. The assembly power change *del* is defined in this work as the RENUS and McCARD difference of the assembly power change in the deformed core problem. For example, the McCARD and RENUS assembly power at the core center change by about -47.76 % and -48.22 %, respectively, in the deformed UC problem with 100 % R_{XS}. Therefore, the assembly power change *del* at the core center is 0.46 % in this problem. All assembly power change *del* distribution for the six core problems are small enough compared to assembly power change distributions. These results reveal that the RENUS unstructured nodal solution and the reference solution match each other well in assembly power changes induced by core deformations.

Table 5.21. Comparison of the assembly power distribution for the deformed 2D SNR-300 core problems with uniform expansion.

Abs. ΔP (%)		Regular	Deformed (Rxs) 0 %	50 %	100 %
UC	Max.	3.38	3.47	3.11	2.96
	RMS	1.71	1.72	1.69	1.68
LC	Max.	2.44	2.41	2.41	2.40
	RMS	1.34	1.34	1.33	1.33

Table 5.22. Comparison of the assembly power change distribution for the deformed 2D SNR-300 core problems with uniform expansion.

Abs. ΔP (%) vs. Regular			Deformed (Rxs) 0 %	50 %	100 %
UC	McCARD	Max.	3.79	27.13	47.76
		RMS	2.33	3.14	4.64
	RENUS	Max.	3.72	27.4	48.22
		RMS	2.33	3.17	4.7
	del	Max.	0.09	0.27	0.46
		RMS	0.03	0.04	0.06
LC	McCARD	Max.	3.61	20.94	36.63
		RMS	2.15	2.61	3.58
	RENUS	Max.	3.56	21.08	36.9
		RMS	2.15	2.62	3.61
	del	Max.	0.06	0.13	0.27
		RMS	0.02	0.03	0.05

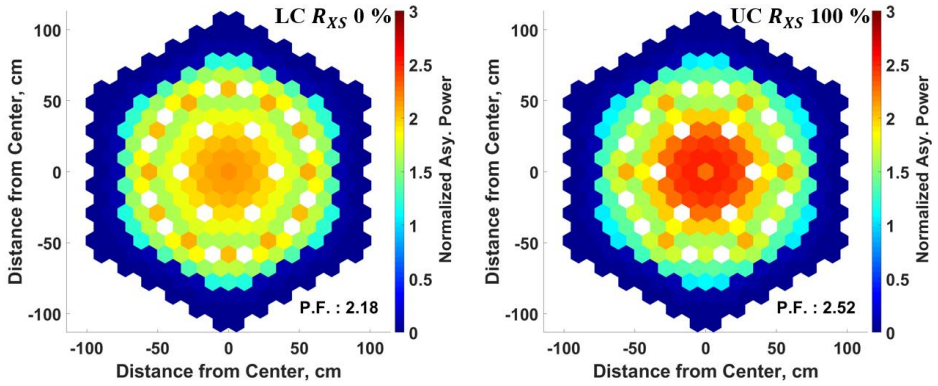

Figure 5.23. McCARD assembly power distribution for the deformed 2D SNR-300 core problems with uniform expansion.

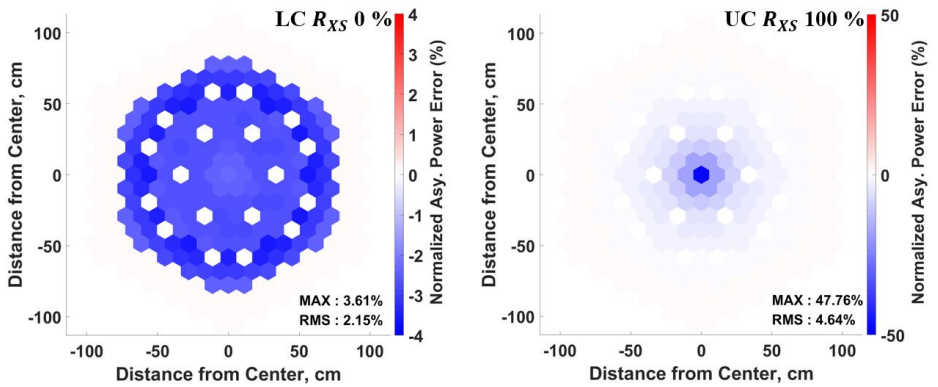

Figure 5.24. McCARD assembly power change distribution for the deformed 2D SNR-300 core problems with uniform expansion.

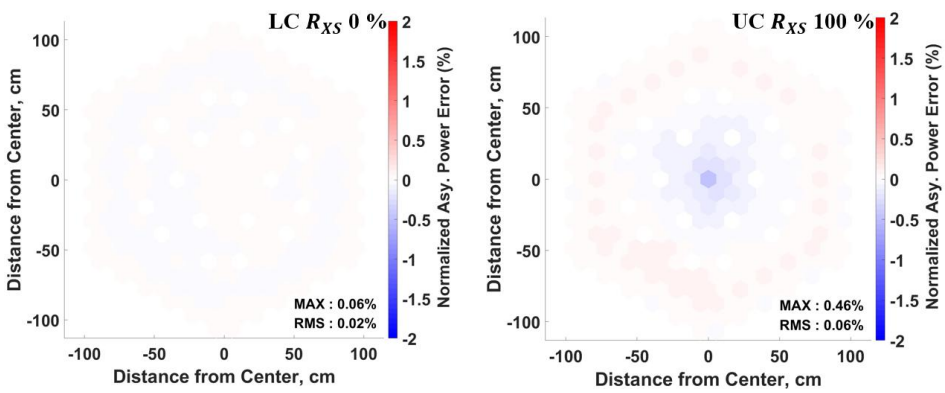

Figure 5.25. Assembly power change *del* distribution for the deformed 2D SNR-300 core problems with uniform expansion.

5.3.4. 2D deformed SNR-300 core problems with assembly-wise expansion

The excellent agreements for the changes in nuclear characteristics between the two solutions for the deformed core problems presented in the previous subsection can result from a cancellation between opposite solution errors in assemblies. Therefore, it needs to investigate the cores with *contrived state*s on each assembly. In this work, twenty-two core problems were established additionally for the UC and LC problems, respectively, by applying *contrived states* to a group of assemblies. Concretely, c*ontrived states* were applied to one of the assemblies shown in Figure 5.26. *Contrived states* were also applied to the assemblies, which overlaps with the assembly when reflected on the 30-degree lines passing through the core center. For example, *contrived states* are applied to the twelve assemblies expressed as diagonal lines in Figure 5.27 in case 17. By duplicating assembly deformations in the azimuthal direction, the changes in nuclear characteristics are amplified, and the resolution of solution differences is increased. One hundred and twenty-six core problems were solved with the twenty-one cases, UC and LC problems, and three different R_{XS}. The McCARD solutions exploited in the following verifications were obtained by using the same options described in Subsection 5.3.2.

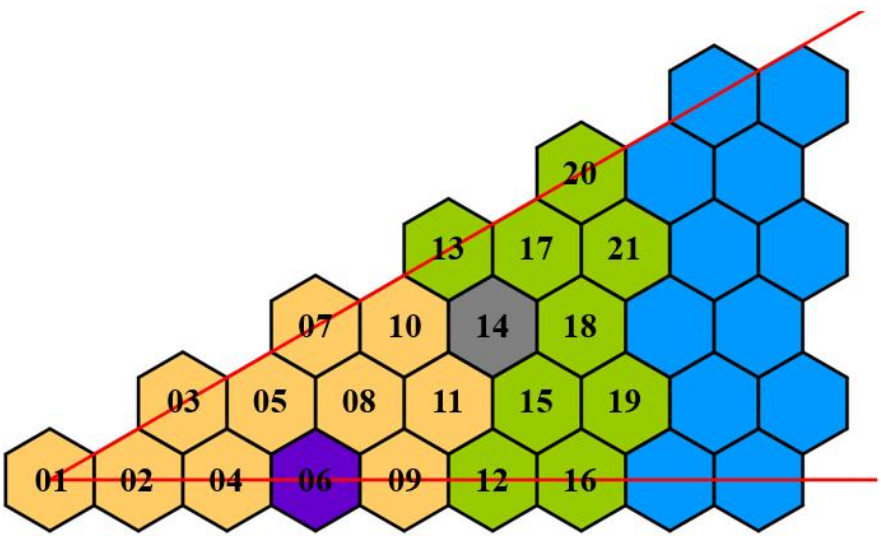

Figure 5.26. Radial core configuration of the SNR-300 benchmark problem in the range of 30-degree.

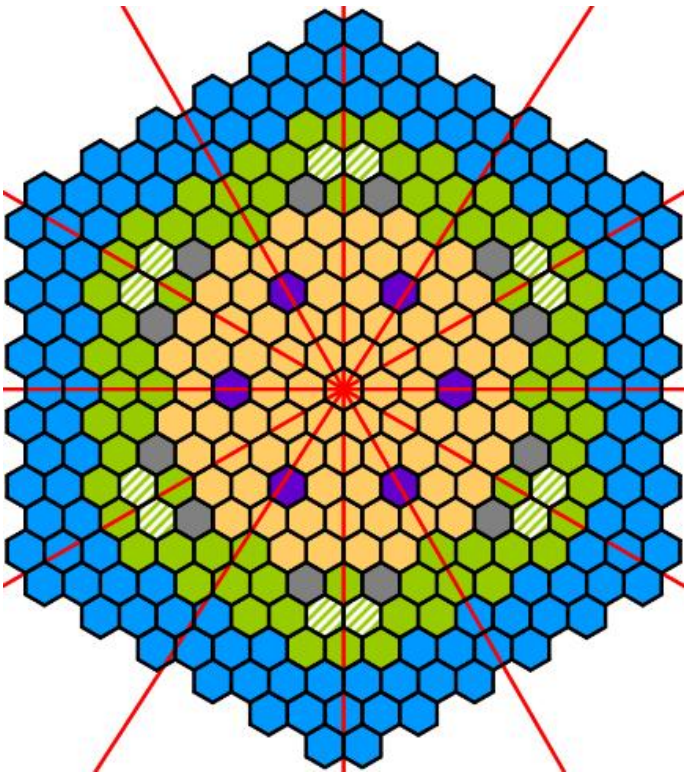

Figure 5.27. Deformed assemblies (expressed as diagonal lines) in the deformed 2D SNR-300 core problem with assembly-wise expansion (case 17).

The comparison results of the reactivity changes between the two solutions for the deformed core problems are presented in Figure 5.28-Figure 5.33. The values in each assembly are the calculation results for the deformed core problem with *contrived states* on the assembly. Those values are the McCARD and RENUS reactivity changes and the reactivity change *del* between the two solutions. The reference reactivity changes by up to 383 pcm in the UC problem case 10 with 0 % R_{XS}. The reactivity changes of the two solutions match each other within 18 pcm.

The comparison results of the assembly power change distribution between the two solutions for the deformed core problems are presented in Figure 5.34-Figure 5.39. The values in each assembly are the calculation results for the deformed core problem with *contrived states* on the assembly. The McCARD and RENUS assembly power changes and the assembly power change *del* between the two solutions are represented in columns at each assembly. The maximum and RMS values are represented in rows at each column. The reference assembly power changes by up to 45.52 % in the UC problem case 2 with 100 % R_{XS}. The assembly power changes of the two solutions match each other within 0.40 %.

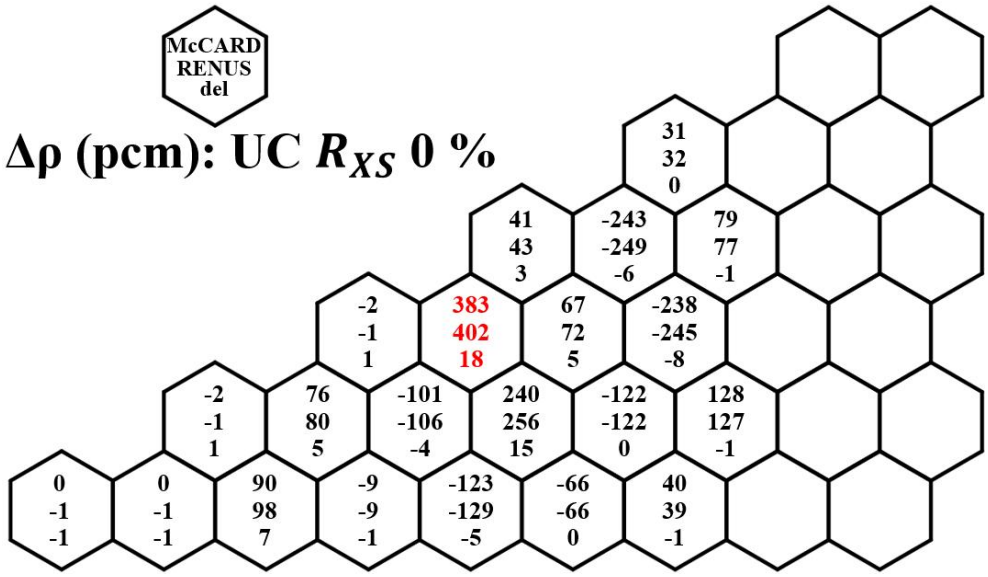

Figure 5.28. Comparison of the reactivity changes for the deformed UC problems with assembly-wise expansion and 0 % R_{XS}.

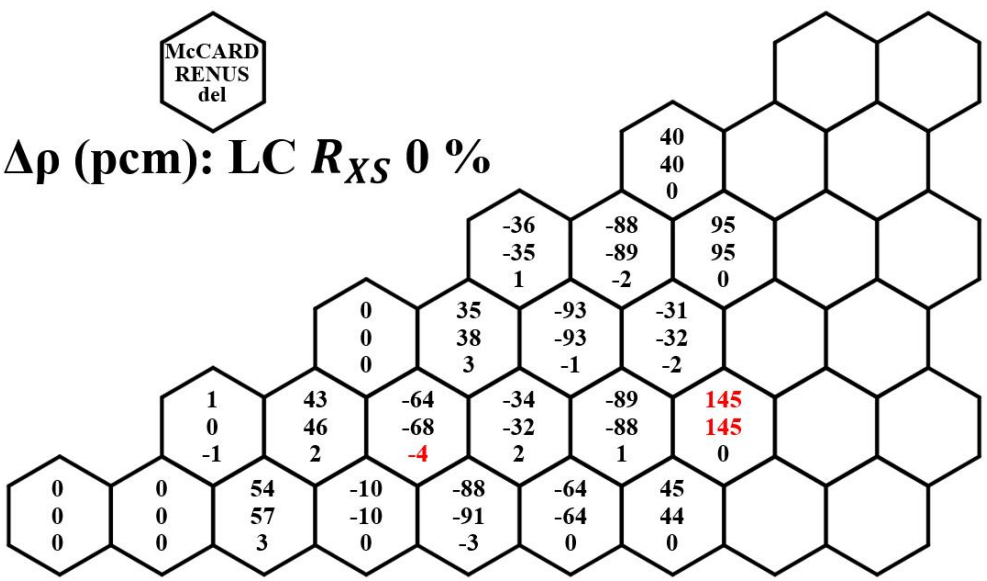

Figure 5.29. Comparison of the reactivity changes for the deformed LC problems with assembly-wise expansion and 0 % R_{XS}.

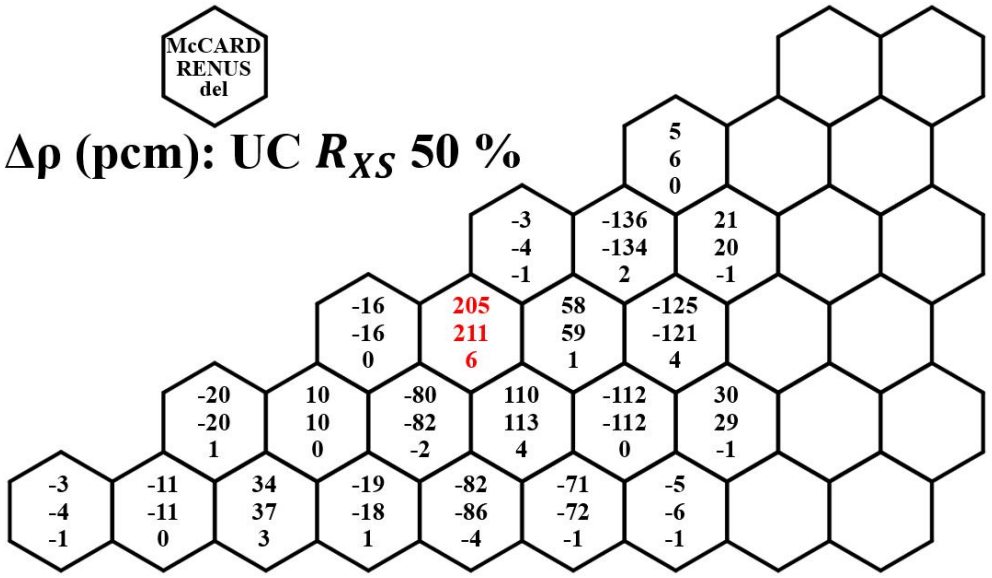

Figure 5.30. Comparison of the reactivity changes for the deformed UC problems with assembly-wise expansion and 50 % R_{XS}.

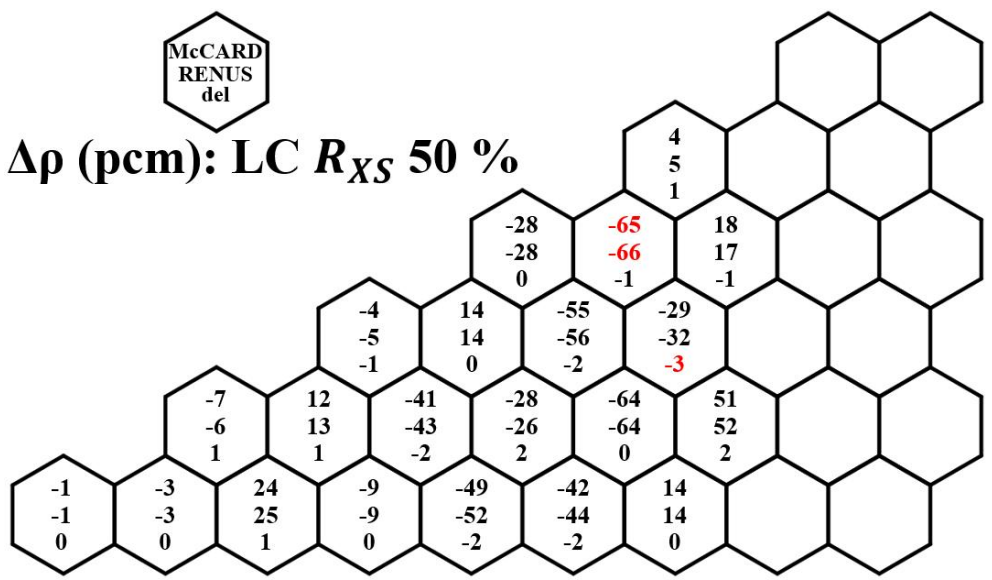

Figure 5.31. Comparison of the reactivity changes for the deformed LC problems with assembly-wise expansion and 50 % R_{XS}.

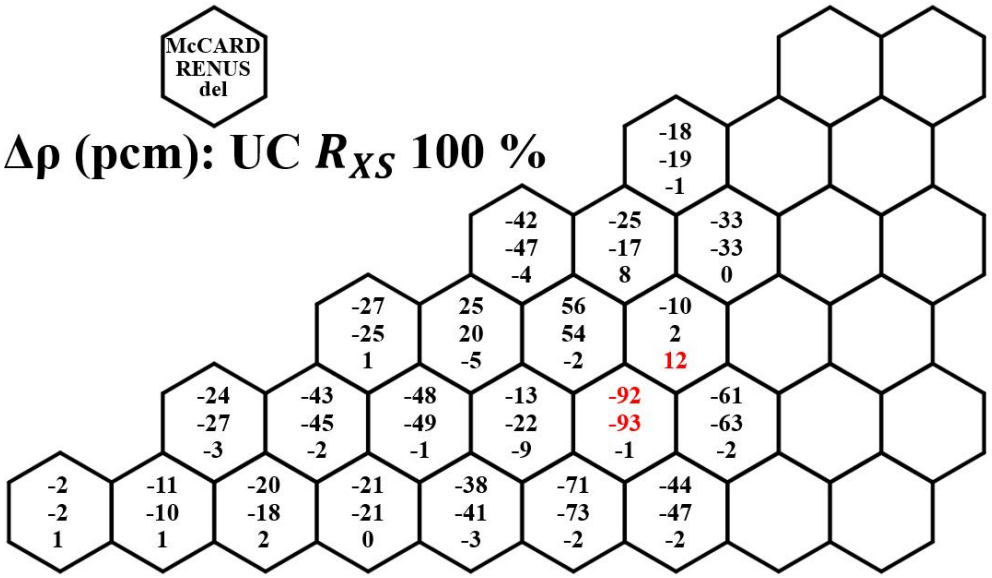

Figure 5.32. Comparison of the reactivity changes for the deformed UC problems with assembly-wise expansion and 100 % R_{XS}.

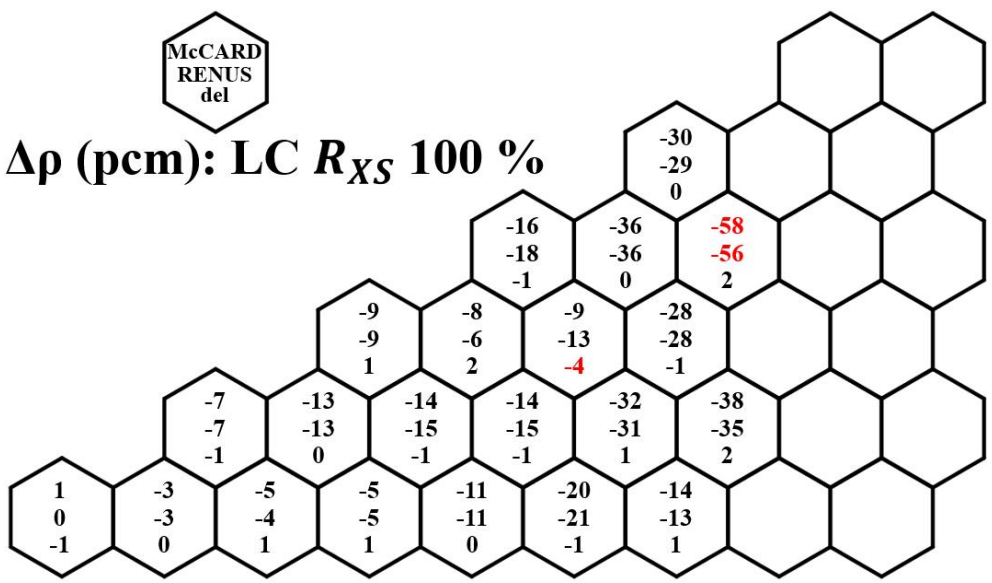

Figure 5.33. Comparison of the reactivity changes for the deformed LC problems with assembly-wise expansion and 100 % R_{XS}.

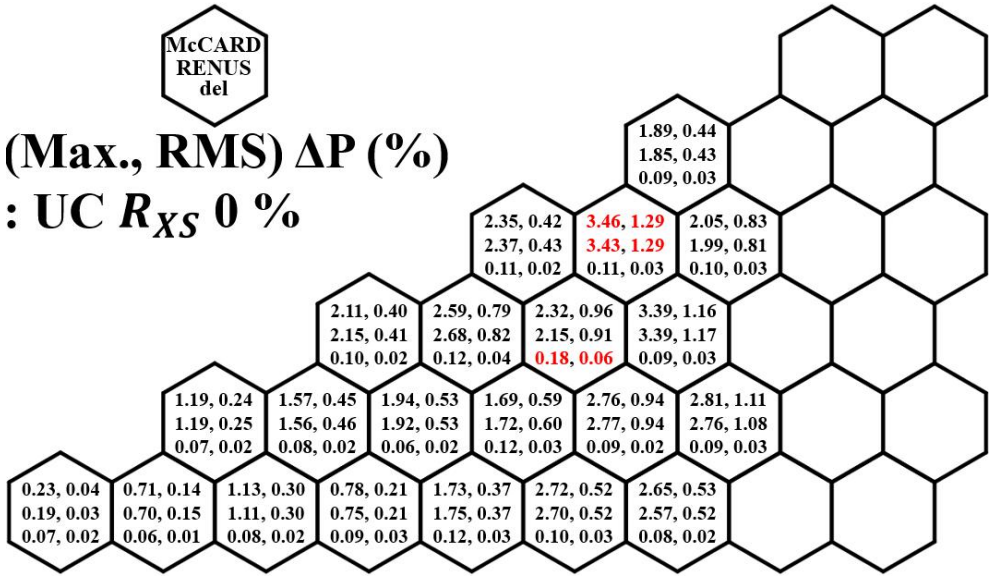

Figure 5.34. Comparison of the assembly power change distribution for the deformed UC problems with assembly-wise expansion and 0 % R_{XS}.

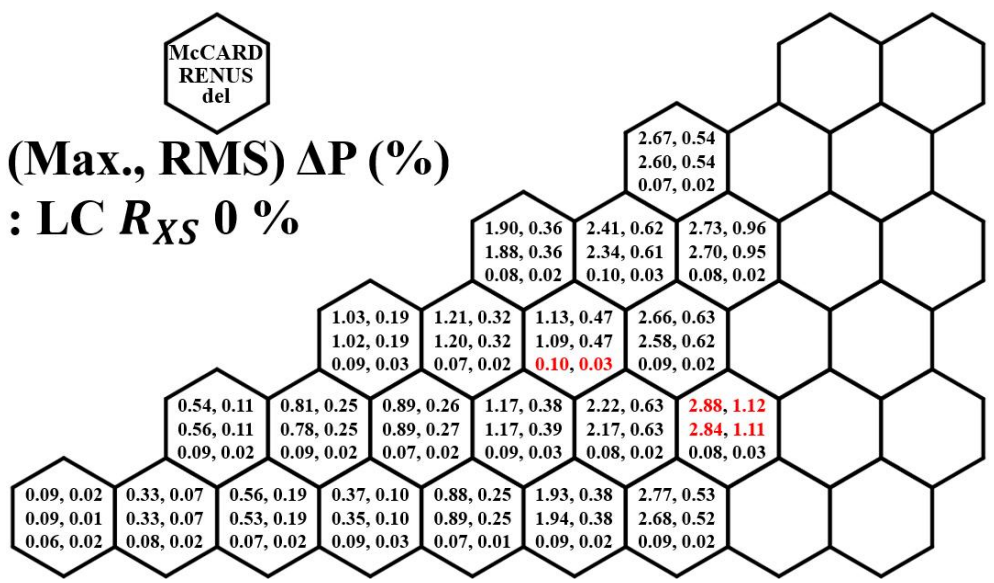

Figure 5.35. Comparison of the assembly power change distribution for the deformed LC problems with assembly-wise expansion and 0 % R_{XS}.

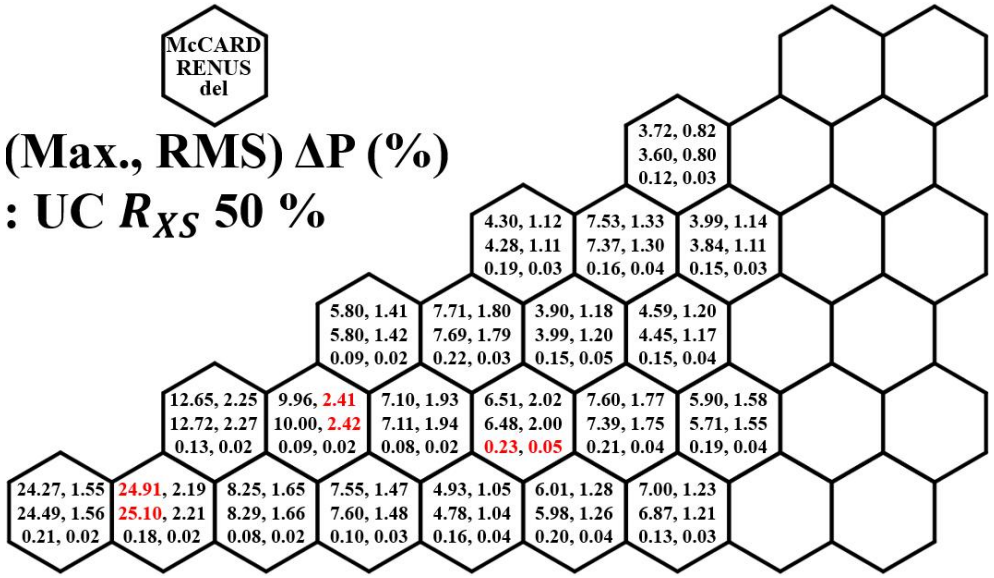

Figure 5.36. Comparison of the assembly power change distribution for the deformed UC problems with assembly-wise expansion and 50 % R_{XS}.

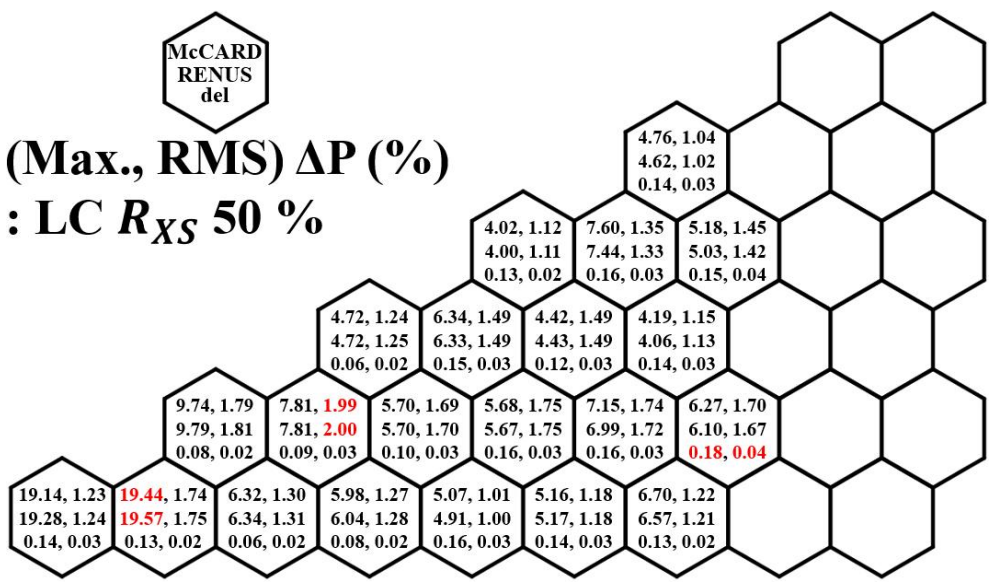

Figure 5.37. Comparison of the assembly power change distribution for the deformed LC problems with assembly-wise expansion and 50 % R_{XS}.

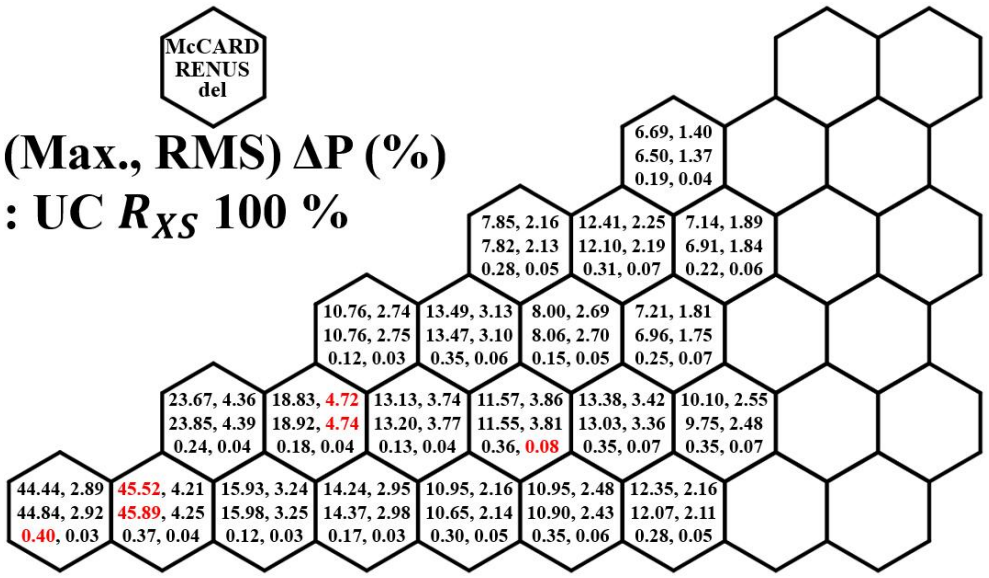

Figure 5.38. Comparison of the assembly power change distribution for the deformed UC problems with assembly-wise expansion and 100 % R_{XS}.

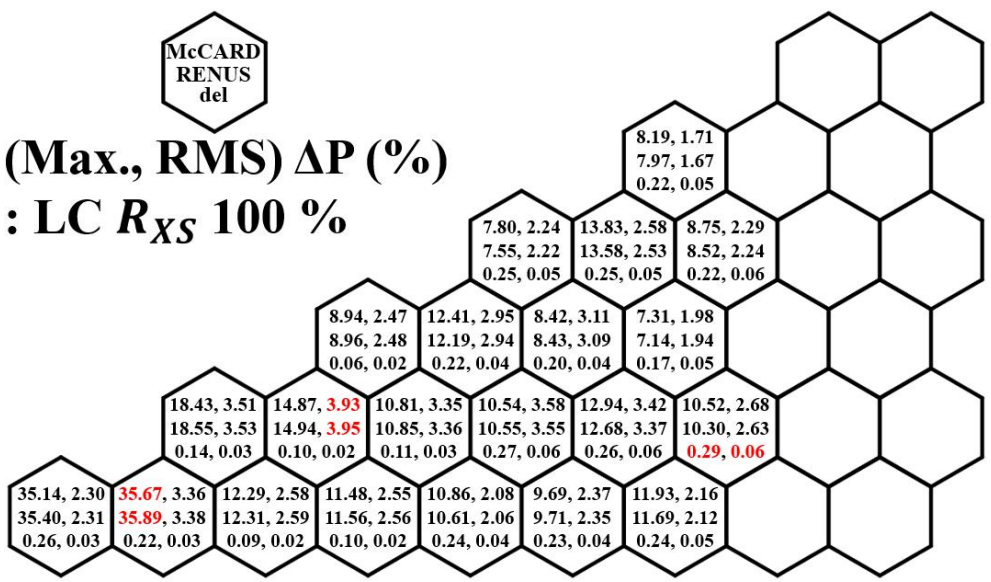

Figure 5.39. Comparison of the assembly power change distribution for the deformed LC problems with assembly-wise expansion and 100 % R_{XS}.

The McCARD assembly power, McCARD assembly power changes, and assembly power change *del* distributions for the deformed LC problem case 18 with 0 % R_{XS} and the deformed UC problem case 02 with 100 % R_{XS} are depicted in Figure 5.40-Figure 5.42, respectively.

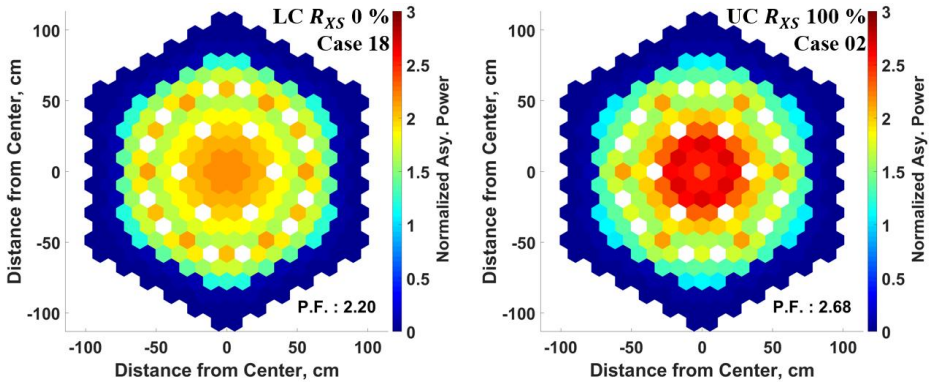

Figure 5.40. McCARD assembly power distribution for the deformed 2D SNR-300 core problems with assembly-wise expansion.

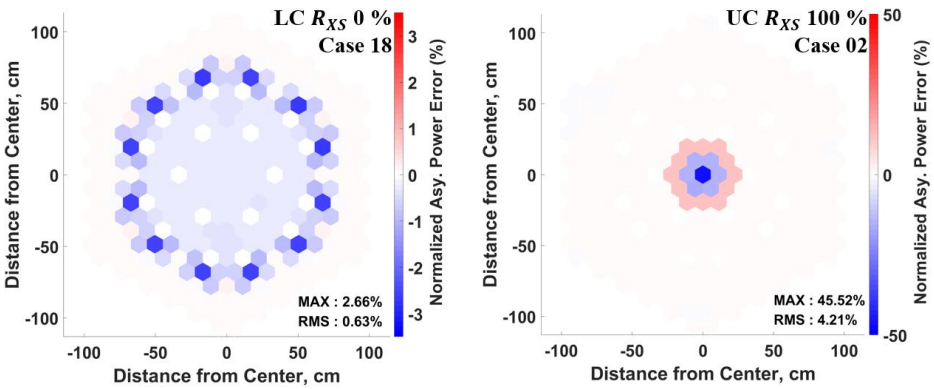

Figure 5.41. McCARD assembly power change distribution for the deformed 2D SNR-300 core problems with assembly-wise expansion.

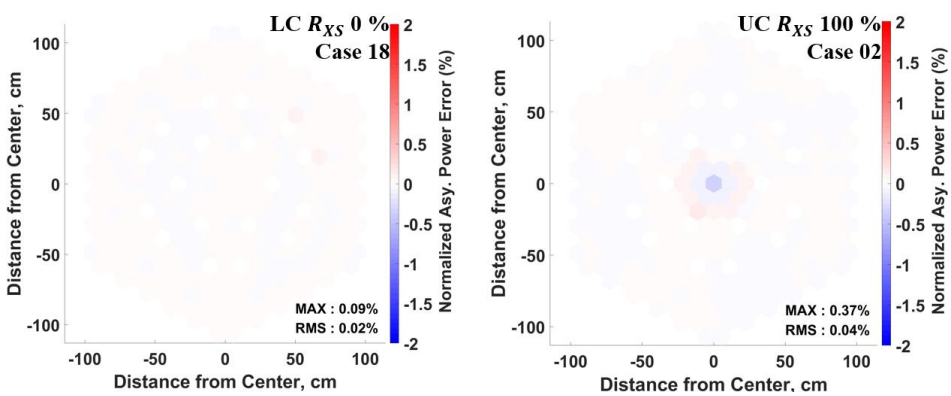

Figure 5.42. Assembly power change *del* distribution for the deformed 2D SNR-300 core problems with assembly-wise expansion.

The reactivity *dels* and assembly power change *del* distributions for all deformed core problems with assembly-wise expansion are small enough compared to the reference reactivity changes and assembly power change distributions, respectively. Therefore, it is concluded that the highly accurate RENUS solutions for predicting the changes in nuclear characteristics induced by uniform expansion on the fuel region do not owe to any error cancellation.

Summary and Conclusions

In this work, the hexagonal ray tracing module and coarse mesh finite difference (CMFD) acceleration, which are capable of explicitly modeling hexagonal geometry cores including complicated structures, are developed in a direct whole core calculation (DWCC) code, nTRACER. The hexagonal ray tracing calculation in nTRACER is parallelized efficiently by employing the assembly-wise domain decomposition (ADD) scheme. The hexagonal assembly-wise nodal solution is expanded to the unstructured geometry so that the high-fidelity analyses of sodium-cooled fast reactor (SFR) core deformations can be conducted in a practical time. The nTRACER solution accuracy is verified by comparing its calculation results for the various hexagonal geometry core problems against the reference solutions. The ADD performance is examined by comparing the ray tracing time *with* or *without* the ADD scheme for the water-water energetic reactor (VVER) core problems. The accuracy of the unstructured hexagonal nodal solution in RENUS is verified by comparing its calculation results for the arbitrarily deformed 2D SFR core problems against the McCARD results.

Both VVERs, which have spread widely in the East-European bloc and developing countries for several decades, and SFRs, which are estimated to have the highest feasibility of commercial operations among Generation-VI reactors, have a hexagonal geometry core. The unusual structures such as Vygorodka and the corner stiffener in VVERs and assemblies with different rod sizes in SFRs undermine the assumptions of the diffusion equation and assembly or pin homogenization, on which the two-step core calculation (TSCC) code systems base. Thus, the hexagonal ray tracing module and CMFD acceleration are developed in nTRACER to attain the solution for VVER and SFR core problems with high accuracy in this research. The *elongated* model is employed in the hexagonal ray tracing module to explicitly model Vygorodka and the assembly duct of VVER cores. This model expands the periphery fuel cell into a pentagon so that the gap cell becomes a parallelogram. The memory required to construct cell-wise module rays increases in this model due to the various cell types in hexagonal geometry. Thus, the hexagonal ray calculation in nTRACER is conducted by using the assembly-wise modular rays.

The CMFD formulation for regular square cells cannot solve the various cell types in the *elongated* model. Thus, the CMFD formulation is expanded to the unstructured geometry by applying flexibility to the surface length, mesh width, and the number of neighboring meshes. The performance of CMFD calculations would

be deteriorated by incorporating CMFD meshes for the tiny gap cells in VVER cores in that a significant computing resource is consumed additionally while solution accuracy improvement is negligible. Thus, the super pin scheme, which is to homogenize the periphery fuel cell and gap cell into one cell in the CMFD calculation, is employed in nTRACER. Consequently, the CMFD calculation time and total computing time for the 2D VVER core problems are reduced by up to 39 % and 17 %, respectively.

DWCC solutions have higher accuracy and resolution compared to TSCC solutions while they require an enormous computing resource and time. Thus, it is necessary for DWCC solutions to reduce memory usage and improve parallel efficiency. nTRACER divides a 3D core into several planes, on which ray tracing calculations are conducted in parallel by using processors of computing nodes. Each planar ray tracing calculation is also conducted in parallel by using threads of CPUs. The angle-wise parallelization, where threads trace tracking rays in parallel across the whole problem domain, requires an enormous memory, which increases computing time by inducing high fetching overhead. This problem is alleviated by using the ADD scheme to let each thread trace the rays in one assembly. Memory reduction and consequent reduction in computing time are possible since storing the flat source region (FSR) information is needed only for the assemblies being computed currently. On the other hand, the convergence of method of characteristics (MOC) calculations would be deteriorated in ADD calculations due to the lag in updating the incoming angular fluxes at the assembly surface. This deterioration is relaxed by updating the angular fluxes after CMFD calculations and by using the three-color scheme. The three-color scheme is to sweep all assemblies belonging to one color and then use the outgoing angular fluxes of those assemblies in updating the incoming angular fluxes of the other colored assemblies. The total computing time for the 2D VVER core problems is reduced by up to 13 % by reducing the number of MOC iterations. The angular flux storage scheme (AFSS), which is to store the angular flux changes and conduct moment calculations at the end of the ray tracing calculation, is also used in nTRACER. The total computing time for the 2D VVER core problems is reduced by up to 23 % by avoiding expensive moment calculations during ray tracing calculations.

The critical characteristic of an SFR core is the thermal core expansion induced by high power density and steep temperature gradient, which significantly impacts reactivity and power distribution. A finite difference method, finite element method, and Monte Carlo method, which have been used in the analyses of SFR core

deformations, have a drawback in that they require an enormous computing resource to attain sufficient solution accuracy. On the other hand, a nodal solution requiring the smallest calculation burden has been established only for regularly structured geometries so far. In this work, the unstructured nodal solution is developed in RENUS to overcome this problem. The triangle-based polynomial expansion nodal (T-PEN) method, corner point balance (CPB) solution, and CMFD formulation are expanded to the irregularly deformed hexagonal geometry. The linear systems in the T-PEN method and CPB solution are constructed by substituting the *derived* group variables with an equation of the *representative* group variables in the physical constraints. The curvilinear and surface integrals of basic functions incorporated in the variable expressions need to be calculated for unstructured geometry to conduct this conversion. The method, which is to split a polygon into several parallelograms and calculate the polynomial integrals in each parallelogram by using the look-up table formulated in advance, is suggested. The unstructured nodal solution is implemented in RENUS by expressing the surface and areal variables in arbitrary geometry as linear combination of polynomials by using this method. The CMFD formulation in RENUS is expanded to the unstructured geometry similarly to nTRACER.

The solution accuracy of nTRACER is verified by comparing its calculation results for the various hexagonal geometry core problems against the McCARD results. The reactivity difference and the maximum and root-mean-square 3D pin power differences do not exceed 7 pcm, 6.41 %, and 0.44 %, respectively, for the three 3D C5G7 H benchmark problems with different control rod insertions. For the nine 2D VVER-1000 core problems proposed by KAERI with different fuel and coolant temperatures and boron concentrations, the solution differences do not exceed 106 pcm, 2.24 %, and 0.95 %, respectively, by using the P0 option. It is demonstrated that the nTRACER solution difference is reduced by using the P2 option, especially for the problems in operation state with low boron concentration. The solution differences are reduced by up to 70 pcm, 0.25 %, and 0.12 %, respectively, by using the P2 option. The nTRACER and McCARD solutions for the 2D 'Full-core' VVER-440 and MET-1000 SFR core problems also match each other well by using the P2 option. It is demonstrated that nTRACER achieved satisfactory solution accuracy for hexagonal geometry core problems.

The ADD performance is examined by comparing the ray tracing time *with* and *without* the ADD scheme for the various VVER core problems. The maximum difference in reactivity and pin power distribution induced by the ADD scheme do

not exceed 1 % and 0.78 %, respectively. For the 2D one-sixth and full core problems, the ray tracing time is reduced by up to 18 % and 48 %, respectively. The total computing time is reduced by up to 6 % and 38 %, respectively. For the 3D one-sixth and full core problems, the ray tracing time is reduced by up to 44 % and 53 %, respectively. The total computing time is reduced by up to 36 % and 45 %, respectively. It is verified that the hexagonal ray tracing calculation in nTRACER is parallelized efficiently by employing the ADD scheme.

The performance of the unstructured hexagonal nodal solution in RENUS is verified by comparing its calculation results for the 2D arbitrarily deformed schneller natriumgekühlter reaktor-300 (SNR-300) core problems against the McCARD results. The *contrived state* is defined here as an arbitrary core deformation to deviate assembly corner points outward by 9 % of the assembly pitch. The solution differences for the 2D SNR-300 core problems with regularly structured geometry are somewhat large, up to 508 pcm in reactivity and 3.38 % in assembly power distribution. Nonetheless, RENUS reproduces the changes in reactivity and assembly power distribution in the reference solution induced by *contrived states* on the fuel region within 7 pcm and 0.46 %, respectively. In contrast, the reference reactivity and assembly power change by up to 240 pcm and 47.76 %, respectively. A cancellation between opposite solution errors in assemblies may exist for the deformed core problem with uniform expansion. Therefore, the RENUS solutions were further verified by decomposing the deformed core problem with uniform expansion into the deformed core problems with assembly-wise expansion. The reactivity and assembly power changes of the two solutions match each other within 18 pcm and 0.40 %, respectively, while they change by up to 383 pcm and 45.52 %, respectively. It is demonstrated by these verification results that excellent agreements between the two solutions for the deformed core problems do not owe to any error cancellation. Thus, it is concluded that RENUS attained significantly high accuracy in predicting the changes in nuclear characteristics induced by core deformations by using the unstructured nodal solution.

In this work, the high-fidelity hexagonal geometry core analysis system capable of diverse applications is facilitated by developing the hexagonal ray tracing module and CMFD acceleration in nTRACER and by expanding the nodal solution in RENUS to the unstructured geometry. nTRACER reproduces the reference solution for hexagonal geometry core problems with high accuracy by explicitly modeling the complicated geometries of VVER and SFR cores. The practicality of the nTRACER solution is improved as the ray tracing time is reduced by employing the

ADD scheme. RENUS reproduces the McCARD solution changes for the 2D arbitrarily deformed hexagonal geometry core problems with high accuracy by using the unstructured nodal solution. Due to its accuracy and practicality, nTRACER coupled with T/H codes is currently used in the multi-physics analyses of VVER cores. It is expected that this hexagonal geometry core analysis system would also provide the comprehensive analyses of SFR cores including thermal core expansion.

References

[1] J. Y. Cho *et al.*, "Whole core transport calculation employing hexagonal modular ray tracing and CMFD formulation," *Journal of nuclear science and technology*, **45.8**, pp. 740-751 (2008).

[2] Y. S. Jung, C. B. Shin, C. H Lim, and H. G. Joo, "Practical numerical reactor employing direct whole core neutronic transport and subchannel thermal/hydraulic solvers," *Annals of Nuclear Energy*, **62**, pp. 357-374 (2013).

[3] B. Kochunas *et al.*, "Overview of development and design of MPACT: Michigan parallel characteristics transport code," *Proceedings of M&C 2013*, Sun Valley, ID, USA, May 5-9 (2013).

[4] S. Y. Choi, C. H. Lee, and D. J. Lee, "Resonance treatment using pin-based pointwise energy slowing-down method," *Journal of Computational Physics*, **330.1**, pp. 134-155 (2017).

[5] C. B. Shim, J. Y. Cho, and K. H. Lee, "Core Follow Calculation for a VVER-1000 Reactor in Cycles 1 through 6 using DeCART2D/MASTER," *Proceedings of M&C 2017*, Jeju, Korea, April 16-20 (2017).

[6] J. Jang *et al.*, "Analysis of Rostov-II Benchmark Using Conventional Two-Step Code Systems," *Energies*, **15.9**, 3318 (2022).

[7] J. Y. Cho *et al.*, "Improvement and verification of the DeCART code for HTGR core physics analysis," *Nuclear Engineering and Technology*, **51**, pp. 13-30 (2019).

[8] D. Xianan *et al.*, "Application of TULIP/STREAM code in 2-D fast reactor core high-fidelity neutronic analysis," *Nuclear Engineering and Technology*, **51**, pp. 1871-1885 (2019).

[9] T. Ghaddar *et al.*, "Hexagonal Geometries in MPACT," No. ORNL/TM-2021/2180. ORNL, TN, USA (2021).

[10] Z. Liu *et al.*, "Development and verification of the hexagonal core simulation capability of the NECP-X code," *Annals of Nuclear Energy*, **179**, 109388 (2022).

[11] M. Papadionysiou *et al.*, "Validation of the novel core solver nTRACER-COBRA-TF for Full Core High Fidelity Cycle Analysis of VVERs," *Nuclear Engineering and Design*, **398**, 111946 (2022).

[12] J. Gonzalez-Amoros *et al.*, "Capability extension of a high-resolution thermal-hydraulics code ESCOT for hexagonal geometry core multiphysics analysis," *Nuclear Science and Engineering*, 1-22 (2022).

[13] S. Kosaka and E. Saji, "Transport theory calculation for a heterogeneous multi assembly problem by characteristics method with direct neutron path linking technique," *Journal of Nuclear Science and Technology*, **37.12**, pp. 1015-1023 (2000).

[14] B. Kochunas and T. J. Downar, "Parallel 3-D method of characteristics in MPACT," *Proceedings of M&C 2013*, Sun Valley, ID, USA, May 5-9 (2013).

[15] L. Giorgio, M. Mauro, and T. Nicola, "Generation IV nuclear reactors: Current status and future prospects," *Energy Policy*, **61**, pp. 1503-1520 (2013).

[16] G. M. Greenman, "Calculation of the reactivity feedback due to core assembly bowing in LMFBRs," Argonne Natl. Lab, IL,USA (1984).

[17] P. J. Finck, "A technique for computing the reactivity feedback due to core-assembly bowing in LMFBR's," Argonne National Lab., No. FRA-TM-159, IL,

USA (1987).
[18] G. Palmiotti, J. M. Rieunier, C. Gho, and M. Salvatores, "BISTRO Optimized Two Dimensional Sn Transport Code," *Topical Meeting on Advances in Reactor Physics, Mathematics and Computation*, Paris, France, April (1987).
[19] C. Fiorina, I. D. Clifford, M. Aufiero, and K. Mikityuk, "GeN-Foam: a novel OpenFOAM based multi-physics solver for 2D/3D transient analysis of nuclear reactors," *Nuclear Engineering and Design*, **294**, pp. 24–37 (2015).
[20] E. R. Shemon *et al*., "NEAMS Neutronics: Development and Validation Status," *Proceedings of ICAPP 2014*, Charlotte, USA, April 6-9 (2014).
[21] J. I. Yoon and H. G. Joo, "Two-Level Coarse Mesh Finite Difference Formulation with Multigroup Source Expansion Nodal Kernels," *Journal of Nuclear Science and Technology*, **45.7**, pp. 668-682 (2008).
[22] J. Y. Cho *et al.*, "Non-linear triangle-based polynomial expansion nodal method for hexagonal core analysis," No. KAERI/TR-1652/2000, Korea Atomic Energy Research Institute (2000).
[23] Y. H. Choi *et al.*, VVER1000 reactor benchmark problems," Technical Report, KAERI/TR-7339/2018, Korea Atomic Energy Research Institute (2018).
[24] T. Lötsch *et al*., "The X2 benchmark for VVER-1000 reactor calculations. Overview and current status," *Proceedings of the 26th AER Symposium on VVER Reactor Physics and Reactor Safety*, Helsinki, Finland, October 8-12 (2016).
[25] B., Yuri, E. Fridman, and T. Lötsch., "X2 VVER-1000 benchmark revision: Fresh HZP core state and the reference Monte Carlo solution," *Annals of Nuclear Energy*, **144**, 107558 (2020).
[26] V. Krysl, "'FULL-CORE' VVER-440 pin power distribution calculation benchmark proposal," *AER Working Groups A&B*, Plzen, Czech Republic, May 10-11 (2011).
[27] G. Hegyi, M. Makai, and C. Maraczy, "Diffusion benchmark calculation of a VVER-440 core with 180° symmetry," *Proceedings of the 8th AER Symposium on VVER Reactor Physics and Reactor Safety*, Bystfice nad Perstejnem, Czech Republic, September 21 - 25 (1998).
[28] N. E. Stauff *et al.*, "Benchmark for neutronic analysis of sodium-cooled fast reactor cores with various fuel types and core sizes," No. NEA-NSC-R-2015-9, Organisation for Economic Co-Operation and Development (2016).
[29] K. S. Kim and M. D. DeHart, "Unstructured partial-and net-current based coarse mesh finite difference acceleration applied to the extended step characteristics method in NEWT," *Annals of Nuclear Energy*, **38.2-3**, pp. 527-534 (2011).
[30] S. Kosaka and E. Saji, "Transport theory calculation for a heterogeneous multi assembly problem by characteristics method with direct neutron path linking technique," *Journal of Nuclear Science and Technology*, **37.12**, pp. 1015-1023 (2000).
[31] B. Kochunas and T. J. Downar, "Parallel 3-D method of characteristics in MPACT," *Proceedings of M&C 2013*, Sun Valley, ID, USA, May 5-9 (2013).
[32] S. G. Stimpson *et al.*, "Boundary acceleration techniques for CMFD-accelerated 2D-MOC," *Proceedings of PHYSOR 2014*, Kyoto, Japan, September 28 – October 3 (2014).
[33] S. Choi and D. Lee, "Three-dimensional method of characteristics/diamond-difference transport analysis method in STREAM for whole-core neutron

transport calculation," *Computer Physics Communications*, **260**, 107332 (2021).
[34] S. C. Kim and H. G. Joo, "Performance enhancement of planar MOC calculation in hexagonal geometries by assembly-wise domain decomposition", *Proceedings of PHYSOR 2022*, Pittsburgh, PA, USA, May 15-20, pp. 493-502 (2022).
[35] R. Min, "Efficient treatment of anisotropic scattering in method of characteristics calculations," MS Thesis, Seoul National University, Department of Energy Resource Engineering, Seoul, Korea (2016).
[36] Y. A. Chao and Y. A. Shatilla, "Conformal mapping and hexagonal nodal methods—II: implementation in the ANC-H code," *Nuclear Science and Engineering*, **121.2**, pp. 210-225 (1995).
[37] Y. Z. Li, H. C. Wu, and L. Z. Cao, "Unstructured Triangular Nodal-SP 3 Method Based on an Exponential Function Expansion," *Nuclear Science and Engineering*, **174.2**, pp. 163-171 (2013).
[38] U. Grundmann and F. Hollstein, "A two-dimensional intranodal flux expansion method for hexagonal geometry," *Nuclear science and engineering,* **133.2**, pp. 201-212 (1999).
[39] H. J. Shim *et al*., "McCARD: Monte Carlo code for advanced reactor design and analysis," *Nuclear Engineering and Technology*, **44.2**, pp. 161-176 (2012).
[40] C. Lim, H. G. Joo, and W. S. Yang, "Development of a fast reactor multigroup cross section generation code EXUS-F capable of direct processing of evaluated nuclear data files," *Nuclear Engineering and Technology*, **50.3**, pp. 340-355 (2018).
[41] J. J. Grundzinski and C. Grandy, "Design and analysis of the core restraint system for a small modular fast reactor," *Transactions SMiRT-22*, San Francisco, CA, USA, August 18-23 (2013).
[42] E. R. Shemon *et al*., "Direct Neutronics Modeling Approach for Deformed Core Analysis using PROTEUS," *Proceedings of M&C 2017*, Jeju, Korea, April 16-20 (2017).
[43] E. Lum and C. L. Pope, "Simulation of the Fast Reactor Fuel Assembly Duct-Bowing Reactivity Effect Using Monte Carlo Neutron Transport and Finite Element Analysis," *Nuclear Technology*, **207.5**, pp. 761-770 (2021).
[44] G. Buckel, K. Kufner, and B. Stehle, "Benchmark calculations for a sodium-cooled breeder reactor by two and three-dimensional diffusion methods," *Nuclear Science and Engineering*, **64**, pp. 75-89 (1977).

요약 및 결론

이 연구에서는 VVER (Water-Water Energetic Reactor) 및 SFR (Sodium-cooled Fast Reactor) 노심에서의 불규칙적인 기하 구조를 정확히 모사하는 육방형 집합체 기반 선추적 해석 및 CMFD (Coarse Mesh Finite Difference) 계산 모듈을 직접전노심수송해석코드 nTRACER에 구현했다. 병렬 계산을 통한 계산 신속화를 위해서는 ADD (Assembly-wise Domain Decomposition)를 사용하여 육방형 집합체 기반 선추적 계산을 효과적으로 가속시켰다. 한편 SFR에서의 비균일 노심 열팽창을 효과적으로 모사하기 위해 노달코드 RENUS에 가변 구조에 대한 노달법 계산 모듈을 구현했다. 새로 구현한 nTRACER의 계산 모듈은 다양한 육방형 집합체 기반 벤치마크 문제에 대해 McCARD 표준해와 비교함으로써 계산 정확도를 검증했다. ADD의 효과는 병렬계산법에 따른 VVER 노심 문제에 대한 선추적 계산 시간을 비교함으로써 평가했다. 가변 구조 노달법 RENUS 계산 모듈은 임의로 변형된 2차원 SFR 벤치마크 문제에 대해 McCARD 표준해와 비교함으로써 계산 정확도를 검증했다.

동구권과 개도국에서 다수 운영되고 신설되고 있는 VVER과 4세대 원자로로서 활발하게 연구되고 있는 SFR은 공통적으로 육방형 집합체 기반 노심을 가진다. VVER 노심에서 Barrel, Vygorodka와 집합체 관, SFR 노심에서의 이중 집합체 관 및 다양한 집합체 내부 구조 등의 복잡한 구조물은 집합체 단위 균질화와 확산 방정식에 기초하는 2단계 계산 방법의 정확도를 상당히 저하시킨다. 이러한 배경하에 이 연구에서는 VVER과 SFR 노심 해석의 정확도를 제고하기 위해 전노심계산코드 nTRACER에 육방형 집합체 기반 노심 계산 기능을 구현하는 것을 목표로 삼았다. 집합체관과 Vygorodka를 그대로 모사하기 위해 육방형 집합체 기반 선추적 모듈에 Elongated 모델을 도입했다. 이 모델은 바깥 연료 셀을 오각형으로 확장함으로써 간극 셀을 평행사변형으로 모사한다. 이 모델에서 육방형 집합체가 다양한 기하 구조의 셀을 가지므로 셀 단위 모듈러 선을 구성할 때 필요한 메모리가 증가한다. 따라서 nTRACER는 육방형 집합체 단위 모듈러 선을 구성하여 선추적 계산을 수행했다.

기존 nTRACER의 CMFD 계산 모듈은 고정된 정방형 메쉬에서의 확산 방정식에 기초하여 구현되었으므로 Elongated 모델에서의 다양한 기하 구조의 메쉬를 해석할 수 없다. 따라서 확산 방정식에서의 메쉬 경계면 길이, 중심과 경계면과의 수직 거리 및 인접 메쉬 개수에 자유도를 부여함으로써 CMFD 계산 모듈이 가변 구조에 대해 적용될 수 있도록 기능을 확장했다. VVER 노심에서의 간극 셀은 연료 셀에 비해 크기가 매우 작으므로 CMFD 계산에서 이 간극 셀을 그대로 모사하는 것은 비효율적이다. 따라서 간극 셀 및 간극 셀과 인접한 연료 셀을 하나의 메쉬로 균질화한 후 CMFD 계산을 수행하는 Super pin 계산법을 도입했다. 이 방법에 의해 2차원 VVER 노심 문제에 대한 CMFD 계산 시간과 총 계산 시간이 각각 최대 39 %, 17 % 감소했다.

직접전노심계산법은 2단계 해석법에 비해 높은 정확도와 해상도를 가지는 반면 막대한 계산 자원과 계산 시간을 필요로 한다. 따라서 직접전노심수송해석법에는 메모리 사용량을 줄이고 병렬계산능을 높이는 최적화가 필수적이다. nTRACER는 3차원 노심을 여러 평면으로 나눈 후 컴퓨팅 노드의 CPU들을 사용하여 각 평면에서의 선추적 계산을 병렬적으로 수행하며, 평면에서의 선추적 계산 또한 CPU 코어들을 사용하여 병렬적으로 수행한다. CPU 코어들이 노심에서의 추적선을 병렬적으로 추적하는 기존 nTRACER 병렬계산법은 각 코어가 노심 전체 FSR (Flat Source Region) 정보를 저장하며 이에 따라 메모리 접근 연산에 막대한 계산 시간이 소요된다. 이 문제를 해결하기 위해 이 연구에서는 nTRACER의 육방형 집합체 기반 선추적 모듈의 병렬계산법으로서 CPU의 코어들이 각 집합체에서의 선추적 계산을 병렬적으로 수행하는 ADD를 구현했다. 이를 통해 각 CPU 코어에서 선추적 계산에 필요한 FSR 메모리가 크게 감소하고 이에 따라 선추적 계산 시간 상당히 감소했다. 한편, ADD 선추적 계산에서는 집합체 경계에서의 인입 부분 각중성자속가 불연속적으로 갱신되며 이에 따라 MOC (Method of Characteristics) 계산 수렴성이 악화된다. 이러한 불연속성을 완화하기 위해 CMFD 계산 전후 인입 부분 각중성자속의 변화율로 인입 부분 각중성자속을 보정하는 방법과 3색 계산법을 도입했다. 3색 계산법이란 노심에서의 육각형 집합체를 세 가지 그룹으로 나누고 한 그룹에서의 선추적 계산 이후 집합체 경계면에서의 외행 부분 각중성자속을 다른 그룹에서의 인입 부분 각중성자속으로 사용하는 방법이다. 이를 통해

선추적 반복 횟수를 줄임으로써 2차원 VVER 노심 문제에 대한 총 계산 시간이 최대 13 % 감소했다. 한편 AFSS (Angular Flux Storage Scheme)를 사용하여 ADD 선추적 계산 시간을 추가적으로 단축시켰다. AFSS란 Segment에서의 각중성자속 변화를 별도로 저장하여 선추적이 끝난 후 중성자속을 한번에 계산하는 방법이다. 이를 통해 중성자속 모먼트 계산에서의 수학적 연산수를 줄임으로써 2차원 VVER 노심 문제에 대한 총 계산 시간이 최대 26 % 감소했다.

SFR 노심에선 높은 열출력 밀도와 급격한 온도 변화에 의해 집합체 관에 변형이 발생하며 이에 따라 연료와 냉각재의 부피비가 달라지므로 노심 반응도 및 열출력 분포 또한 크게 변한다. 기존 연구에서 이러한 비균일 노심 열팽창을 해석하기 위해 사용한 유한차분법, 유한요소법 및 몬테칼로 방법은 모두 적절한 정확도를 달성하기 위해 상당한 계산 자원을 필요로 한다. 반면 계산 자원을 가장 적게 사용하는 노달법은 지금까지 규칙적인 기하 구조에 대해서만 계산식이 유도되었다. 이러한 배경으로부터 이 연구에서는 노달코드 RENUS에 가변 구조 노달법 해석 모듈을 구현했다. 구체적으로는 횡 방향 T-PEN (Triangle-based Polynomial Expansion Nodal) 방법과 CPB (Corner Point Balance) 계산 및 CMFD 계산을 가변 구조에 대해 확장했다. T-PEN과 CPB 방법은 유도 변수를 표현 변수의 식으로 표현한 후 물리적 제한식에 이 식을 대입함으로써 선형계를 구성한다. 이 변수들에는 경계면과 메쉬에서의 중성자속 평균값 등이 포함된다. 따라서 가변 구조 노달법을 구현하기 위해서는 가변 경계면과 가변 영역에서의 다항식 선적분 및 면적분을 계산해야 한다. 이 연구에서는 다각형을 여러 평행사변형으로 나눈 후 미리 계산된 순람표를 사용하여 적분값을 계산하는 방법을 고안했다. RENUS는 이 방법을 사용하여 변형된 집합체에서의 변수들을 다항식으로 표현하며 이를 통해 선형계를 수립하고 노달계산을 수행한다. 가변 구조에 대한 RENUS의 CMFD 계산 모듈은 nTRACER에서의 CMFD 계산 모듈과 같은 방법으로 구현했다.

nTRACER의 계산 정확도는 다양한 육방형 집합체 기반 노심 문제에 대해 nTRACER 계산 결과와 McCARD 표준해를 비교함으로써 검증했다. 기존 C5G7 벤치마크를 육방형 집합체 기반 노심으로 변형한 C5G7 H 벤치마크에서 제어봉 삽입 정도를 달리한 세 개의 3차원 노심 문제에

대해 반응도 오차는 7 pcm 이하며, 3차원 봉 출력 오차의 최댓값과 RMS (Root-mean-square) 값은 각각 6.41 %, 0.44 % 이하였다. KAERI에서 제안한 VVER-1000 벤치마크에서 핵연료와 감속재의 온도 및 붕산 농도를 달리한 9 개의 2차원 노심 문제에 대해 nTRACER가 P0 옵션을 사용할 때 반응도 오차는 106 pcm 이하며, 봉 출력 오차의 최댓값과 RMS 값은 각각 2.24 %, 0.95 % 이하였다. 온도가 높고 붕산 농도가 낮은 노심 문제에 대해 nTRACER가 P2 옵션을 사용할 때 계산 결과 오차가 효과적으로 감소했다. nTRACER가 P2 옵션을 사용함으로써 반응도 오차는 최대 70 pcm 감소하며, 봉 출력 오차의 최댓값과 RMS 값은 각각 최대 0.25 %, 0.12 % 감소했다. VVER-440 'Full-core' 2차원 노심 문제 및 MER-1000 SFR 2차원 노심 문제에 대해서도 P2 옵션을 사용할 때 nTRACER와 McCARD 계산 결과가 잘 일치했다. 이러한 검증 결과를 바탕으로 하여 nTRACER의 육각형 집합체 기반 노심 해석 모듈이 높은 계산 정확도를 가진다는 결론을 얻었다.

nTRACER ADD의 선추적 계산 가속 효과는 다양한 VVER 노심에 대해 ADD 사용 전후 선추적 계산 시간을 비교함으로써 검증했다. ADD에 의해 발생한 계산 결과의 반응도 오차와 봉 출력 오차는 각각 최대 1 pcm, 0.78 %였으며 이를 통해 ADD가 계산 정확도를 저해하지 않음을 확인했다. 2차원 노심 문제에 대해 ADD를 사용할 때 총 선추적 계산 시간은 1/6 노심과 전노심에서 각각 최대 18 %, 48 % 감소하며, 총 계산 시간은 1/6 노심과 전노심에서 각각 최대 6 %, 38 % 감소했다. 3차원 노심 문제에 대해 ADD를 사용할 때 총 선추적 계산 시간은 1/6 노심과 전노심에서 각각 최대 44 %, 53 % 감소하며, 총 계산 시간은 1/6 노심과 전노심에서 각각 최대 36 %, 45 % 감소했다. 이러한 검증 결과를 바탕으로 하여 ADD에 의해 nTRACER 육각형 집합체 기반 선추적 계산이 효과적으로 가속된다는 결론을 얻었다.

RENUS 가변 구조 노달법의 계산 정확도는 SNR-300 (schneller natriumgekühlter reaktor-300) 2차원 변형 노심 문제에 대해 RENUS 계산 결과와 McCARD 표준해를 비교함으로써 검증했다. 이 연구에서는 임의 노심 변형인 국부 변형 상태를 각 집합체 꼭짓점을 노심 바깥 방향으로 집합체 길이의 9 %만큼 이동시키는 것으로 정의했다. 기존 SNR-300 2차원 노심 문제에 대해 RENUS는 McCARD와 비교하여 최대 508 pcm

반응도 오차 및 3.38 % 집합체 열출력 오차로 다소 큰 계산 오차를 가진다. 반면 국부 변형에 의해 McCARD 반응도 및 집합체 열출력이 최대 240 pcm 및 47.76 %만큼 변할 때 각 변화에 대한 RENUS와 McCARD의 계산 오차는 각각 7 pcm와 0.46 % 이내였다. 연료 영역에서의 균일한 팽창에 의한 노심 변형 문제에선 반대 부호를 가지는 각 집합체에서의 계산 오차가 서로 상쇄될 수 있다. 따라서 집합체 단위 팽창에 의한 노심 변형 문제들에 대해서도 RENUS 검증을 수행했다. 이 노심 문제들에 대해 McCARD 반응도 및 집합체 열출력이 최대 383 pcm 및 45.52 %만큼 변할 때 각 변화에 대한 RENUS와 McCARD의 계산 오차는 각각 18 pcm와 0.40 % 이내였다. 이러한 검증 결과는 RENUS와 McCARD의 적은 계산 오차가 어떠한 오류 상쇄에도 의존하지 않음을 보인다. 따라서 RENUS가 가변 구조 노달법을 사용하여 노심 변형에 의한 노심 핵특성 변화를 높은 정확도로 예측한다는 결론을 얻었다.

이 연구에서는 직접전노심수송해석코드 nTRACER에 육방형 집합체 기반 선추적 해석 및 CMFD 계산 모듈을 구현하고 노달코드 RENUS에 가변 구조 노달법 해석 모듈을 구현함으로써 다양한 활용이 가능한 고신뢰도 육방형 노심해석체계를 개발했다. nTRACER는 VVER과 SFR 노심의 복잡한 구조물을 정확하게 모사함으로써 육방형 집합체 기반 노심에 대해 McCARD 표준해와 잘 일치하는 계산 결과를 생산했다. 육방형 집합체 기반 선추적 계산의 병렬계산법으로 ADD를 사용함으로써 nTRACER의 계산 효율성을 향상시켰다. RENUS는 임의로 변형된 육방형 집합체 기반 노심에 대해 가변 구조 노달법을 사용하여 McCARD 표준해와 잘 일치하는 계산 결과를 생산했다. nTRACER는 높은 계산 정확도와 계산 효율성으로 인해 이미 여러 T/H 코드와 연계되어 VVER 노심에 대한 다물리 해석에 사용되고 있다. 이 연구에서 개발한 고신뢰도 육방형 노심해석체계는 향후 비균일 노심 열팽창을 포함하는 총체적 SFR 노심 해석에도 유용하게 사용될 것으로 기대된다.

초 록

이 연구에서는 VVER (Water-Water Energetic Reactor) 및 SFR (Sodium-cooled Fast Reactor) 노심에서의 불규칙적인 기하 구조를 정확히 모사하는 육방형 집합체 기반 선추적 해석 및 CMFD (Coarse Mesh Finite Difference) 계산 모듈을 직접전노심수송해석코드 nTRACER에 구현했다. VVER 노심의 집합체관과 Vygorodka를 그대로 모사하기 위해 육방형 집합체 기반 선추적 모듈은 Elongated 모델을 도입했다. 이때 육방형 집합체 단위 모듈러 선을 구성하여 선추적 계산을 수행함으로써 노심 추적선 저장에 필요한 메모리를 줄였다. Elongated 모델에서의 다양한 기하 구조의 메쉬를 해석하기 위해 CMFD 계산 모듈의 기능을 가변 구조에 대해 확장했다. 이때 Super pin 해법을 사용함으로써 2차원 VVER 노심 문제에 대해 nTRACER의 CMFD 계산 시간 및 총 계산 시간이 각각 최대 39 % 및 17 % 감소했다.

병렬 계산을 통한 계산 신속화를 위해 ADD (Assembly-wise Domain Decomposition)를 사용하여 육방형 집합체 기반 선추적 계산을 효과적으로 가속시켰다. ADD에 의해 각 CPU 코어에서 선추적 계산에 필요한 FSR (Flat Source Region) 메모리가 집합체 범위만큼으로 크게 감소하고 이에 따라 선추적 계산 시간이 상당히 감소했다. 이때 MOC (Method of Characteristics) 계산 수렴성이 악화되는 문제를 완화하기 위해 CMFD 계산 전후 인입 부분 각중성자속의 변화율로 인입 부분 각중성자속을 보정하는 방법과 3색 계산법을 도입했다. 3색 계산법과 AFSS (Angular Flux Storage Scheme)를 사용함으로써 2차원 VVER 노심 문제에 대한 총 계산 시간이 각각 최대 13 % 및 23 % 감소했다.

SFR에서의 비균일 노심 열팽창을 효과적으로 모사하기 위해 노달코드 RENUS에 가변 구조 노달법 계산 모듈을 구현했다. 우선 가변 구조 다각형을 여러 평행사변형으로 나눈 후 미리 계산된 순람표를 사용하여 적분값을 계산하는 방법을 고안했다. 이 방법을 사용하여 횡방향 T-PEN (Triangle-based Polynomial Expansion Nodal) 방법과 CPB (Corner Point Balance) 계산을 가변 구조에 대해 확장했다. RENUS의 3차원 CMFD 계산 모듈은 nTRACER에서와 같은 방법으로 가변 구조에 대해 확장되었다.

nTRACER의 계산 정확도는 다양한 육방형 집합체 기반 노심 문제에 대해 nTRACER 계산 결과와 McCARD 표준해를 비교함으로써 검증했다. 세 개의 3차원 C5G7 H 벤치마크 노심 문제에 대해 반응도 오차는 7 pcm 이하며, 3차원 봉 출력 오차의 최대값과 RMS (Root-mean-square) 값은 각각 6.41 %, 0.44 % 이하였다. 9 개의 2차원 KAERI VVER-1000 노심 문제에 대해 nTRACER가 P0 옵션을 사용할 때 반응도 오차는 106 pcm 이하며, 봉 출력 오차의 최대값과 RMS 값은 각각 2.24 %, 0.95 % 이하였다. 2차원 'Full-core' VVER-440 및 MET-1000 SFR 노심 문제에 대해서도 nTRACER와 McCARD 계산 결과는 잘 일치했다. nTRACER가 P2 옵션을 사용함으로써 반응도 오차와 봉 출력 오차의 최댓값은 각각 최대 70 pcm 및 0.90 % 감소했다. 이러한 검증 결과를 바탕으로 하여 nTRACER의 육각형 집합체 기반 노심 해석 모듈이 높은 계산 정확도를 가진다는 결론을 얻었다.

nTRACER ADD의 선추적 계산 가속 효과는 다양한 VVER 노심에 대해 ADD 사용 전후 선추적 계산 시간을 비교함으로써 검증하였다. 2차원 전노심 문제에 대해 ADD를 사용할 때 총 선추적 계산 시간과 총 계산 시간은 각각 최대 48 % 및 38 % 감소했다. 3차원 전노심 문제에 대해 ADD를 사용할 때 총 선추적 계산 시간과 총 계산 시간은 각각 최대 53 % 및 45 % 감소했다. 이러한 검증 결과를 바탕으로 하여 ADD에 의해 nTRACER 육각형 집합체 기반 선추적 계산이 효과적으로 가속된다는 결론을 얻었다.

RENUS 가변 구조 노달법의 계산 정확도는 SNR-300 (schneller natriumgekühlter reaktor-300) 2차원 변형 노심 문제에 대해 RENUS 계산 결과와 McCARD 표준해를 비교함으로써 검증했다. 이 연구에서는 가변 구조 노달법의 계산 정확도를 검증하기 위해 노심 문제에 국부 변형 상태를 도입했다. 연료 영역에 대한 국부 변형에 의해 반응도 및 집합체 열출력이 각각 최대 240 pcm 및 47.76 %만큼 변할 때 각 변화에 대한 RENUS와 McCARD의 계산 오차는 각각 7 pcm와 0.46 % 이내였다. 연료 영역에서의 균일한 팽창에 의한 노심 변형 문제를 집합체 단위 팽창에 의한 노심 변형 문제들로 분해한 후, 이 문제들에 대해서도 RENUS 해법의 정확도를 검증했다. 이 검증 결과들을 바탕으로 하여 RENUS가

가변 구조 노달법을 사용하여 노심 변형에 의한 노심 핵특성 변화를 어떠한 오류 상쇄 없이도 높은 정확도로 예측한다는 결론을 얻었다.

주요어 : 육방형 집합체 기반 노심, 선추적 계산, 소격격자 유한차분법, 집합체 단위 영역분할법, 노심 열팽창, 가변 구조 노달법
학 번 : 2016-21288